

Numerical and experimental study of the tolerance of natural laminar flow on a wing to TS destabilisation at the leading edge /wing-box junction

Ashworth R.^{*}, Lawson S.^{***}, Lowry R.^{**}, Martinez-Cava A.^{*1}, Mughal S.[¶], Roland H.^{*2}, Thomas C.[¶]

^{*}Airbus Group Innovations, Filton, BS34 7QW

^{**}Airbus Operations Ltd, Filton BS99 7AR

^{***}Aircraft Research Association, Manton Lane, Bedford, England, MK41 7PF

[¶]Dept. Mathematics, Imperial College, London

¹Current address: School of Aeronautics, Universidad Politecnica de Madrid, Madrid

²Current address: Dept. Mathematics, Imperial College, London

Abstract

The junction between the leading edge and wing box components of natural laminar flow wings presents a feature to the flow that can potentially enhance the growth of transition causing Tollmein Schlichting (TS) instabilities leading to a significant forward movement of transition. Even when a filler is applied to the gap between the components, subsequent curing will lead to a shallow cavity formed by the filler surface. This paper describes a detailed experimental and numerical study of flow over realistic filler shapes under conditions representative of a natural laminar flow wing. Wind tunnel results show that for the width of gap examined there is an initial forward movement of transition by a quite significant amount for very shallow filled gaps but essentially no further movement as the depth is increased. PSE based stability analysis reveals that there is a destabilisation of modes near the gap. The degree of destabilisation appears to plateau with increasing depth due to recirculation of flow inside the gap which maintains an almost constant effective depth. Compensating stabilisation soon after the gap means however that there is very little lasting effect of the gap on the magnitude of the transition causing modes further downstream and stability analysis suggests there is little movement in transition as seen beyond a certain depth. The initial movement observed in the tunnel tests may be due to enhanced receptivity to TS waves at the site of the gap which is not captured by the stability analysis.

Introduction

Since NLF wings have low sweep the interaction of TS instabilities with the gap region and its effect on transition can be reasonably well captured by a zero sweep configuration. In fact a more compact representation of the flow can be provided by a ring-wing configuration provided the diameter of the annulus is large compared to the boundary layer thickness. Such a configuration has been designed by Airbus for manufacture by ARA and subsequent testing in their transonic wind-tunnel. The configuration consists of three segments, in two of which an insert is machined to represent an azimuthally running groove of representative width L and at a representative chord location with a profile corresponding to a realistic filler shape. The third segment is left clean to provide a reference point. Appropriately positioned pressure taps, hot films and coatings of temperature sensitive paint have provided detailed pressure, velocity fluctuation and transition front data. Three separate runs enabled 6 depths of filler profile to be tested. Computational studies have been carried out at Airbus Group Innovations (AGI) and Imperial College (IC) using the IC PSE based stability method and a recently developed RANS boundary layer extraction tool for the base flow. Numerical results have been able to reproduce and explain the lack of movement in transition seen in tunnel tests for deeper gaps but not the initial movement seen for very shallow gaps. However there are indications that the initial movement may be due to a receptivity mechanism not captured by the stability calculations. In the first part of this paper a description is given of the wind tunnel tests and the measurements that have been made. The numerical approach is then described and a comparison made between the numerical and experimental results. A possible explanation is offered in terms of receptivity for the observed initial movement in transition for shallow depths followed by little further movement as the depth is increased. The paper ends with some conclusions and recommendations for future work.

Experimental Set-up

Wind Tunnel

The ARA transonic wind tunnel is a closed circuit, continuous operation porous wall tunnel, with a Mach number range up to 1.4. The rectangular test section is 2.74m x 2.44m, with a maximum wall porosity of 22 μm . Stagnation pressure can be varied from 0.8 to 1.2 bar, although the tunnel was operated at 1 bar for these tests. The TWT has been qualified for NLF testing during a previous research programme, SAWoF [1].

Model Design

The model used for these tests was a ring wing configuration, as shown in figure 1. The model was designed to be circumferentially uniform, with an identical aerofoil section at all points around the circumference, maximising the measurement area whilst eliminating the end effects of a panel wing. The flow-field around the circumference was effectively 2D since the ratio of model diameter to boundary layer thickness was very large. The aerofoil was a natural laminar flow section derived by Airbus.

The model was divided into 3 segments, with a full set of instrumentation in each segment. The effect of 3 different surface imperfections could therefore be measured in each tunnel run. Features designed to model various surface imperfections were installed at a representative chord-wise location for a leading edge/wing box junction. These consisted of 6 groove features. Each groove feature consisted of a shallow channel of fixed width (L) and with a radius on the bottom corners. The grooves depths (D) ranged over the depth to width ratios $D/L=0.35 \times 10^{-2}$ to $D/L=10.55 \times 10^{-2}$.



Figure 1: Ring wing model installed in the ARA TWT

Instrumentation

The model was designed to provide measurements of transition and surface pressure distributions as shown in figure 2. Static pressure tappings were installed in 3 rows, one on each of the 3 segments. The pressures in each row were aligned to ensure each tapping was unaffected by any turbulent wedge that might have originated from the upstream tapping.

Twelve Dantec hot films were installed on the model in a row on each segment of the model, i.e.36 in total. These were also aligned to ensure each hot film was unaffected by any turbulent wedge that might have originated from the upstream hot film.

Transition was mainly determined from measurements of surface temperature during a step increase in freestream temperature using both Temperature Sensitive Paint (TSP) and Infra-Red (IR) thermography. The technique requires an insulating layer which on this model consisted of a 4mm

thick panel covering a large area of the surface of each segment. The panels, consisting of a thermoplastic polymer, were machined to conform exactly to the required surface profile. TSP data were processed to determine transition location by first calculating the ratio of hot to cold images before and after the freestream temperature step. Transition onset and completion were defined for this study as the maximum and minimum of the second order derivative of intensity ratio with respect to chord.

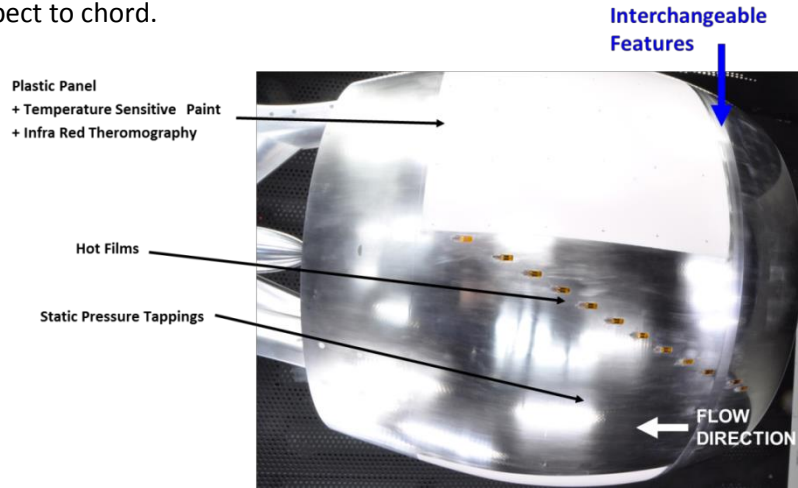


Figure 2: Installed measurement system

Test Programme

Three configurations were tested, each with 3 different features, one in each segment. The configurations were tested with one of the segments consisting of a clean profile with no features to provide a consistent baseline. The tests were conducted at a range of subsonic and transonic Mach numbers at zero incidence and sideslip throughout.

Results

The pressure measurements showed that a consistent pressure distribution was achieved throughout the test. Transition onset was calculated using IR, TSP and hot films. An example of a temperature sensitive paint result after calculating the hot/cold ratio and displaying the slice locations is shown in figure 3 (left). Also in this figure it is shown how the intensity ratio distribution is used to determine transition location (right).

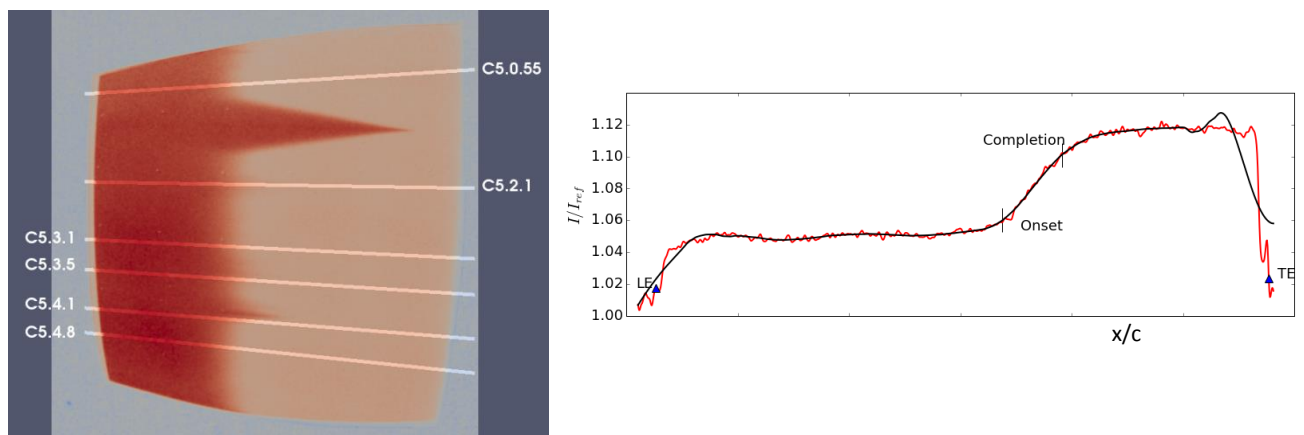


Figure 3: Example of TSP data (left) and use of TSP intensity ratio to determine transition (right)

In figure 4 (left) is an example of a infra-red camera image that can be used to reveal transition fronts including turbulent wedges such as seen near the opt of the image. In figure 4 (right) is a power spectral density composed from hot film data. These will be examined in more detail below.

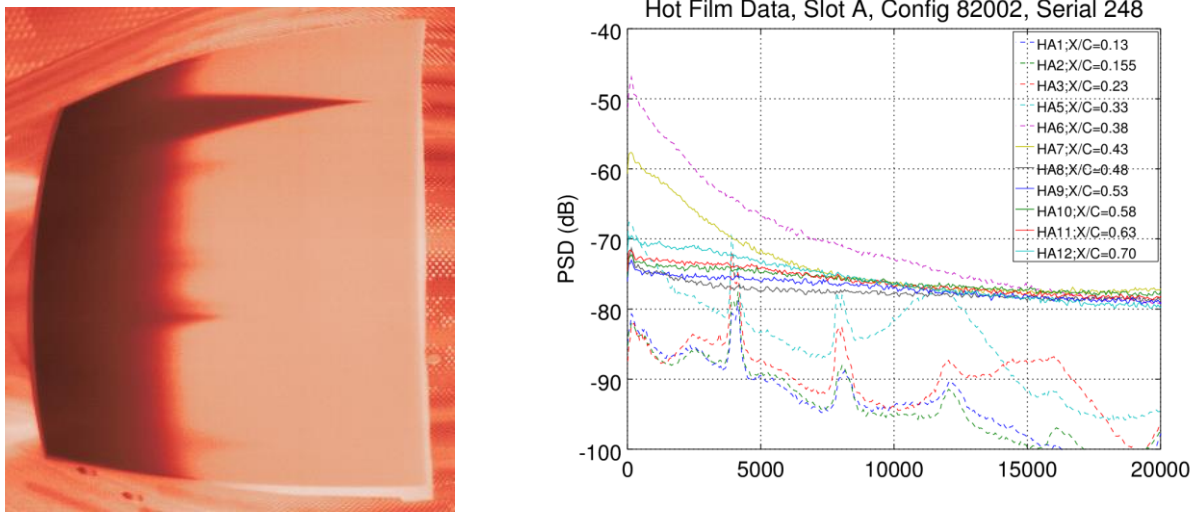


Figure 4: Infra-red camera image (left) and example of PSD of hot film data (right)

Finally, initial results on the effect of groove depth on transition position are shown in figure 5. For this the average of 3 to 5 locations on each segment corresponding to groove depths varying by no more than +/-5 microns has been used. The standard deviation indicates the transition position is accurate to within +/-1% chord. These show a marked forward movement of transition of chord for a groove of depth $D/L=2 \times 10^{-2}$ compared to the clean wing. As groove depth increases further, transition is relatively constant with evidence of a small rearward movement at a depth $D/L=6 \times 10^{-2}$.

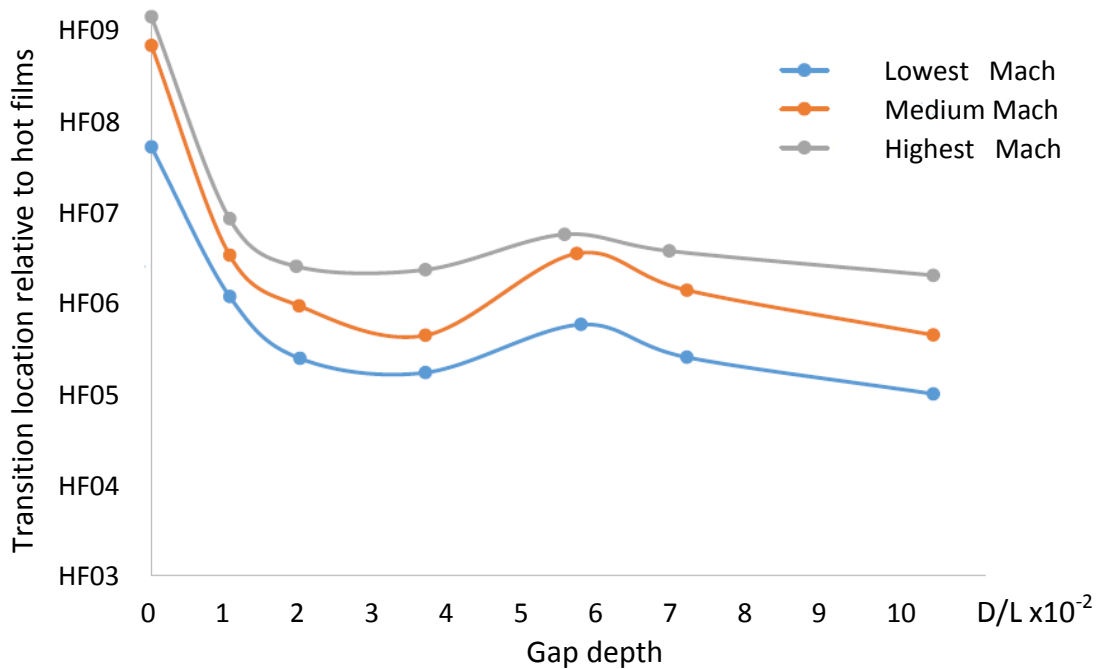


Figure 5: Variation of averaged transition locations with gap depth for each of three Mach numbers

Numerical Studies

Flow conditions for numerical study

Flow computations were performed in advance of the wind-tunnel test and were used to guide the choice of tunnel conditions as well as the range of filler depths for the inserts. The computations were performed at the highest of the three Mach numbers in the test and at a Reynolds number per metre of $Re=12.32 \times 10^6$. Transition was fixed a little aft of the most downstream transition location.

Computation of Base Flow

RANS computations were performed with the DLR tau solver and SOLAR meshing. Initial computations at Airbus were for a fully 3d clean configuration. Work at AGI was then directed towards developing a new mesh which could reproduce the Airbus results for a clean configuration but would also admit deformations in the surface to represent the filler configurations. The challenge in the re-meshing work was to adequately resolve the very small scales of the filled gap (small chord-wise extent, L , and depth ratio as little as $D/L=1.2 \times 10^{-2}$) whilst not ending up over resolving the remainder of the surface for the sake of solution quality. Figure 6 (left) shows the final 3d meshing strategy that was adopted for the surface meshing. A span-wise refinement of L together with a chord-wise refinement of $3L/40$ was adopted over a T shaped region. A zone of gradual de-refinement was adopted around these regions to match the background level of resolution.

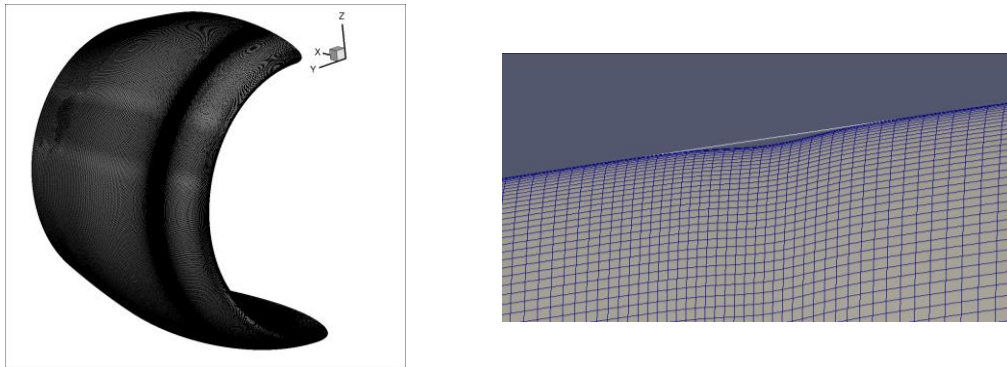


Figure 6: Surface mesh show regions of refinement (left) and detail showing exponential depression (right)

This resulted in a half-mesh with 30 million cells. The mesh could then be deformed to represent a simple exponential type filler as shown in figure 6 (right) which was used for numerical studies in advance of the actual filler profiles being defined. Acceptable RANS solutions for a range of filler depths were obtained and some preliminary boundary layer extraction and stability analysis was performed to demonstrate the method. However the actual filler profiles that were finally adopted for the tunnel tests were considerably more demanding than the simple exponential profiles. Being representative of what happens to real filler they were characterised by a much sharper descent from the rim to the base of the depressed region with the base being flat bottomed. This necessitated the resolution of much finer scales in the vicinity of the rims. Attempts to achieve this in a fully 3d mesh resulted in unmanageably large meshes and it was necessary to rethink the meshing strategy. It was decided to represent the flow through an equivalent axisymmetric configuration that produced the same boundary layer development on the outer surface.

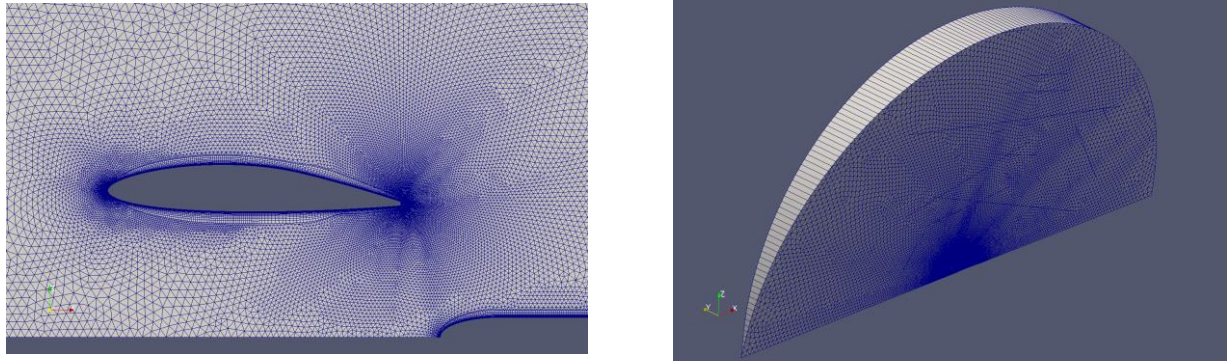


Figure 7 Axisymmetric mesh for ring wing equivalent configuration

Starting from the sting plus aerofoil from a 2d section of the original 3d configuration the sting diameter was increased by a factor of 1.9 to produce an axisymmetric mesh (figure 7) with the required blockage effect to produce an attachment line and cp distribution closely corresponding to that of the full 3d configuration with vanes etc. N factors calculated with BL2d and CoDS showed good agreement with those obtained for the 3d configuration as seen in figure 8. The use of an axisymmetric mesh with 1 cell in the azimuthal direction enabled chord-wise refinement down to about $L/40$ to be achieved i.e. 40 cells across the filled gap.

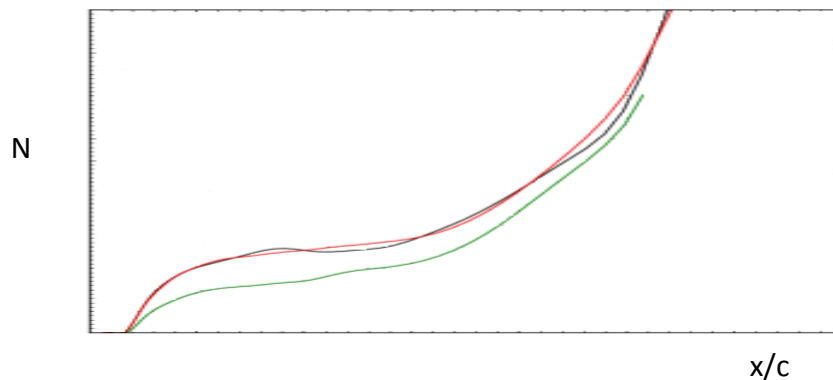


Figure 8: N factor envelope for axisymmetric configuration compared to Airbus 3d configuration (blue), with axisymmetric results before (green) and after (red) adjusting blockage.

The mesh refinement together with pressure coefficients obtained for a particular depths are shown in figure 9. It can be seen that there is a strong adverse pressure gradient over the gap followed by a pressure recovery.

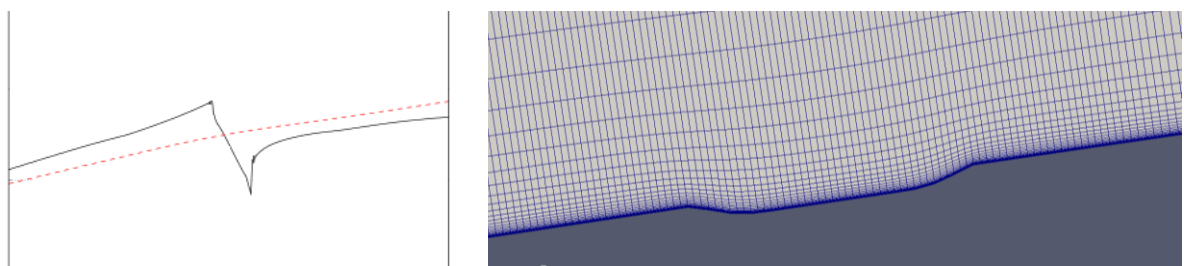


Figure 9: Pressure coefficient with and without gap (left) for realistic filler shape. Details of mesh (right)

Extraction of base flow

A common approach to computing the base flow is to use surface pressure from a RANS solution to provide edge velocity conditions for a more accurate and highly resolved solution of the boundary layer equations in the laminar boundary layer region. This approach could not be adopted here for anything other than the clean configuration because of the presence of flow separation over the filled gap which cannot be captured by solving the boundary layer equations. Instead use was made of a capability that has been developed at AGI and Imperial by Thomas [2] to extract the necessary boundary layer profile data directly from the RANS solution. This includes both the velocity and velocity gradient data that is required in order to perform a stability analysis based on solutions of the parabolised stability equations (PSE). In figure 10 it can be seen from the REBL data that the flow recirculates in the cavity formed by the filled gaps forming a virtual floor which it is suggested reduces the effective depth of deeper cavities.

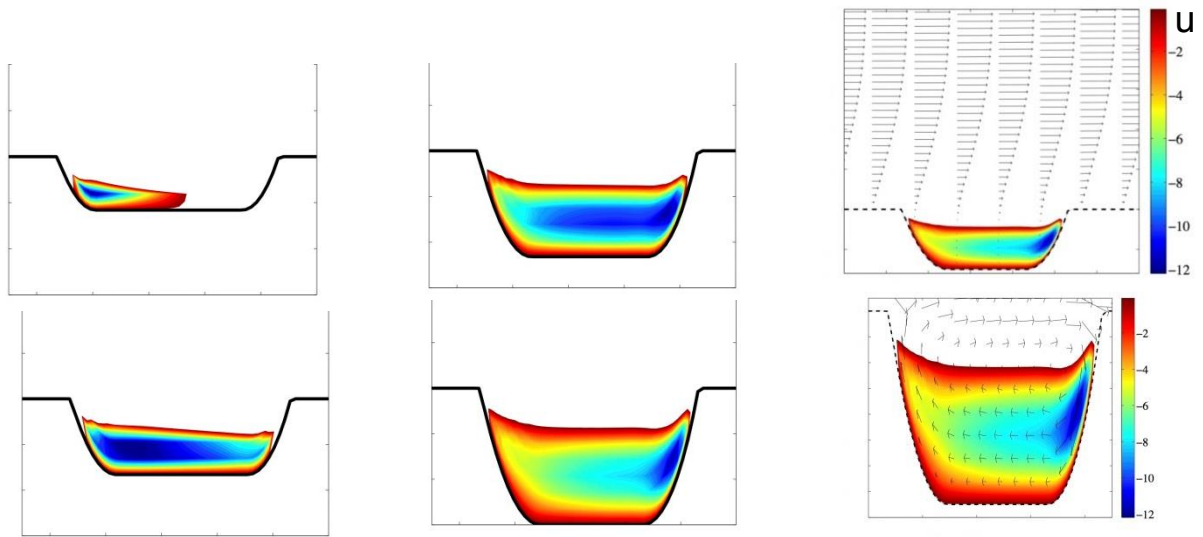


Figure 10: REBL data from RANS solutions for different filler depths showing reversed flow region and almost constant depth virtual floor.

Stability Analysis

Preliminary analysis at Airbus for design of the ring wing geometry had been through solution of the Orr-Sommerfeld equations (OSE) to determine growth rates for TS modes. Spatial integration of these growth rates gives a relative amplitude e^N for each mode at every location from which an envelope of maximum N factors can be determined. The OSE solution is a local approach based on a parallel flow assumption that is perfectly valid for the clean configuration. Thus a similar OSE based approach was adopted at AGI for checking that solutions on its new meshes resulted in similar N factor envelopes to those of Airbus as shown previously in figure 8. However for the purpose of determining the effect of the filled gaps on the growth on TS modes it was anticipated that the parallel flow assumption would not be valid in the vicinity of the gap where the flow separates. Thus the analysis at AGI for the parametric studies was based on solution of the parabolised stability equations (PSE) – a non-local approach that arises from considering weakly non-parallel flow (see Herbert [3]). For this purpose the CoPSE (compressible PSE) solver of Mughal was used [4].

Figures 11, 12 and 13 show the results of the stability analysis for the clean configuration and for filled gaps ranging in depth from $D/L=1.2 \times 10^{-2}$ to $D/L=7.5 \times 10^{-2}$. Unstable modes ranging in frequency from below 10kHz to 40kHz have been included in the analysis. As can be seen for the clean configuration, figure 11 (top), there is an upstream onset of instability of the highest frequency modes with progressively lower frequency modes becoming unstable and dominating downstream

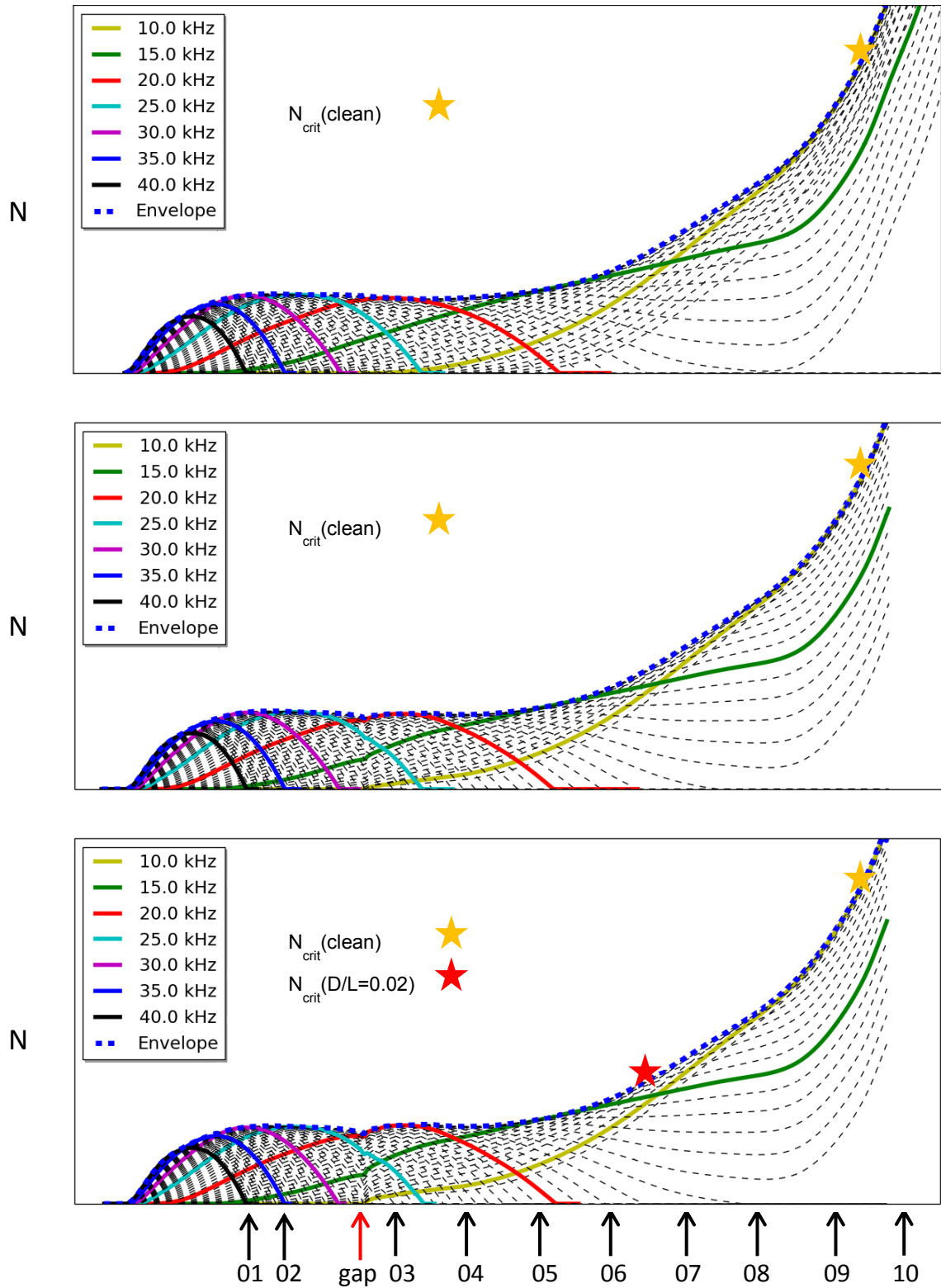


Figure 11: Envelope of N factors calculated for a clean wing (top) and gaps of depth $D/L=0.012$ (middle) and $D/L=0.020$ (bottom). Hot film locations are indicated by black arrows and the gap by a red arrow. Orange stars indicate transition location using N_{crit} for the clean configuration and red stars indicate transition locations based on an N_{crit} for a configuration with gap of depth $D/L=0.02$.

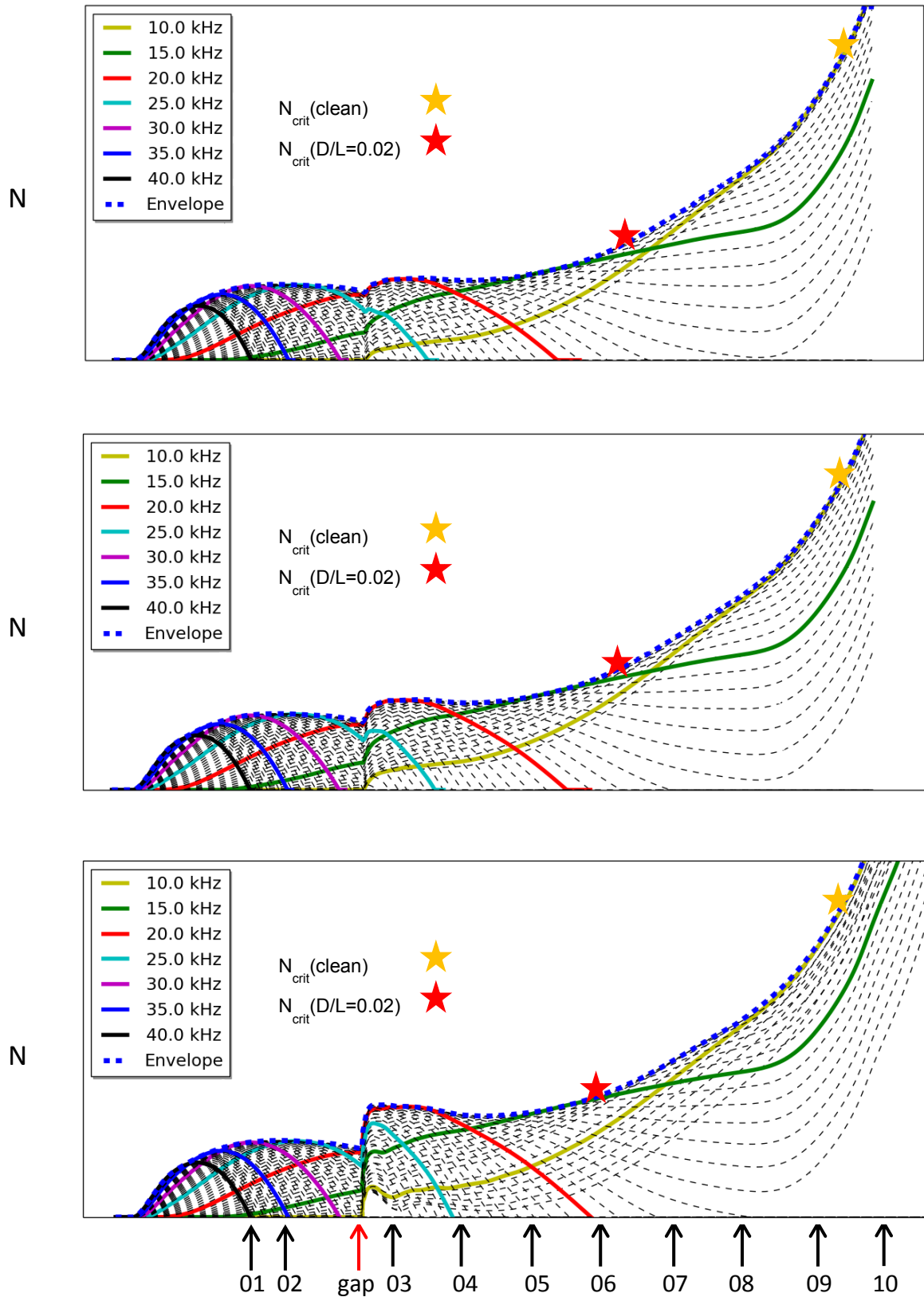


Figure 12: Envelope of N factors calculated for gaps of depth $D/L=0.029$ (top), $D/L=0.042$ (middle) and $D/L=0.058$ (bottom). Hot film locations are indicated by black arrows and the gap by a red arrow. Orange stars indicate transition location using N_{crit} for the clean configuration and red stars indicate transition locations based on an N_{crit} for a configuration with gap of depth $D/L=0.02$.

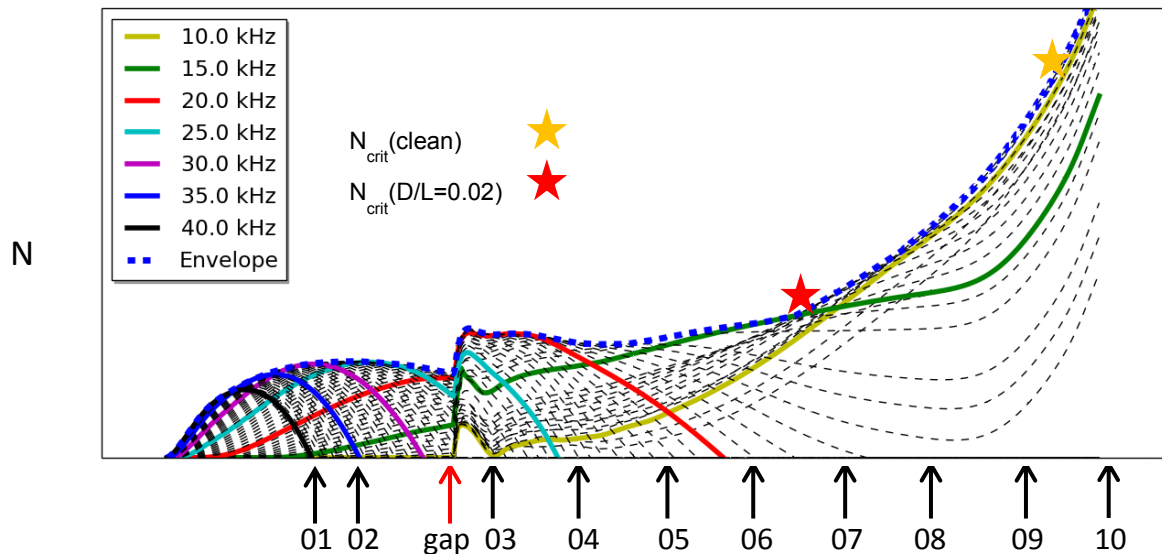


Figure 13: Envelope of N factors calculated for gap of depth $D/L=0.075$ (top). Hot film locations are indicated by black arrows and the gap by a red arrow. Orange stars indicate transition location using N_{crit} for the clean configuration and red stars indicate transition locations based on an N_{crit} for a configuration with gap of depth $D/L=0.02$.

before stabilising again as the boundary layer thickens. For 18kHz and below the modes do not decay completely but undergo a further phase of instability starting at around hot film 8 or 9 for 18kHz. As the frequency reduces further the preceding region of stabilisation (decay in N factor) becomes less pronounced until for 16kHz and below there is no stabilisation at all. Experimental data indicates transition occurs at the location of the yellow star from which a critical N factor can be determined for a transition causing mode of around 10 kHz.

As the depth of the filled gap is increased from ratio $D/L=1.2 \times 10^{-2}$ to $D/L=7.5 \times 10^{-2}$, figure 11 (middle) - figure 13, it is seen that there is a rapid growth in all modes over the gap which results in a sudden increase in N factor with the magnitude of the increase getting larger as the depth increases (except for the deepest gap, $D/L=7.5 \times 10^{-2}$, where the results indicate a smaller increase compared to $D/L=5.8 \times 10^{-2}$). For the higher frequency modes this rapid growth is then followed by more moderate growth and decay following a similar pattern to the clean configuration. For the lower frequency modes in the 10-15 kHz range it is seen that as the depth of the filled gap is increased beyond $D/L=7.5 \times 10^{-2}$ the region of rapid growth is increasingly offset by a more extended region of decay so that by hot film 3 there is little (for $D/L=7.5 \times 10^{-2}$) or no (for $D/L=7.5 \times 10^{-2}$) increase in N factor for these modes. Subsequent evolution is similar to that for the clean configuration and the results would imply very little movement in transition arising from the passage of TS modes across the gap. This does not exclude the possibility of movement due to a receptivity mechanism in which new modes are introduced through the interaction of the gap with the acoustic environment.

Validation of numerical results against experimental data

Comparison of results

A comparison of the experimental and computational surface pressure coefficient in figure 14 reveals that they are in good agreement in the important regions of the outer surface where the TS modes are developing. In figure 15 the experimentally determined transition locations of figure 5 has been reproduced and the numerically determined transition locations (indicated by orange and red stars) have been added. These transition locations correspond to the orange and red stars in the PSE plots. Orange stars are based on the assumption that the critical N factor is constant at its clean value throughout whereas red stars are based on the assumption that the critical N factor

reduces initially with depth (perhaps due to receptivity at the gap) but then is constant at its value for $D/L = 2.0 \times 10^{-2}$. Use of the latter N factor assumes that the critical N factor is constant i.e. there is no increase in receptivity effects arising from the gap as the depth increases further. The numerical locations are in reasonable agreement with experiment except at $D/L = 7.5 \times 10^{-2}$ where there is a forward movement in the numerical transition compared to a backward movement in the experimental transition. Setting instead a critical N factor based on the clean configuration, it is found that the stability computations are completely unable to predict the initial rapid forward movement with depth of the gap. Instead it is seen that there is no movement at all in the transition location as indicated by the orange stars in the PSE plots and in figure 15. Thus using the critical N factor at $D/L = 2.0 \times 10^{-2}$, the numerical computations seem to have been reasonably accurate in predicting the insensitivity to filler depth but the shift compared to the clean configuration implies there is some additional physics that is not been captured by the stability calculations.

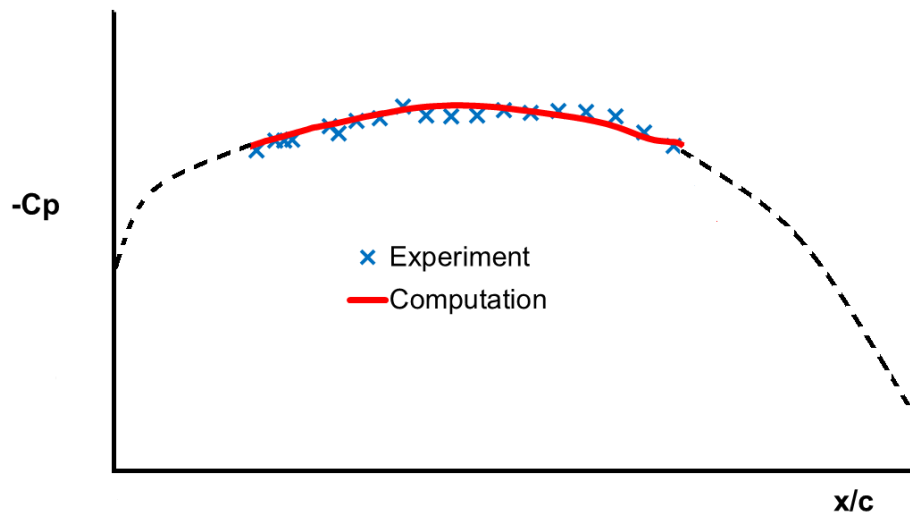


Figure 14: Comparison of experimental and numerical pressure coefficient for clean configuration.

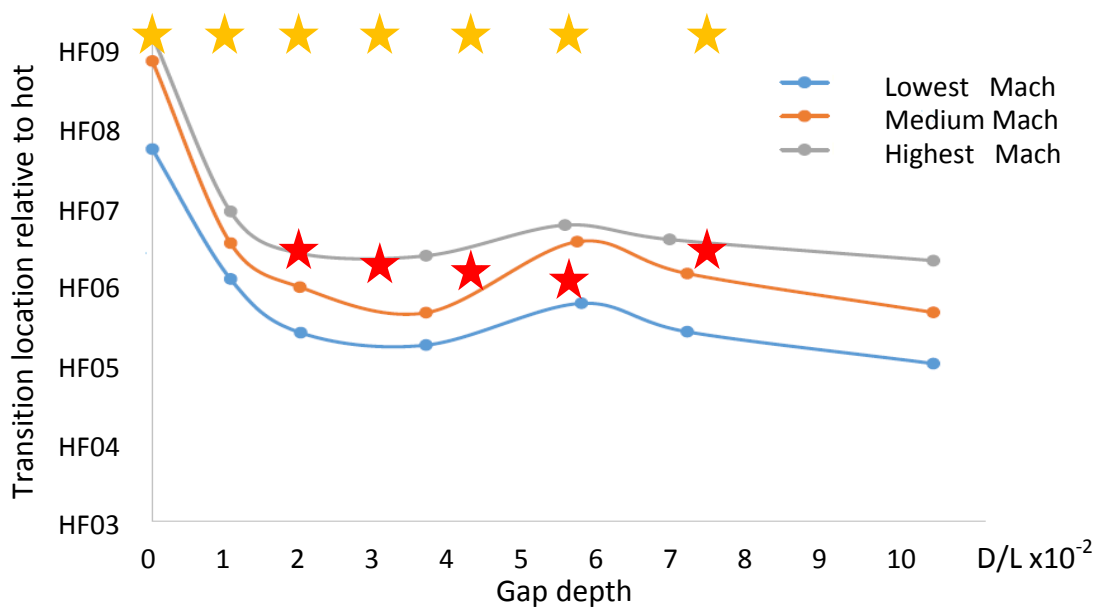


Figure 15: Comparison of experimental and numerical transition locations for various gap depths. Yellow and red stars are numerical transition based on critical N factors for clean and $D/L = 2 \times 10^{-2}$

More insights can be gleaned by examining the hot film data. The location of the hot film sensors is indicated by the arrows in the N factor plots. What stands out from comparing the hot film data for the clean configuration with that for $D/L=1.2 \times 10^{-2}$ and particularly with that for greater depths is the difference in the dominant frequency just before transition. For the clean configuration a peak in the PSD is seen at around 9 kHz at the location of hot film 9 where the rise in the PSD at higher

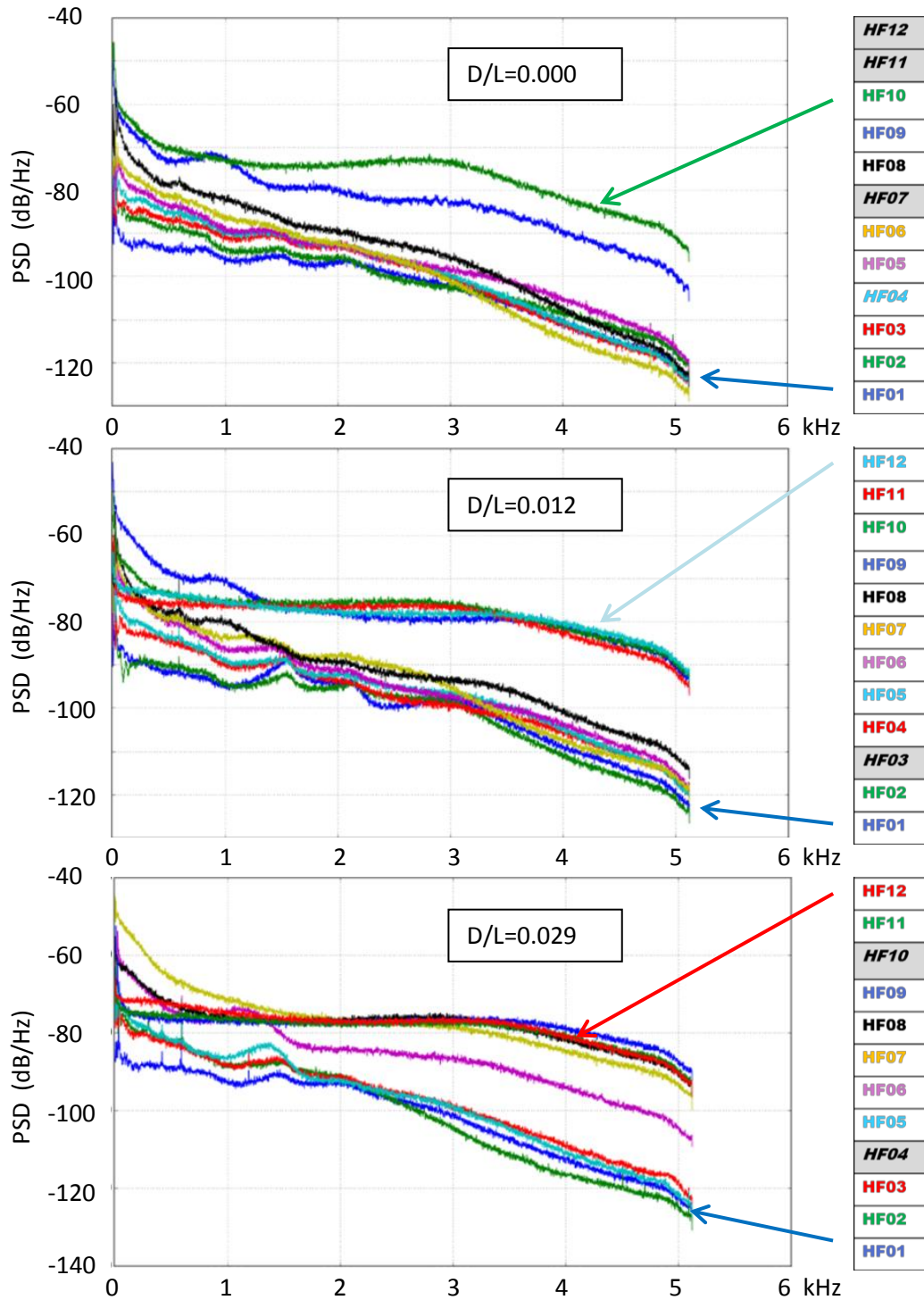


Figure 16: Comparison of experimental and numerical pressure coefficient for clean configuration (left)

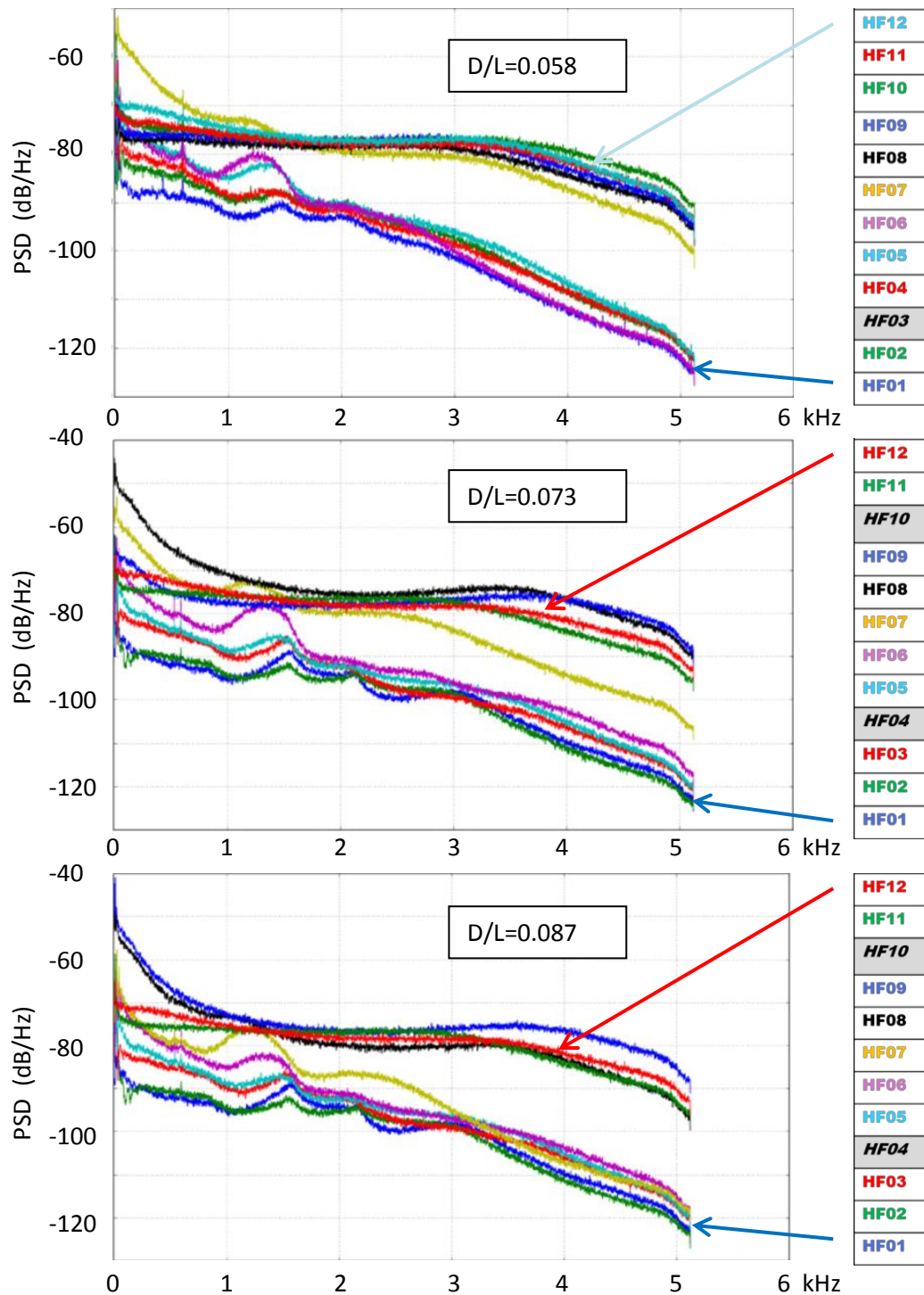


Figure 17: Comparison of experimental and numerical pressure coefficient for clean configuration (left)

frequencies indicates the onset of transition. For $D/L=1.2 \times 10^{-2}$ this peak occurs at a slightly higher frequency, closer to 10 kHz but for $D/L=2.9 \times 10^{-2}$ the peak occurs at a markedly higher frequency of about 12-13 kHz at the location of hot film 7 for transition onset. The results for $D/L=4.4 \times 10^{-2}$ (not shown) with an early transition to turbulence suggest the hot film was in a turbulent wedge and therefore should be discounted. For $D/L=5.8 \times 10^{-2}$ the peak occurs at 13-14 kHz at the location of hot film 6 whilst for $D/L=7.3 \times 10^{-2}$ the peak occurs at 12-13 kHz at a location around hot film 7. Here the result for $D/L=5.6 \times 10^{-2}$ indicates a forward movement rather than the rearward movement from TSP above.

Explanation for observed results

The dominance of a 9 kHz mode at the experimental transition location for the clean configuration is what is observed in the stability analysis, figure 16 (top). Also the dominance of a mode near 12kHz between hot films 6 and 7 for different depth filled gaps is also what is observed in figure 16 (bottom) to figure 17. What appears to be happening is there is a change in N factor for certain modes around 12 kHz which arises from the introduction of the filled gaps and this change in N factor remains more or less constant for filled gaps beyond depth ratio $D/L=2.9 \times 10^{-2}$. One explanation is that the gap is acting as a receptivity site introducing TS forcing over a range of frequencies. Newly introduced modes will only be significant compared to existing modes of the same frequency if the existing modes are of small amplitude and hence N factor. The newly introduced modes should also not be too far upstream of the neutral stability point for their frequency otherwise they will be heavily damped before they can grow. Thus the increment in N factor due to receptivity will be greatest for unstable modes which are near their initial amplitude (i.e. N factor close to zero) just upstream of the gap. Examination of figure 11-figure 13 reveals that this is indeed the case for modes of around 12 kHz for which the increment in N factor due to receptivity must be similar to the difference in critical N factors for clean and gap with $D/L=2 \times 10^{-2}$. The fact that the strength of the receptivity mechanism become almost invariant with filler depth can likewise be attributed to the recirculation inside the cavities which results in a virtual floor of zero x velocity that is at a near constant depth below the cavity opening as seen in figure 10.

Conclusions and further work

This study has shown, somewhat contrary to expectations, that for a filled gap representative of the junctions between leading edge and wingbox components on a natural laminar flow wing for conditions similar to cruise there is a marked forward movement in transition for gaps as shallow as $D/L=2.0 \times 10^{-2}$. However as the depth of the gap increases beyond this point there is no further movement. Stability calculations based on PSE predict no further movement beyond a certain depth but completely fail to predict the initial movement. It is suggested that this may result from the introduction of new modes at the gap through a receptivity mechanism. The transition causing frequencies at around 12 kHz are of small N factor at the gap and thus would be susceptible to such augmentation. The PSE computations have indicated that there is almost no lasting downstream effect of the filled gaps on the growth of transition causing modes. Although they do grow in passing over the gap they subsequently decay before following a similar growth further downstream to that seen for the clean configuration and no lasting mark is left from passage over the gap.

Future work should be targetted at better understanding and predicting a possible receptivity mechanism. The acoustic environment in the tunnel will be very different from that in flight and receptivity effects may be very different under flight conditions. Further work should also be directed towards understanding the optimal gap width. Initial studies have indicated much greater instability at larger depths when the gap width is increased and the saturation effect due to recirculation in the cavity formed by the gap is no longer so prevalent. Work should also be directed towards understanding the effect of unequal heights i.e. a step as well as a gap.

Acknowledgements

This work has been carried out within the ALFET project funded by Innovate UK.

References

1. N. Allen, S. Lawson, M. Maina, J. Alderman, "Qualification of the ARA TWT for laminar flow testing", RAES 2012
2. Thomas, C, Mughal, S.M., Gipon, M., Ashworth, R. and Martinez-Cava, A. 2016, "Boundary layer and stability methods for cross-flow over wavy surfaces", to appear in AIAA Journal
3. Herbert, T., 1997, "Parabolized stability equations. Annu. Rev. Fluid Mech. 29, 245-283.
4. Mughal, S., M., 2006, "Stability analysis of complex wing geometries: Parabolised stability equations in generalised non-orthogonal co-ordinates. AIAA Paper 2006-3222m doi 10.2514/6.2006-3222

Stabilization of crossflow instability with plasma actuators: Linearized Navier–Stokes simulations

Proc IMechE Part G:
J Aerospace Engineering
2020, Vol. 234(1) 68–78
! IMechE 2019
Article reuse guidelines:
sagepub.com/journals-permissions
DOI: 10.1177/0954410019842033
journals.sagepub.com/home/pig



Kean Lee Kang¹ , Richard Ashworth¹ and Shahid Mughal²

Abstract

This paper describes work carried out within the European Union (EU)-Russia Buterfli project to look at the control of transition-causing “target” stationary cross flow vortices, by the use of distributed plasma actuation to generate sub-dominant “killer” modes. The objective is to use the “killer” modes to control the “target” modes through a non-linear stabilizing mechanism. The numerical modelling and results are compared to experimental studies performed at the TsAGI T124 tunnel for a swept plate subject to a favorable pressure gradient flow. A mathematical model for the actuator developed at TsAGI was implemented in a linearized Navier–Stokes (LNS) solver and used to model and hence predict “killer” mode amplitudes at a measurement plane in the experiment. The LNS analysis shows good agreement with experiment, and the results are used as input for non-linear parabolized stability equation (PSE) analysis to predict the effect of these modes on crossflow transition. Whilst the numerical model indicates a delay in transition, experimental results indicated an advance in transition rather than delay. This was determined to be due to actuator-induced unsteadiness arising in the experiment, resulting in the generation of travelling crossflow disturbances which tended to obscure and thus dominate the plasma stabilized stationary disturbances.

Keywords

Flow control, plasma actuator, laminar turbulent transition, crossflow instability, linearized Navier–Stokes, parabolized stability equations

Date received: 12 December 2017; accepted: 24 February 2019

Introduction

The laminar-turbulent transition process over a swept transport wing under cruise conditions is dominated near the leading edge by crossflow instability. A common approach to controlling such disturbances in laminar wing design involves modifying the base flow of the boundary layer through suction to make it less susceptible to the growth of these instabilities. The system to achieve this incurs a drag penalty due to weight and actuation energy and raises reliability issues due to the complex network of pipes and pumps required. An alternative approach for controlling laminar-turbulent transition at the leading edge is through the promotion of “killer” crossflow modes that retard the growth of the most unstable “target” transition-causing modes via nonlinear interaction. This can be realized through excitation of the “killer” modes with distributed roughness elements or through an active approach involving spanwise periodic forcing, for example with plasmas, heat spots or blowing. Such active approaches for introducing disturbances require less energy compared to

approaches involving base flow modification because they involve only small perturbations to the flow over a much more limited chord-wise extent. Furthermore, such a dynamic method offers the possibility of varying the wavelength of the control perturbations to match the changing stability properties of the boundary layer under variations in cruise conditions that occur during a typical aircraft flight. Plasma actuators appear to be well suited to this role, offering the benefit of rapid response time and flexibility and are capable of producing the small velocity amplitudes that are required.

The viability of this approach has been explored in the European Union (EU)-Russia “Buterfli” project. In this project, a distributed dielectric barrier

¹Airbus Group Innovations, Bristol, UK

²Department of Mathematics, Imperial College, London, UK

Corresponding author:

Richard Ashworth, Airbus Group Innovations, Building 20A1, Bristol BS34 7QW, UK.

Email: richard.ashworth@airbus.com

discharge (DBD) plasma actuator was designed and built by the Joint Institute for High Temperatures (JIHT) in Russia and incorporated into a swept plate model at TsAGI¹ for testing in the T124 low turbulence tunnel under conditions where transition occurs due to crossflow instability. The effectiveness of the control through plasma actuation has been explored through the tunnel test and also through numerical simulations, the results of which are reported in this paper. This involves implementation of an actuator body force model developed by TsAGI and JIHT, as a field source term in a linearized Navier–Stokes (LNS) code.² Initial “killer” mode amplitudes determined with the LNS solver are used to set upstream “linear regime” conditions for the nonlinear parabolized stability equations (PSE, see Herbert³). Through solution of the PSE, the growth of the primary “killer” crossflow disturbance growth along with the transition-causing mode and their nonlinear interactions are studied to determine the possible transition delay achievable downstream. Although the predicted “killer” modes’ evolution match experimental downstream plane measurements, the predicted delay in transition from the numerical study does not correspond with experiment due to additional unsteady effects arising from the plasma actuation device.

The DBD actuator creates a wall jet flow effect, which with careful tuning of the plasma force distribution, can be confined to cause maximum effect within the viscous boundary layer. The wall jet arises with the introduction of a body force in the fluid, whereby the plasma actuator enhances the local fluid momentum.⁴ Plasma actuation produces a very concentrated and thus localized flow modification. Beyond the DBD placement region, the plasma-induced force reduces in magnitude fairly rapidly. Such extreme modifications to the basic field have been modelled until now by solutions to nonlinear boundary layer, direct Navier–Stokes (DNS) or Reynolds averaged Navier–Stokes (RANS) equations.

The physics of plasma actuation is a very complex problem, due to the multi-time and multi-spatial scales arising and in general requires precise numerical modelling of the convection-diffusion dynamics with the added complication of stiffness in the plasma reaction/ionization equations. This multi spatial and time modelling problem involves many stages (note Table 1, taken from Boeuf et al.,⁵ see also Regis⁶). The detailed analysis of Vidmar and Stalder⁷ indicates electron temperatures ranging between 1000 K and 10,000 K, with electron velocities of the order of 10^5 to 10^6 m/s (see Mertz & Corke),⁸ while fluid velocity is typically of order of 100 m/s. Complete numerical solutions of the fully coupled plasma-fluid dynamics in a consistent manner, in addition to Vidmar and Stalder,⁷ are the works of Unfer and Boeuf,⁹ Singh and Roy¹⁰ and Orlov¹¹ among others.

Table 1. Scales involved in DBD actuator modelling (Boeuf et al.,⁵ more detailed analysis of the disparate time and spatial scales is in Unfer and Boeuf⁹).

Temporal scales	Seconds
Maxwell relaxation time	10^{-12}
CFL time – electrons	10^{-12}
CFL time – ions	10^{-10}
Plasma formation	10^{-9}
Voltage generator	10^{-4}
Ambipolar diffusion	10^{-4}
Generated flow	10^{-2}
Spatial scales	Metres
Sheath	10^{-6}
Plasma dimension	10^{-3}
CFL	10^{-1}
Generated flow	10^{-1}

An alternative route has been that based on the electrostatic body force approximation (proposed by Shyy et al.¹²) and based on the key assumption, as alluded to above, that the many processes involved in the physics of the actuator operation (such as charge re-distribution) occur across widely separated time and spatial scales, so that the plasma generation may be treated in a quasi-steady manner. If one could directly implement an adequate approximation of the electrodynamic force in the Navier–Stokes equations, significant computational cost savings could be obtained for solutions of the complete plasma-fluid coupled equations.

The modelling challenge is thus that of developing a body-force model that captures the true induced force produced by the plasma hardware under flight or experimental operating conditions. A common practice is that of making measurements of the plasma actuator force vector under quiescent conditions and then applying the experimentally captured data in non-quiescent test conditions (see Serpieri et al.¹³).

The plasma actuator body force f , based on experiments and comparison with full and detailed numerical simulations of the plasma generation process, was found to be well approximated by Maxwell’s electrostatic force equations. Mertz and Corke,⁸ Orlov¹¹ and others solve the Poisson equation numerically to compute the electric potential distribution and thus the body force components. Shyy et al.¹² proposed a simple empirical model to characterise the DBD actuator, with the assumption that the plasma only arises above the actuator, in a triangular-shaped region with a linear decrease of the field strength from the maximum point, the field strength being maximal at the minimum separation between electrodes. The effect of increasing voltage was then modelled by a re-scaling of the triangular domain with voltage increments.

This simple model has been used in a number of Euler, DNS and RANS solvers¹⁴ to corroborate the flow control effects arising from the plasma actuator and with experimental verification. This simplistic expression of course requires very fine tuning and fitting to experiment, otherwise the total DBD force acting on the flow is erroneous at higher and *off design* voltages, giving rise to negative and unphysical force components. Singh and Roy¹⁰ and Grundmann et al.¹⁵ build upon this approach, by proposing a considerably more sophisticated and highly tuneable-induced body force vector. The basis of their model is detailed multiscale modelling of a two-dimensional DBD with a finite element time adaptive method. This detailed modelling confirms that the maximum plasma force arises in the overlap between the exposed and grounded electrodes. Assuming that an essentially time-averaged body force arises, and coupled to choosing initial conditions matched with realistic experimental data, they proposed that the electrodynamic force could be well approximated by exponential forms. Generally they find that for fixed frequency, the body force-induced jet velocity increases with the applied voltage.

Their body force expression is of course strictly two-dimensional, an accurate description of the electric field that is strongly tied to the electrode 3D-shape is a much more difficult problem to model and parameterise, which will be case and shape dependent. Disotell¹⁶ considers the implication of having a periodic array of shaped plasma actuators and studies them in a semi-empirical manner. More recent works concerned with controlling flow instabilities as opposed to flow separation are those of Wang et al.¹⁷ (with a nonlinear PSE plasma model) and Dorr and Kloker^{18–20} (compute and resource intensive DNS modelling). In addition to Ustinov et al.,¹ whose experiment we replicate in this paper numerically, experimental plasma control of crossflow instability using the killer mode concept has also been reported by Serpieri et al.¹³

In the PSE model of Wang et al.,¹⁷ a sensitivity analysis is undertaken of the effect of plasma on the nonlinear crossflow arising in the swept Hiemenz base flow. Due to the inability of the PSE to model the disturbance generation process arising from the plasma actuation itself, they model how a pre-existing crossflow disturbance state (generated by some other means) is modified as it convects through the plasma (i.e. a sensitivity analysis) region. In addition to this simplification, there is also the assumption of a very weak plasma momentum force, to enable the nonlinear PSE (NPSE) study to be feasible.

We investigate the feasibility of modelling plasma flow control through the linearized Navier–Stokes model. The plasma actuation within the LNS scheme of modelling the periodic spanwise actuation of stationary crossflow vortices is of an exploratory but novel nature. We add in the three-dimensional

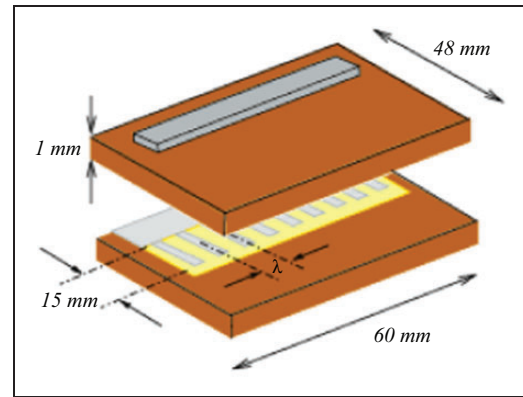


Figure 1. Sandwich actuator with control electrodes (JIHT report by Moralev et al.²⁵)

actuation capability by a smoothly varying step function (in the y -spanwise direction) to give periodic variations in span for the body-force source terms. Hence, the spanwise variation is simply a smoothed step up/down function (ranging between 0 and 1) which allows the plasma to be active in a specified fraction of the periodic box under investigation along similar lines as that shown in Figure 1. As remarked above, most work in plasma actuation has been based on making significant alterations to the flow, for example to control flow separation. The linearised Navier–Stokes model herein will be a valid model for magnitudes of the body-force source terms which lead to weak changes to the leading order basic field. Unlike using the full *brute-force* approach of Dorr and Kloker,¹⁸ the harmonic LNS route affords an efficient means of investigation of this relatively weak phenomenon. Not only does the LNS method, unlike the PSE model, capture the birth process of crossflow disturbance due to the plasma, but it also captures non-parallel and any detailed short-scale physical processes arising in the disturbance evolution. PSE models cannot model processes below a certain spatial resolution due to an inherent ill-posedness in the PSE equations and hence step-size restriction. This has been demonstrated in the context of surface roughness-induced stationary crossflow generation by Mughal and Ashworth.²¹ All of the LNS results reported in this paper were undertaken on a stand-alone workstation, with each LNS simulation taking less than 5 min for a highly resolved grid-independent computation.

The details of our numerical approach may be found in the paper of Thomas et al.,²² and below we focus on aspects of the plasma model and demonstrate the efficacy of our LNS model with comparisons with the experiment. The basis of our methodology is as follows: we utilise the LNS model for capturing the plasma-induced crossflow generation of the killer mode; and the amplitude of the killer mode predicted by the LNS model is then used to force the significantly more efficient nonlinear

PSE solver to investigate the control aspects of the study.

Experiment

The experiment in the TsAGI T124 tunnel has been described in detail in Ustinov et al.^{1,23} In summary, a flat plate with 35° sweep was subjected to a favorable pressure gradient flow on one surface through tunnel wall profiling. This was designed to promote the development of cross flow instabilities. Hot wire velocity profile measurements were made across three spanwise planes at distances of 250 mm, 350 mm and 600 mm from the leading edge. The last of these was expected to be close to the onset of transition. Extensive surface pressure data were also collected. Preliminary numerical studies^{23,24} had shown that the most amplified naturally occurring stationary cross flow mode was close to 7.5 mm in spanwise wavelength and this could most effectively be controlled through introduction of a “killer” mode having 2/3 of the spanwise wavelength, i.e. 5 mm. Thus, a DBD actuator was developed by JIHT to promote this particular mode through a periodic arrangement of electrodes.²⁵ This consisted of two embedded electrodes as shown in Figure 1. The lower embedded electrode included equidistantly spaced electrodes at the actuation wavelength ($\lambda=5$ mm) and an electrode width ($w=2$ mm). The DBD actuator was embedded in the plate with the downstream edge of the exposed electrode at a distance of 120 mm from the leading edge of the plate.

Measurement data were collected with and without actuation at a tunnel speed of 25 m/s which was equivalent to a virtual freestream of 31.9 m/s. The plasma actuation in the experiment, unlike the simulations reported in this paper, was found to advance rather than delay transition in the experiment. From the spectral velocity data, this was thought to be due to unsteady forcing by the plasma actuator which generated travelling crossflow modes alongside the stationary modes. The travelling modes were sufficiently unstable to trigger the early transition. Finding a way of eliminating this unsteadiness is one of the major technical challenges to be overcome if plasma actuators are to be used in this way. This will be the subject of future work. This paper describes numerical modelling of the actuators neglecting the unsteady effects and certainly the simulations indicate that the actuators should be able to produce a delay in transition, should it prove possible to eliminate and manufacture plasma actuators exhibiting reduced levels of unsteadiness during operation. Nevertheless, the numerical model of the actuator arising from the Butterfly project and our simulations has been successful in validating some aspects of the experiment, and indeed we find that plasma actuators can be used to control stationary crossflow vortices.

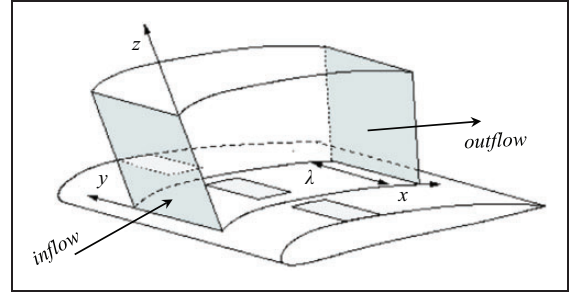


Figure 2. Computational domain of linearized Navier–Stokes solver for spanwise periodic roughness or body forcing in spanwise homogeneous flow.

Numerical model

Equations

The generation of the killer cross flow mode has been modelled through incorporation of a modified form of the TsAGI body force model²⁶ into a linearized Navier–Stokes (LNS) solver developed at Imperial College with support from Airbus Group Innovations.² As described in some detail in Mughal and Ashworth²¹ and Thomas et al.,²² the LNS equations are solved for spanwise periodic disturbances in a spanwise homogeneous base flow with a computational domain that encloses one period of the disturbance inducing roughness or plasma forcing as indicated in Figure 2.

The derivation of the LNS equations follows the usual route of decomposing the total unsteady flow \hat{q} , along the following ansatz

$$\hat{q}(x, y, z, t) = \bar{Q}(x, z) + \tilde{q}(x, y, z, t) \quad (1)$$

where t is a time variable, (x, y, z) spatial variables, \bar{Q} represents the steady spanwise invariant in y base flow velocity field, and \tilde{q} the disturbance state involving the velocity components $(\tilde{u}, \tilde{v}, \tilde{w})$ and pressure \tilde{p} . The steady pressure field is assumed to be invariant with (y, z) and thus $\bar{P} = \bar{P}(x)$ only. The disturbance state is then decomposed as follows

$$\tilde{q}(x, y, z, t) = \sum_{m=-N}^{m=N} q_{(m)}(x, z) e^{i(m\beta y - \omega t)} \quad (2)$$

In the above, a time harmonic and span periodic ansatz is assumed for the disturbance \tilde{q} , i.e.

$$\begin{aligned} \frac{\partial \tilde{q}}{\partial t} &= -i\omega q_{(m)} \\ \frac{\partial \tilde{q}}{\partial y} &= -im\beta q_{(m)} \end{aligned} \quad (3)$$

for a specified angular frequency and wavenumber pair $(\omega, m\beta)$, with $\beta = 2\pi/\lambda$. Substitution of the

above into the unsteady body-fitted Navier–Stokes equations, followed by neglect of nonlinear terms leads to the LNS equations (see Appendix 1). As our focus is on control of steady crossflow modes, from here on we set $\omega = 0$, while the integer m is used to model higher harmonics of the stationary crossflow which arise in the near field of the plasma actuation site, as well as to denote the same modes developing in our nonlinear PSE simulations (note equation (1)). For clarity, from here on we drop the suffix m -notation on the $q_{(m)}$ variable.

The plasma is represented by \hat{f}_k field source terms in the forced LNS momentum equations, while roughness is represented through a “wall” boundary condition obtained from a Taylor expansion in the total flow (base plus disturbance) in conjunction with the requirement that no slip is satisfied where the surface of the roughness would be (i.e. in the interior of the flow rather than the “wall”). Thus

$$q(x, y, 0) = -H(x, y) \frac{\partial \bar{Q}}{\partial z} \quad (4)$$

for a given height function H and base flow velocity $\bar{Q} = (\bar{U}, \bar{V}, \bar{W})$. The discretised LNS equations ultimately require the solution to a linear system of equations of the form

$$L\vec{q} = \vec{r} \quad (5)$$

where \vec{r} is constructed from either the field source terms involving \hat{f}_k for the plasma model developed by TsAGI, or and in combination with the roughness function H . The LNS operator L is derived through a fourth-order accurate finite difference discretization in x (the streamwise direction), a pseudo spectral discretisation in z and a Fourier decomposition in y the spanwise domain.

TsAGI-JIHT body force model for distributed actuation

Within the Buterfli project, a phenomenological body force model was formulated for the DBD actuator developed at JIHT. PIV measurements of the flow generated by the device were made by JIHT in quiescent conditions and the thrust generated by the device over one span period was determined through integration of the measured momentum flux on a control volume enclosing one spanwise period of the device. A value of $F_{x\Sigma} = 5.0 \times 10^{-6}$ N per period was arrived at for an actuation voltage of 3.2 kV, frequency of 190 kHz and electrode width of 2 mm. The forcing was observed from PIV to be restricted to a cuboidal domain immediately above the electrode of size 1.5 mm, 2 mm and 0.2 mm in the streamwise, spanwise and wall normal directions, respectively. Determination of the spanwise component of the forcing was more problematic as the symmetry

properties excluded the approach used for the streamwise component. However, an estimate was made that the spanwise component was $F_{y\Sigma} = 1.2 \times 10^{-6}$ N in each half of the cuboidal domain with the force having opposite directions in each half of the domain. The wall normal component of the force arising from the actuation was observed to be negligible compared to the wall tangential components and was therefore taken to be zero. TsAGI took this information from JIHT and combining it with insights gained from their parametric studies for canonical 2D (spanwise invariant) DBD actuators including in particular the location of force maxima, arrived at a more detailed model of the force distribution as a function of voltage. This is described in some detail in Ustinov and Rusianov.²⁶

The field source terms \hat{f}_k in the forced LNS (see Appendix 1) arise on performing a fast Fourier transform (FFT) in y of expressions²⁶ for the longitudinal and spanwise components of the force density (N/m³)

$$\begin{aligned} F_x &= \frac{1}{x_0 y_0 z_0} F_{x\Sigma} \theta(\hat{x}) \frac{\hat{x}\hat{z}}{\pi^{1/2}} e^{-(\hat{x}^2 + \hat{y}^2/4 + \hat{z})} \\ F_y &= \frac{1}{x_0 y_0 z_0} F_{y\Sigma} \theta(\hat{x}) \hat{x}\hat{y}\hat{z} e^{-(\hat{x} + \hat{y} + \hat{z})} \end{aligned} \quad (6)$$

in which the non-dimensional coordinates are with respect to the location of the force maximum, i.e. $\hat{x} = x/x_0$, $\hat{y} = y/y_0$, $\hat{z} = z/z_0$. The coordinates of the force maximum location depending linearly on the ratio of the applied voltage to the discharge voltage are as follows

$$\begin{aligned} x_0 &= F_{x1} \left(\frac{V}{V_0} - 1 \right) \\ y_0 &= F_{y1} \left(\frac{V}{V_0} - 1 \right) \\ z_0 &= H_1 V \end{aligned} \quad (7)$$

The integrated values (for one electrode intersection) of the force density components depend quadratically on the voltage ratio

$$\begin{aligned} F_{x\Sigma} &= A_x \left(\frac{V}{V_0} - 1 \right)^2 \\ F_{y\Sigma} &= A_y \left(\frac{V}{V_0} - 1 \right)^2 \end{aligned} \quad (8)$$

The integration is over one side (left or right) for the y component; θ is a Heaviside function to ensure forces are zero for negative x . The various coefficients have been empirically determined to have the following values: $A_x = 1.82 \times 10^{-5}$ N, $A_y = 4.37 \times 10^{-6}$ N, $F_{x1} = 1.43$ mm, $F_{y1} = 0.65$ mm (changed from $F_{y1} = 0.95$ mm in original model²⁶) and $H_1 = 0.0312$ mm/kV. These parameters stretch the plasma field of influence in the streamwise and

wall-normal directions, and along with the use of the Heaviside function θ affords maximum flexibility to fine-tune the plasma model with data from experiment.

The LNS simulations with the implemented model have been applied to a boundary layer corresponding to the experimental conditions for a tunnel reference velocity of 25 m/s as described in Ustinov et al.¹ The boundary layer or the steady base flow represented by $\bar{Q}(x, z)$ in equation (1) was computed with the

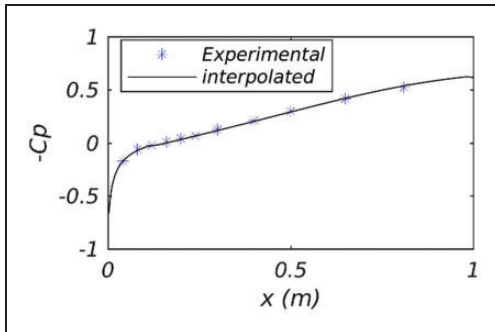


Figure 3. Pressure coefficient C_p based on virtual free stream conditions and measured data.

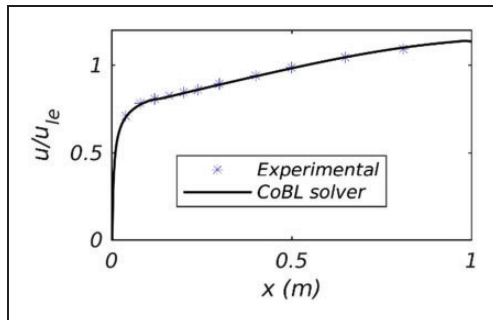


Figure 4. Comparison of computed and measured edge velocity.

non-similar boundary layer solver CoBL,²⁷ using an equivalent virtual freestream velocity of 31.9 m/s together with the corresponding pressure coefficient interpolated from experimental pressure measurements is shown in Figure 3.

The interpolated pressure data were then used to compute three-dimensional boundary-layer profiles for the subsequent disturbance control simulations involving either LNS or nonlinear PSE. As a check on the correct implementation of the surface pressure data, the CoBL recomputed boundary-layer edge velocity distribution was found to compare very well with the experimentally measured edge velocities, as may be seen in Figure 4. This is a crucial check since instability analysis is known to be very sensitive to any inaccuracies or inconsistencies in the boundary-layer computations. The resulting streamwise and spanwise velocity profiles computed by our boundary-layer solver CoBL are displayed in non-dimensional form in Figure 5 at a number of streamwise positions. Validations and adequacy of the CoBL laminar boundary-layer computed solutions and comparison with RANS-derived boundary layer profiles were previously reported in Thomas et al.²⁷

Results and discussion

Stability analysis with a linear PSE solver for a range of stationary cross-flow modes revealed a most amplified mode of around 8 mm, as shown in Figure 6(a), which is in line with previous analysis of Ustinov et al.²³ and Hein.²⁴

A comparison between linear PSE for the 5 mm “killer” mode generated with our LNS simulation of a cylindrical roughness element placed within a periodic box of $\lambda = 5.0$ mm span showed good agreement with the amplification based N-factor, as shown in Figure 6(b). The precise details of the roughness element are unimportant, since we use it simply as a means to generate the linear stationary crossflow disturbance.

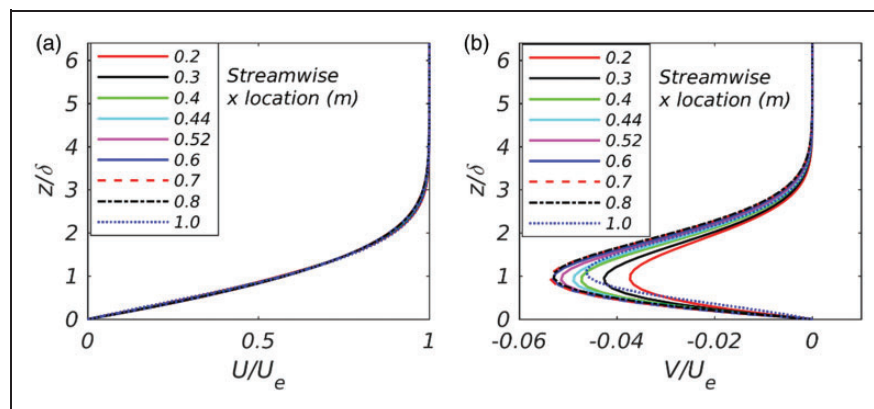


Figure 5. Non-dimensional boundary layer profiles: component in directions of inviscid stream (a) and cross-flow component (b). Velocity components and wall normal distance are normalized by local boundary layer edge velocity displacement thickness respectively.

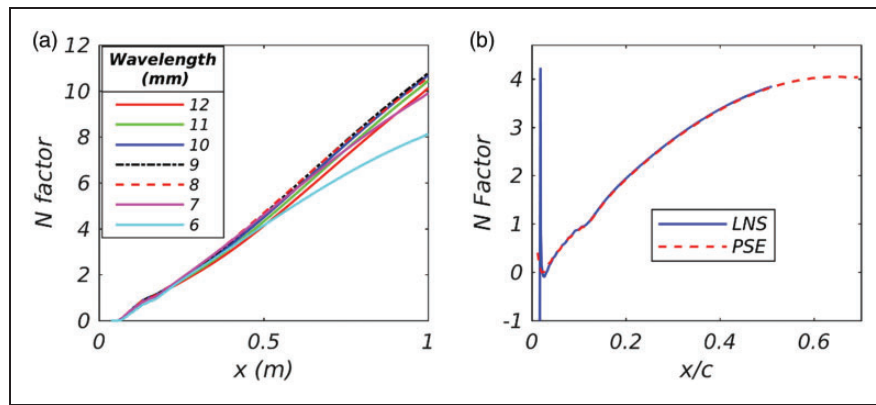


Figure 6. Linear PSE for a range of span wavelengths (a) and comparison between linear PSE and LNS simulation for the 5 mm mode (b).

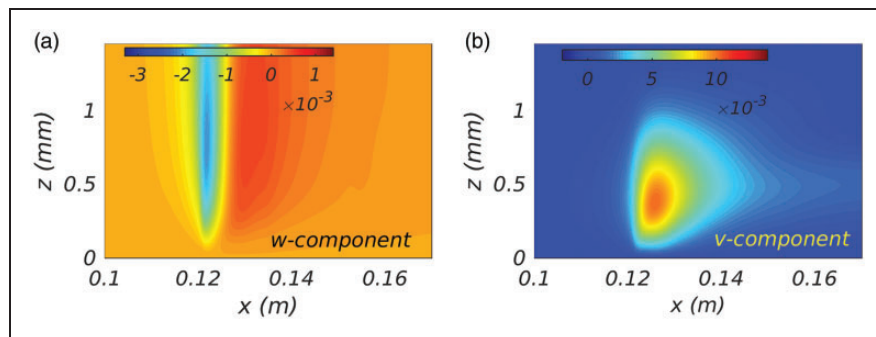


Figure 7. Base flow modification, mean flow distortion (0, 0) mode due to plasma actuation (applied voltage 4.0 kV). Normal to leading edge wall normal w and spanwise v -disturbance fields.

The LNS solver was then applied with the plasma actuator for a range of applied voltages from 3.0 kV to 4.0 kV for a 5 mm domain spanwise width. Stationary crossflow ‘killer’ modes of varying magnitude are thus directly generated by the imposed varying plasma forcing. A primary concern before analysis can be conducted is to confirm the implicit assumption that the plasma body force induces only weak variations to the base flow. This is confirmed by examination of the induced steady base flow correction, the so-called (0,0) mean flow distortion disturbance, computed by the LNS on setting $m = 0$ in equation (2). Figures 7 and 8(a) show the w , v and u components of the (0,0) mode disturbance near the plasma activation site ($x = 0.12$ m). The u -component of the (0,0) mode is the largest in magnitude and indicates fluid to be accelerated in the normal to leading edge streamwise and spanwise directions while also being drawn in towards the surface at the commencement of the actuation (i.e. the relatively larger negative valued w -field in Figure 7(a)). Observe that the plasma effect is quite localized (concentrated at about $x = 0.12$ m) for the (w , v)-fields, where w is the weakest field followed by the spanwise v -component a factor of ten larger, but by about $x = 0.14$ all three velocity components have diminished in magnitude significantly.

The corresponding streamwise (0,1) u -disturbance killer modes birth (at $x = 0.12$) and subsequent continuous growth in amplitude with x are shown in Figure 8(b). The fairly rapid growth in x of the (0,1) disturbance by about $x = 0.25$ is then sizable enough for nonlinearity to be significant and this then induces the re-growth of the (0,0) u -mode (note Figure 8(a)). That this re-growth of the mean flow disturbance is due to nonlinearity may be ascertained from Figure 9, which shows maximum amplitude evolution with x of a number of higher harmonics (including the (0,0) mode) generated by the plasma field with our Navier–Stokes solver run in true linear mode for applied voltages of 3.0 kV and 4.0 kV. Observe that the (0,0) disturbance amplitude for both voltages keeps on decreasing with x , downstream of the $x = 0.12$ generation site. Moreover, note all the near field higher harmonic-generated modes rapidly decay in magnitude too, apart from the fundamental ‘killer’ (0,1) mode. Finally, we also show results of our linear PSE, which are in very good agreement with the LNS results once the (0,1) crossflow disturbance has established itself. Since the amplitude for the 5.0 mm induced killer mode is to be used in non-linear PSE analysis to investigate the control of the most rapidly growing 7.5 mm disturbance, this

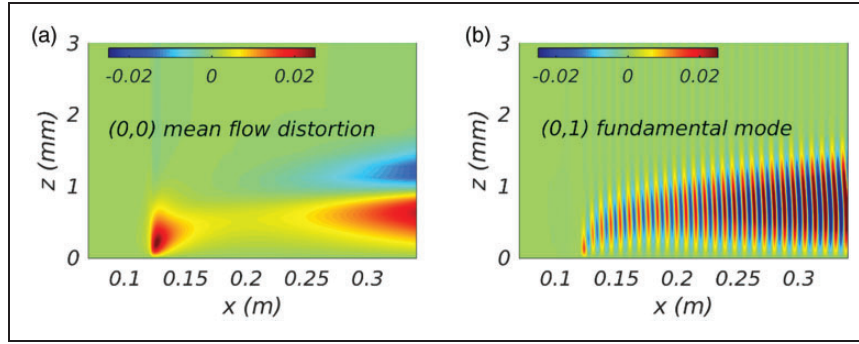


Figure 8. Stationary crossflow streamwise u -disturbance field generation and evolution. Plasma actuation of applied voltage of 4.0 kV is concentrated at about $x = 0.12$ m. (a) Shows the (0,0) mean flow distortion u -disturbance, while plot (b) shows the fundamental (0, 1) u -disturbance.

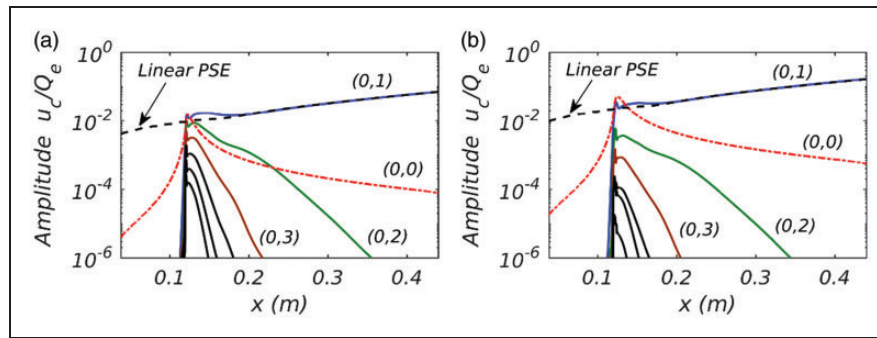


Figure 9. Left plot (a) shows 3.0 kV near field, while right plot (b) is the 4.0 kV generated near field computed with LNS, also shown is the (0, 1) linear PSE result (dashed black curves). Observe that in the 4.0 kV simulation, the plasma-induced mean flow correction (0,0) is much stronger and persists downstream of the plasma site.

good agreement between PSE and LNS provides significant confidence in the adequacy of using non-linear PSE analysis in the plasma control work presented below.

The downstream development of the peak amplitude in the normal to leading edge component of the velocity disturbance killer mode for a range of plasma voltages is shown in Figure 10. The linear growth is seen to commence in all cases at about 200 mm from the leading edge, but a loss in effectiveness is also suggested with increasing applied voltage, since the change in disturbance amplitude curves going from 3.8 kV to 4.0 kV appears to be decreasing and/or attaining an upper maximum limit. The development of the disturbance was compared with experimental measurements made at a plane 250 mm from the leading edge as shown in Figure 11, where the disturbance u_o and associated dimensionalising velocity U_o are defined in experimental coordinates along the free-stream direction. This reveals an almost linear increase in amplitude with applied voltage for both the experiment and the numerical model with remarkably good agreement between the two. The amplitude for the highest voltage induced 5.0 mm killer mode was used in subsequent NPSE analysis to investigate the control of the most rapidly growing 7.5 mm disturbance.

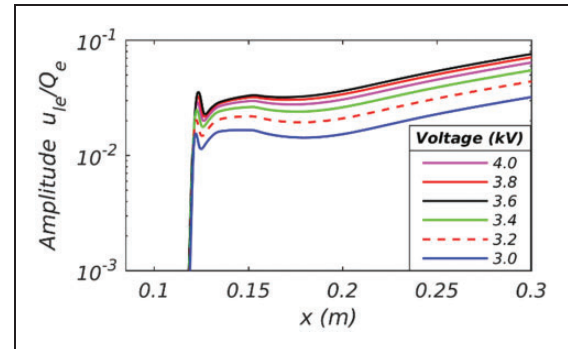


Figure 10. Profile maximum disturbance amplitude evolution of killer mode for increasing actuation voltages (3.0, 3.2, 3.4, 3.6, 3.8 and 4.0 kV).

The (0, 3) control mode amplitude at $x = 0.25$ m obtained from the LNS model with actuator voltage of 4.0 kV has been used to initialize an appropriate initial killer mode amplitude in a NPSE computation, the results of which are shown in Figure 12. Note from here on, we refer to the same 5.0 mm plasma generated, previously denoted (0,1) mode corresponding to wavenumber $\beta = 2\pi/\lambda_{5\text{mm}} = 3\beta_{PSE}$, as the (0,3) killer mode in the NPSE control analysis with a redefinition of the spanwise wavenumber $\beta_{PSE} = 2\pi/\lambda_{15\text{mm}}$.

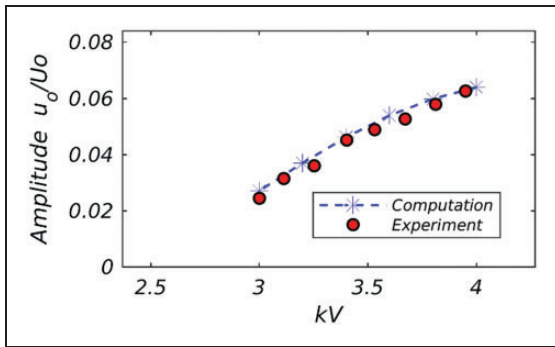


Figure 11. Amplitude of killer mode as a function of the actuator voltage on the measurement plane, 0.25 m from the leading edge.

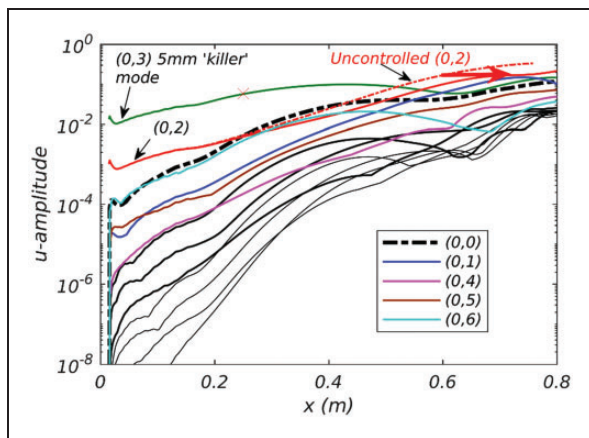


Figure 12. Non-linear PSE computation showing interaction of (0, 3) killer mode generated by plasma actuation with (0, 2) target mode for (0, 1) fundamental mode of 15 mm. Red star shows amplitude from LNS calculation. The u -amplitude is scaled with Q_e the local boundary-layer edge total velocity.

The amplitude of the transition causing target (0, 2) mode ($= 2\beta_{PSE}$) with spanwise wavelength of 7.5 mm was set to correspond with the experimental measurement data reported in Ustinov et al.¹ Comparison of the uncontrolled and controlled growth of the target mode indicates a clear reduction in amplitude and an expected delay in transition of about 0.1 m. In reality, as was mentioned previously, there was a forward movement in transition in the experiment¹ where this is explained in terms of the excitation of transition causing travelling modes by the plasma actuator due to the plasma-induced unsteady velocity fluctuations which increase linearly with actuation voltage. This unsteadiness in the actuation is not captured in the actuator model described here and thus it is not possible to capture the generation of the travelling modes. However, the work does indicate that if the physical realization of the distributed plasma actuator can be redesigned so as to lessen the unsteady component of the forcing then it can be expected to be capable of producing a delay in transition due to cross-flow instability and this should be a focus for future

plasma actuator development. Moreover, scaling arguments reported within the Buterfli project²⁸ have indicated that the approach based on distributed plasma actuation could be energetically favourable when considered for application at flight scale thus providing an important practical incentive for continued development of this technology.

Conclusions

It has been demonstrated that the generation of “killer” modes by plasma actuation can be modelled through a linear Navier–Stokes approach which when used in conjunction with a non-linear PSE solver can make a prediction about the delay in transition arising from the actuation. Although the numerical model has been shown to give good agreement with experiment for the amplitude of the killer modes on a downstream plane, the subsequent non-linear interaction leading to suppression of the transition causing “target” mode and delay in transition is not what was observed in experiment. This is due to unsteady effects in the plasma actuation and the generation of transition causing travelling crossflow modes in the experiment. Nevertheless, should future refinements in the actuator hardware permit the elimination of the unsteady actuation effects, then the modelling approach outlined provides a good basis from which to predict the effectiveness of such actuators.

We have also demonstrated an efficient high fidelity LNS-based methodology, which allows analysis to be undertaken relatively quickly. Comparison with linear PSE is equally good, and our LNS method may be used to provide initial amplitudes to initialize non-linear PSE simulations. The coupled LNS-NPSE approach reproduces nearly DNS-like results in fractions of the time and CPU hardware resources compared to full DNS simulations. The LNS method models the generation of crossflow disturbances, i.e. receptivity directly, and quite remarkable agreement with experiment has been obtained. The incorporation of body force terms within the LNS framework, we believe is ideally suited for the study of propagation, generation and control of instabilities in plasma-based flow control when the instabilities to be controlled and manipulated are relatively weak.



Declaration of Conflicting Interests

The author(s) declared no potential conflicts of interest with respect to the research, authorship, and/or publication of this article.

Funding

The author(s) disclosed receipt of the following financial support for the research, authorship, and/or publication of this article: This work was completed within the Buterfli project supported by the European Commission under the 7th Framework Programme [Grant Agreement 605605].

ORCID iDs

Kean Lee Kang  <http://orcid.org/0000-0001-8449-2863>
 Richard Ashworth  <http://orcid.org/0000-0003-4446-9559>

References

1. Ustinov MV, Moralev IA, Sboev DS, et al. *Experimental study of cross-flow dominated transition control by DRE-type actuator*. Report on Butterfli Project D3.20, 2017.
2. Mughal MS. Advanced transition prediction – development of linearised Navier-Stokes receptivity methods. Imperial College final report prepared for EADS-IW no. IW103511, 2012.
3. Herbert T. Parabolized stability equations. *Annu Rev Fluid Mech* 1997; 29: 245–283.
4. Riherd M and Roy S. Linear stability analysis of a boundary layer with plasma actuators. In: *50th AIAA aerospace sciences meeting including the new horizons forum and aerospace exposition*, Nashville, Tennessee, 9–12 January 2012, paper no. AIAA 2012-0290.
5. Boeuf J, Lagmich Y, Callegari T, et al. New insights in the physics of DBD plasma actuators for flow control. In: *46th AIAA aerospace sciences meeting and exhibit*, Reno, Nevada, USA, 7–10 January 2008, paper no. AIAA 2008-1376.
6. Regis SQ. *Numerical optimisation of boundary-layer control using dielectric barrier discharge plasma actuators*. PhD Thesis, Technische Universität, Darmstadt, 2009.
7. Vidmar R and Stalder K. Air chemistry and power to generate and sustain plasma: plasma lifetime calculations. In: *41st aerospace sciences meeting and exhibit*, Reno, Nevada, USA, 6–9 January 2003, paper no. AIAA 2003-1189.
8. Mertz BE and Corke TC. Single-dielectric barrier discharge plasma actuator modelling and validation. *J Fluid Mech* 2011; 669: 557–583.
9. Unfer T and Boeuf JP. Modelling of a nanosecond surface discharge actuator. *J Phys D Appl* 2009; 42: 194017.
10. Singh KP and Roy S. Force approximation for a plasma actuator operating in atmospheric air. *J Appl Phys* 2008; 103: 013305.
11. Orlov DM. *Modelling and simulation of single dielectric barrier discharge plasma actuators*. PhD Thesis, Notre Dame, Indiana, USA, 2006.
12. Shyy W, Jayaraman B and Andersson A. Modelling of glow discharge-induced fluid dynamics. *J Appl Phys* 2002; 92: 6434.
13. Serpieri J, Venkata SY and Kotsonis M. Conditioning of cross-flow instability modes using dielectric barrier discharge plasma actuators. *J Fluid Mech* 2017; 833: 25.
14. Jayaraman B and Shyy W. Flow control and thermal management using dielectric glow discharge concepts. In: *33rd AIAA fluid dynamics conference and exhibit*, Orlando, Florida, USA, 23–26 June 2003, paper no. AIAA 2003-3712.
15. Grundmann S, Klumpp S and Tropea C. Experimental and numerical investigations of boundary-layer influence using plasma-actuators. In: King (ed) *Active flow control*. Berlin Heidelberg: Springer-Verlag, 2007, NFM 95, pp.56–68.
16. Disotell KJ. *A semi-empirical model of the wall-normal velocity induced by flow-shaping plasma actuators*. Graduate Thesis, Ohio State University, USA, 2010.
17. Wang Z, Wang L and Fu S. Control of stationary cross-flow modes in swept Hiemenz flows with dielectric barrier discharge plasma actuators. *Phys Fluids* 2017; 29: 094105.
18. Dorr PC and Kloker MJ. Crossflow transition control by upstream flow deformation using plasma actuators. *J Appl Phys* 2017; 121: 063303.
19. Dorr PC and Kloker MJ. Transition control in a three-dimensional boundary-layer flow using plasma actuators. *Proc IUTAM* 2015; 14: 469–478.
20. Dorr PC and Kloker MJ. Transition control in a three-dimensional boundary layer by direct attenuation of nonlinear crossflow vortices using plasma actuators. *Int J Heat Fluid Flow* 2016; 61(Part B): 449–465.
21. Mughal SM and Ashworth RM. Uncertainty quantification based receptivity modelling of crossflow instabilities induced by distributed surface roughness in swept wing boundary layers. In: *43rd fluid dynamics conference, fluid dynamics and co-located conferences*, San Diego, California, USA, 24–27 June 2013, paper no. AIAA 2013-3106.
22. Thomas C, Mughal SM and Ashworth RM. On predicting receptivity in a compressible infinite swept wing boundary layer. *Phys Fluids* 2017; 29: 034102.
23. Ustinov MV, Vozshdaev VV, Teperin LL, et al. *Preparatory CFD studies of the model for cross-flow realization in the flat plate boundary layer*. Report on Butterfli project D3.2, 2016.
24. Hein S. *Report on the results from non-linear instability analysis for the TsAGI T124 w/t experiment*. Report on Butterfli project D3.7, 2016.
25. Moralev I, Sherbakova V, Bituryn V, et al. *Properties, operations and induced flowfield of the plasma actuators with spanwise periodic microdischarges*. Report on Butterfli project D3.13, 2016.
26. Ustinov MV and Rusianov DA. *Improved models of volume force and heat release induced by DBD actuators*. Report on Butterfli project D3.21, 2017.
27. Thomas C, Mughal SM, Gipon M, et al. Stability of an infinite swept boundary layer with surface waviness. *AIAA J* 2016; 54: 3024–3038.
28. Ashworth R and Alderman J. *Aircraft level assessment and recommendations arising from WP3*. Report on Butterfli project D3.26, 2017.

Appendix I

Incompressible body fitted linearised Navier–Stokes disturbance equations:

Flow variables are the three velocity terms, $(\bar{U}, \bar{V}, \bar{W})$ denoting the basic steady flow in the chordwise (x), spanwise (y) and wing-normal (z) directions, and the associated velocity disturbance states (u, v, w) and pressure disturbance p . Body surface curvature terms are denoted by κ and χ . Here κ is the local body curvature, while χ is given as follows

$$\chi = \frac{1}{1 - \kappa y} \quad (9)$$

$$\chi u_x + w_z - \kappa \chi w + im\beta v = 0$$

$$\begin{aligned} \frac{u_{zz} + \chi^2 u_{xx}}{R} - u \left(im\beta\bar{V} + \frac{m^2\beta^2 + \kappa^2\chi^2}{R} + \chi\bar{U}_x - \kappa\chi\bar{W} \right) \\ - \chi P_x - \left(\bar{W} + \frac{\kappa\chi}{R} \right) u_z + (\kappa\chi\bar{U} - \bar{U}_z) w \\ - \chi\bar{U}u_x - \frac{2\kappa\chi^2}{R} w_x + \hat{f}_x = 0 \end{aligned} \quad (10)$$

$$\begin{aligned} \frac{w_{zz} + \chi^2 w_{xx}}{R} - w \left(im\beta\bar{V} + \frac{m^2\beta^2 + \kappa^2\chi^2}{R} + \bar{W}_z \right) \\ - P_z - \left(\bar{W} + \frac{\kappa\chi}{R} \right) w_z - (2\kappa\chi\bar{U} + \chi\bar{W}_x) u \\ - \chi\bar{U}w_x + \frac{2\kappa\chi^2}{R} u_x + \hat{f}_z = 0 \end{aligned} \quad (11)$$

$$\begin{aligned} \frac{v_{zz} + \chi^2 v_{xx}}{R} - v \left(im\beta\bar{V} + \frac{m^2\beta^2}{R} \right) - im\beta P - \bar{V}_z w \\ - \left(\bar{W} + \frac{\kappa\chi}{R} \right) v_z - \chi\bar{U}v_x - \chi\bar{V}_x u + \hat{f}_y = 0 \end{aligned} \quad (12)$$

In the above, R is an appropriately defined Reynolds number.



Destabilization of Stationary and Traveling Crossflow Disturbances Due to Steps over a Swept Wing

Emma E. Cooke^{*}, Shahid Mughal[†] and Spencer J. Sherwin[‡]
Imperial College London, London, United Kingdom, SW7 2AZ

Richard Ashworth[§] and Stephen Rolston[¶]
Airbus Wing Integration Centre, Building 07Y, Bristol, United Kingdom, BS34 7PA

Destabilization effects of forward facing steps, backward facing steps and bumps on stationary and traveling crossflow disturbances are investigated computationally for a 40° infinite swept wing. Step and bump heights range from 24% to 53% of the boundary layer thickness and are located at 10% chord. The spectral/hp element solver, Nektar++, is used to compute base flow profiles with an embedded swept wing geometry. Parabolized Stability Equations (PSE) and Linearized Harmonic Navier-Stokes (LHNS) models are used to evaluate growth of convecting instabilities. The paper describes derivations of the PSE and LHNS models which accurately solve for the perturbed field over the very localized and rapid variations imposed by the surface step-features. Unlike the PSE, which suffer from a stream-wise numerical step size restriction, the LHNS are a fully elliptic set of equations which may use arbitrarily fine grid resolution. Unsurprisingly, the PSE codes fail to capture the effect of abrupt changes in surface geometry introduced by the steps features. Results for the LHNS and roughness incorporating LHNS are given for the varying step types. Comparisons are made between the LHNS model and direct numerical simulations involving the time-stepping linearized Navier-Stokes solver in the Nektar++ software suite. Most previous work in the topic area has focused on Tollmien-Schlichting perturbations over two-dimensional flat plate flows or airfoils, the novelty of this work lies with analyzing crossflow instability over a swept wing boundary-layer flow with step features.

Nomenclature

x_1	=	Stream-wise body fitted co-ordinate
x_2	=	Wall-normal body fitted co-ordinate
x_3	=	Span-wise body fitted co-ordinate
s	=	Stream-wise co-ordinate in computational domain
Y	=	Wall-normal co-ordinate in computational domain
z	=	Span-wise co-ordinate in computational domain
u	=	Stream-wise velocity in computational domain
v	=	Wall-normal velocity in computational domain
w	=	Span-wise velocity in computational domain
h	=	Function for step or roughness profile
c	=	Chord
t	=	Time
x_b	=	Beginning of roughness location in stream-wise body fitted co-ordinates
x_e	=	End of roughness location in stream-wise body fitted co-ordinates
b_l	=	Bubble length
b_h	=	Bubble length with respect to roughness height

^{*}PhD Candidate, Mathematics Department, emma.cooke13@imperial.ac.uk

[†]Lecturer, Department of Mathematics, s.mughal@imperial.ac.uk

[‡]Professor, Department of Aeronautics, s.sherwin@imperial.ac.uk

[§]Research Engineer, Airbus Group Central Research and Technology, r.ashworth@airbus.com

[¶]Research Projects Leader XRV, Airbus Group Central Research and Technology, s.rolston@airbus.com

b_w	=	Bubble length with respect to roughness width
h_w	=	Roughness width
α	=	Stream-wise wave number
β	=	Span-wise wave number
ω	=	Frequency of disturbance
N	=	N-factor
i	=	Imaginary unit
j	=	index quantity
ϵ	=	Negligible quantity
$c.c.$	=	Complex conjugate
Δx_1	=	Length between stream-wise station locations
δ_h	=	Boundary Layer thickness at roughness location
y_c	=	Height of crossflow vortex core
\hat{f}	=	Forcing vector
\mathcal{L}	=	Matrix
Re_δ	=	Reynolds number based on boundary layer thickness

Subscript

i	=	Imaginary component
r	=	Real component
\dagger	=	Complex conjugate
e	=	Boundary layer edge value
$'$	=	Stream-wise derivative term

Superscript

$-$	=	Mean flow quantity
\sim	=	Perturbed flow quantity
\wedge	=	Shape function

I. Introduction

Drag reduction is one of the most important objectives for aircraft manufacturers today. An aircraft with lower drag, is not just more economical but also more environmentally friendly, which is inevitably becoming an ever growing concern. Fuel efficiency can be increased through a number of modifications to the aircraft but a major focus is on the construction of a swept laminar flow wing [1]. Large aircraft of today feature turbulent boundary layers on the majority of the exposed wetted surface, resulting in viscous drag that is five to ten times larger than a laminar boundary layer [2]. Achieving and maintaining laminar flow on a wing is hindered by surface imperfections which may be present on the wing. These imperfections can act as destabilization sites and may arise from rivets, leading edge to wing box junction tolerances, or even insect contamination. The presence of these *roughnesses*, or very localized surface imperfections, which occur primarily in the form of steps or bumps and interact with pre-existing instabilities within the laminar boundary layer. This promotes instability growth causing earlier transition, a thickening of the boundary layer and hence, increasing shear stress over much of the surface. This can completely eradicate any drag reduction benefit obtained from the laminar flow wing.

Instabilities occur in the boundary layer through various receptivity mechanisms. Disturbances may arise through interactions involving acoustic noise, free stream turbulence or / and in combinations with surface roughness features. The amplitude of disturbance present will define the pathway taken, whether it be linear, non-linear, transient, or bypass, to reach transition [3]. Since the disturbance of interest is relatively small, the focal pathway will be through the linear growth regime. Of course, these instabilities can be simulated with direct numerical simulation (DNS) but pouring huge amounts of computational time and resource into predicting these growths is not feasible for industrial design purposes. Consequently, there is motivation for rapid tools that can accurately and efficiently predict transition location without utilizing huge computational resource.

In the past, industry has used a semi-empirical method, e^N , coupled with traditional Linear Stability Theory (LST),

to predict the growth of an instability [4]. Essentially, exponential amplification of disturbances from inception to transition are specified through a calibrated N-factor, the critical N-factor is then determined from flight test data. This still remains a very appealing approach for industry, however in circumstances when a surface roughness is present, the flow in its vicinity is subject to large non-parallelism and LST breaks down. There exist other, superior, approaches which take into account non-parallel effects and surface curvature and can be extended to model non-linear interaction of modes. One of these is through solution of the parabolized stability equations (PSE) [5, 6]. However, even the PSE have been shown to be invalid when the width of the roughness is of the same length scale as the instability [7], since correctness of the mathematical model is constrained by a step size restriction [8]. The only methods remaining which are able to properly capture the effect for small and abrupt changes to surface topography are DNS, which have already been deemed infeasible for industry, and are generally used for further understanding of physics and validation of methods; asymptotic methods, such as the local scattering approach by Wu and Dong [7], which isolate dominant physics in a flow are limited in the parametric range under which they are constructed and finally, the linearized harmonic Navier-Stokes equations (LHNS) [9, 10], which are the most appealing as they do not suffer the step size restriction of PSE nor the computation cost of DNS.

Research has generally been dominated by investigating convection of Tollmien-Schlichting waves over steps and bumps on unswept flat plates [11-15] or two-dimensional (2D) airfoil models [16-18]. However, an important contributor for destabilizing swept wing laminar boundary layers are crossflow instabilities (CFI), which makes the application of these studies to swept wing flows very limited. Over recent years investigations have taken place for steps and bumps on swept flat plate flows and a few infinite swept wings which feature inflectional velocity profiles, characteristic of CFI. Invariably, if the steps or local features change rapidly enough (*i.e.* surface discontinuity) a laminar separation bubble (LSB) will arise, which may act as an oscillator and amplifier. LSB's have been investigated in some detail in the 2D context [19], but the investigation of LSBs in the three dimensional (3D), less so. In this case, there is no longer a closed recirculation but a 3D open recirculation LSB in the span-wise direction.

A common conception based on experiments and computations concerning 2D steady flows is that backward facing steps (BFS) have a much more detrimental effect on boundary layer transition than forward facing steps (FFS). Duncan Jr. et al. [20] and Perraud et al. [21] suggest that the transition location is generally unaffected by small steps but then suddenly jumps to the step, implying there exists a critical step height. Generally, separation bubbles are helical flows which flow root to tip, contrary to the span-wise crossflow direction which flows tip to root [22]. Very recently, a critical step height has been characterized for swept flows over forward facing steps. Vidales et al. [23] experimentally and Tufts et al. [22] numerically studied the critical height for forward facing steps (FFS) and propose that if the core of the crossflow vortex height (y_c), for the clean case, is less than the height of the step (h) a destabilizing interaction takes place. This interaction is between the crossflow and helical downstream flow that is the separation bubble. The height of the core of the stationary crossflow can be determined by finding the CFI wavelength with the largest N-factor at the step location and then finding the maximum of the v -perturbation shape function. If $h > y_c$ the interaction is constructive, amplifies the stationary crossflow and the transition front moves towards the step. Vidales et al. [23] also note that an increase in the ratio of the step height to the boundary layer thickness at the step (h/δ_h) results in a larger reduction in critical N-factor for a fixed y_c/h ratio. Tufts et al. [22] confirmed the interaction of the separation bubble with a trial experiment. They artificially reduced the size of the separation bubble on top of the step but kept the step height the same. When doing this they found that the step produced similar disturbance profiles (amplitudes and shapes) to those for sub-critical step heights rather than the critical behavior expected for that step height.

Tufts et al. [22] also investigated the backward facing step (BFS) which exhibits a larger recirculation region than in the FFS case. They observed that increasing the step height results in a gradual movement of transition towards the step, rather than a quick jump, making it hard to characterize a critical height. They reasoned this is because of the presence of a traveling mode in the recirculation bubble which interacts with the stationary CFI.

Various FFS's and BFS's have also been investigated experimentally by Eppink [24, 25] for step heights ranging from 53 to 71% of the boundary layer. Eppink used the same criteria for predicting the FFS critical step height as Tufts et al. [22] and although results agreed well qualitatively, Tufts et al. predicted a critical step height 15% larger than Eppink found in experiments. Eppink reasoned that upstream of the step the primary incoming stationary crossflow vortices are lifted up significantly from the wall and do not directly impact the step. There are a second set of vortices, rotating in the opposite direction, which form underneath the primary set. Due to their rotation in the opposite direction, their interaction with the downstream helical flow should not be destabilizing. Eppink suggests the crossflow reversal region plays a crucial role in the transition process. Firstly this is because of the effect of the near wall vortex, caused by the crossflow reversal, on the growth of wall-normal perturbations near the wall. Secondly due to the strong streamline curvature induced from the positive crossflow component which causes the two vortices to eventually merge,

a consequence of which is a large stationary crossflow growth downstream.

This work assumes that crossflow instabilities, either stationary or traveling, have already been generated in the boundary-layer by an appropriate receptivity mechanism. The focus of the research is how these pre-existing disturbances are then further modified as they convect over sudden, localized, changes in surface geometry. The aim of this work is to explore and develop robust methods of analysis to enable quantification of how laminar flow may be degraded in the presence of three dimensional LSB's, induced by step-like features, and their interaction with crossflow disturbances. Motivation for the work arose from experiments undertaken by Saeed et al. [26] on a swept wing geometry (AERAST model, see Mughal and Ashworth [9]) where the movement of the laminar-turbulent transition front was observed with naphthalene. Single, infinitely long, 2D steps were created with Kapton tape at varying heights to mimic steps. A key finding was that beyond a critical height, waviness and jaggedness in the transition front was observed, and traveling crossflow instability signals were measured in the hot-wire data. Further increments in step heights moved the transition front forward towards the step. In recent more detailed experimental work Eppink et al. [27], find that the CFI destabilization that arises from BFS is not straightforward – the movement of the transition front is insensitive to BFS below a critical step height, and once the threshold is crossed then a rapid movement of the transition front to the step location is observed. These findings (together with findings of Saeed et al. [26]) suggest an altogether different mechanism in flow destabilization arises in BFS based swept wing boundary layer flows.

This paper outlines the methods that we use for modeling rapid changes in surface features, and their consequent effect on crossflow disturbances convecting over the *small-step* feature introduced on a swept wing geometry. The numerical modeling and instability analysis with PSE and LHNS, along with a new set of LHNS equations which incorporate the geometrical modeling of the steps is described in §III. An embedded mesh approach is used involving coupling an industrial finite volume RANS solver to obtain a global flow solution over the entire airfoil geometry, which then provides boundary and initial conditions for a more refined highly resolved solution within an embedded region. The highly resolved boundary-layer solutions over the micron-scaled step features is undertaken with direct numerical simulation (DNS). The embedded steady DNS solutions are obtained with a high order spectral/hp element solver, Nektar++. Some initial findings of the work are described in §III for FFS, BFS and bumps ranging from heights 24% to 53% of the boundary layer thickness. The steps are placed at 10% chord on a 40° infinite swept wing geometry. Some initial conclusions then follow in §IV.

II. Methods

A. Governing Equations

The two main methods applied in this work are the PSE and LHNS. Both are rapid methods for predicting transition location and involve decomposing the flow field into a base state and a perturbed field. The PSE model introduced by Herbert [5], are harmonic in time and assume a slowly varying wave in the stream-wise, x_1 , direction and a strictly periodic wave in the span-wise, x_3 , direction. They only retain terms which are up to $O(Re_\delta^{-1})$ and are reduced from an elliptic to a parabolic set of equations. The PSE are obtained by first decomposing the flow field into a steady base flow and unsteady perturbed flow,

$$\mathbf{q}(x_1, x_2, x_3, t) = \bar{\mathbf{q}}(x_1, x_2, x_3) + \epsilon \tilde{\mathbf{q}}(x_1, x_2, x_3, t), \quad \epsilon \ll 1. \quad (1)$$

The Navier-Stokes equations are then linearized and the perturbation field is decomposed further into a shape, $\hat{\mathbf{q}}$, and phase function, $\int \alpha(x) dx + \beta x_3 - \omega t$,

$$\tilde{\mathbf{q}}(x_1, x_2, x_3, t) = \hat{\mathbf{q}}(x_1, x_2) e^{i \int \alpha(x_1) dx_1 + \beta x_3 - \omega t} + c.c., \quad (2)$$

where the phase function absorbs rapid variations of $\hat{\mathbf{q}}$ though application of a normalization condition,

$$\frac{\int_0^\infty \tilde{u}^\dagger \frac{\partial \tilde{u}}{\partial x_1} + \tilde{v}^\dagger \frac{\partial \tilde{v}}{\partial x_1} + \tilde{w}^\dagger \frac{\partial \tilde{w}}{\partial x_1} dx_2}{\int_0^\infty \tilde{u}^\dagger \tilde{u} + \tilde{v}^\dagger \tilde{v} + \tilde{w}^\dagger \tilde{w} dx_2}. \quad (3)$$

The equation set can then be discretized and recast into the following matrix form,

$$(\mathcal{L}_0 + \mathcal{L}_1) \hat{\mathbf{q}} + \mathcal{L}_2 \frac{\partial \hat{\mathbf{q}}}{\partial x_1} + \frac{\partial \alpha}{\partial x_1} \mathcal{L}_3 \hat{\mathbf{q}} = 0. \quad (4)$$

Here, \mathcal{L}_0 , \mathcal{L}_1 , \mathcal{L}_2 and \mathcal{L}_3 are all matrix operators in x_2 . \mathcal{L}_0 corresponds to the linear parallel terms, \mathcal{L}_1 contains non-parallel terms of the basic state, \mathcal{L}_2 encompasses non-parallel perturbation terms and last, but not least, \mathcal{L}_3 corresponds to wave number terms.

The linear PSE equations can thus be solved very efficiently by a stream-wise marching parabolic procedure ([28] [29] [30]). Some weak remaining ellipticity in the PSE means that they are constrained by a minimum step size requirement for numerical stability. In order to obtain convergence, $\Delta x_1 \geq 1/\alpha_r$ must be satisfied; Δx_1 is the minimum stream-wise step size and α_r is the real part of the stream-wise wave number as alluded to by Li and Malik [8]. The computational domain applies a stretched grid in the wall-normal direction and a fourth order accurate finite central differencing discretization is applied within the domain. No-slip zero disturbance state is applied at the wall and perturbations are assumed to vanish in the far field.

The LHNS, although requiring slightly more computational time and resource than the PSE, provide much more information about the solution and are not limited by any step size restriction. They assume a periodicity in the span-wise direction through application of the following ansatz,

$$\tilde{\mathbf{q}}(x_1, x_2, x_3, t) = \hat{\mathbf{q}}(x_1, x_2)e^{i(\beta x_3 - \omega t)} + c.c.. \quad (5)$$

The linear harmonic Navier-Stokes form, comprises few assumptions, and are a fully elliptic set of equations which can be recast upon numerical discretization into a large matrix problem of unknown field state points, namely

$$\mathcal{L}\hat{\mathbf{q}} = \hat{\mathbf{r}}. \quad (6)$$

Here, \mathcal{L} , is a vector of the unknown perturbation field, $\hat{\mathbf{q}}$, and a forcing vector, $\hat{\mathbf{r}}$. The solution vector, $\hat{\mathbf{q}}$, is obtained directly by a Lower-Upper matrix LU decomposition method. The forcing vector, $\hat{\mathbf{r}}$, is composed of first order Taylor expansions which modify the wall boundary condition to generate the crossflow (CF) disturbance ahead of the step feature. The wall inhomogeneity may be either stationary (to generate zero frequency disturbances) or non-stationary to generate traveling CF disturbances, as denoted in Fig. 1.

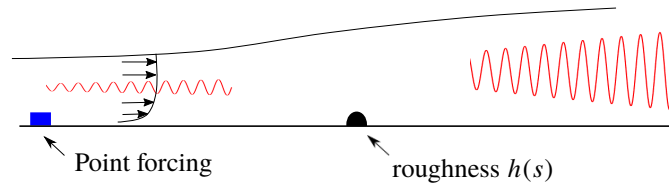


Fig. 1 Depiction of the computational domain showing generation of the instability (red) within a fully developed laminar boundary layer and how this instability is modified when convecting over the roughness.

The equations are discretized with a fourth order accurate central finite differencing scheme in the stream-wise direction and a spectral approach is applied in the surface normal direction. The inflow plane is situated sufficiently upstream of the actuation point such that perturbations can be considered negligible there. At the outflow boundary the PSE radiation condition is applied. Typically, 1800 points are used in the stream-wise direction and 51 Chebyshev polynomials in the wall-normal direction for the no-step cases. Further details may be found in [9] and [31]. To resolve disturbance evolution over the very rapid changes in the BFS and step induced boundary-layer flows as many as 10000 stream-wise and 90+ Chebyshev polynomials are subsequently utilized.

B. Incorporating the Roughness

We have discussed the generation of the perturbation via a small surface actuation, now we need to consider the relatively larger scale step feature and its incorporation into the modeling. It is important to note that for both PSE and LHNS codes, the solvers have visibility of the *roughness* or step through the base-flow profiles, but require an additional transformation to allow resolution of the step feature introduced. The original perturbed PSE [29] and LHNS [9] equations have been formulated based upon a body-fitted clean geometry coordinate system, without allowance for very rapid variations in surface topography such as those considered in this paper.

In order to incorporate large scale roughness, a non-orthogonal coordinate system must be introduced and a parameter assigned to the roughness profile, $h(x_1)$, which is dependent on the stream-wise body fitted coordinate, x_1 . The clean body fitted coordinate system (x_1, x_2, x_3) is transformed to the roughness incorporating coordinate system (s, Y, z) by

application of the following transformation,

$$s = x_1, \quad Y = x_2 - h(x_1), \quad z = x_3, \quad (7)$$

see Fig. 2 also. Since, upon substitution into the Navier-Stokes equations, the transformation is only introduced through the derivative terms, we can see that the roughness edges will cause the key difference between the original and transformed solutions, where dh/ds and d^2h/ds^2 hold non-zero values. The final transformed equation sets, which include the rapid geometrical step modeling, will from here on be referred to as the LHNSh and PSEh models.

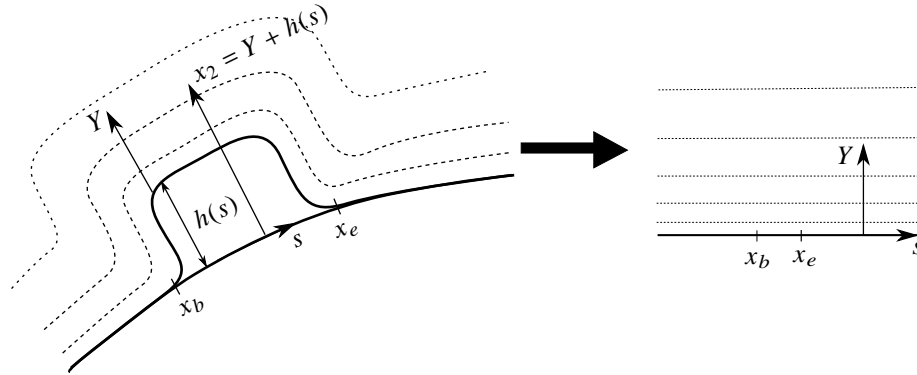


Fig. 2 Depiction of coordinate transformation to decompose the roughness incorporating geometry, (x_1, x_2, x_3) , to the body fitted clean surface, (s, Y, z) , plus a separate h component. Computational domain is depicted on the right.

C. Baseflow Generation and Step Configurations

The AERAST, 40° swept wing, geometry forms the basis of our investigations. The free stream velocity is 20 m/s and Reynolds number is 1×10^6 . The flow conditions and thus DNS computations are made to match as closely as possible to the experimental campaign of Saeed et al. [26]. Boundary-layer field states for four varying step heights are closely matched to the experiments performed. The experiments were only undertaken for localized steps created by placement and layering of non-varying tape strips along the span of the swept model, together with the periodic in span placement of distributed roughness circular elements (DREs) to generate crossflow disturbances ahead of the step. In the computational work reported here, we replicate the experimental scenario but furthermore, we explore the effects of forward facing step (FFS) and backward facing step (BFS) profiles too, on traveling and stationary CF disturbances – not investigated in the experimental campaign of Saeed et al. Each are evaluated at 10% chord with non-dimensional heights $412.5 \mu\text{m}$, $618.7 \mu\text{m}$, $825 \mu\text{m}$ and $893 \mu\text{m}$. The width of the bump is 3.75mm and heights, relative to the local boundary layer thickness, are denoted in table 1. Only the one bump width is considered to replicate the work of Saeed et al. [26]. Worner et al. [13] also suggest that the height of the roughness is much more detrimental to the laminar flow than the width, which plays quite a minor role.

	412.5	618.7	825	893
10% chord	24.43%	36.65%	48.86%	52.93%

Table 1 Roughness height as a percentage of boundary layer thickness of the clean (no step) geometry at each given location.

A civil transport wing would have a boundary layer near the leading edge of the order of millimeters, a wing chord on the order of meters and a span of tens of meters. Computationally modeling a roughness of the order of microns on a geometry of this scale is very demanding with a single computation. To overcome such scale difficulties, in this work a hybrid approach is being developed which combines the use of an industrial finite volume RANS solver to obtain the global flow regime with an embedded hp spectral element approach to more efficiently resolve the fine detail in the laminar boundary layer and roughness. In order to produce the roughness base flow computations, firstly the clean, full geometry, steady base flow is computed using RANS solutions of the industrial flow solver TAU [32]. An embedded

steady DNS solution is then computed using a high order, spectral/hp element solver; Nektar++ [33]. Inflow boundary conditions are extracted from the full TAU solution and high order pressure conditions are applied at the outflow to enable converged solutions on the severely truncated domain [34], see Fig. 3. Far field inflow boundaries are located 35% of a chord length above and below, and 40% of a chord length upstream, of the leading edge. The upper outflow planes are located at 70% chord, just before the flow begins to separate, and at 50% on the lower surface.

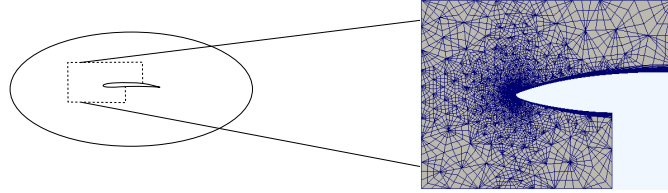


Fig. 3 Left shows the full TAU solution, right shows the embedded Nektar++ domain.

Nektar++ discretizes the domain with h , grid size, and/or p , polynomial order, refinement in order to solve the incompressible Navier-Stokes, for the base flows. A second order accurate implicit-explicit scheme is applied for the time integration and a stiffly stable splitting scheme is utilized to decouple the velocity and pressure fields. Fourier expansions are applied within the span-wise direction with periodic boundary conditions to complete the 2.5 dimensional domain. High order curve-linear meshes are created with computer-aided design (CAD) software and NekMesh which is included in the Nektar++ framework [33].

Convergence studies of h and p type refinement are conducted to ensure no mesh dependence. Typically a polynomial order seven was required, within the quadrilateral, near wall, layer and a lower order was sufficient within the external triangular elements. Usual roughness meshes contain 10,000 elements which are then expanded through the corresponding polynomial basis. Steady solutions are confirmed with an L^2 norm relative error of velocity fields across the entire domain such that,

$$\frac{c}{\bar{u}_\infty} \frac{\sum_{j=1}^N (\bar{\mathbf{q}}_t(j) - \bar{\mathbf{q}}_{t-1}(j))^2}{\sum_{j=1}^N (\bar{\mathbf{q}}_t(j))^2} \leq 10^{-5}. \quad (8)$$

D. Extracting Boundary Layer Profiles

Since the usual boundary layer solver tools fail to compute a valid solution for separated flows [17], a post processing routine has been constructed to extract profiles from the Nektar++ steady state converged roughness simulations. The DNS base flows are extracted and interpolated to the body fitted co-ordinate system for use in the subsequent stability codes. Spline interpolation is applied in the stream-wise and wall-normal directions to attain an equi-spaced, grid in the wall-normal direction, which is finer near the leading edge and grows downstream. A non-uniform stream-wise growing grid is applied to ensure a finer clustering of points near the leading edge and step feature. In the latter position, clustering is crucial to resolve the very rapid variation of the surface, as it merges from the step to the original step-free surface, in an almost near vertical *jump* in the surface field variation. Data is non-dimensionalized with the boundary layer edge values which are determined by finding the point where the stream-wise velocity is 99.99% of the inviscid stream-wise velocity, such that $\bar{u}_e = 99.99\% \bar{u}_{inviscid}$.

A boundary layer solver tool which solves the two dimensional boundary layer equations for swept wings, CoBLc [35], has been used in conjunction with the clean (step-free) case to confirm the validity of the post processing. CoBLc does not incorporate curvature terms, meaning some difference may be expected between the Nektar++ extracted profiles and CoBLc, see Fig. 4.

E. Nektar++ Linearized Navier-Stokes

Nektar++ is also used to compute the unsteady linearized incompressible Navier-Stokes solutions (Nektar++ LNS) for comparison with the more efficient PSE and LNS stability codes. Contrary to the harmonic formulation of the LHNS equations, which provide the long time asymptotic solution, Nektar++ LNS applies a time marching procedure. The domain and method of solving is set up similarly to that of the baseflow cases [33] however, a finer mesh is required for the Nektar++ LNS in order to obtain converged solutions. This resulted in using another embedded mesh consisting of only the upper surface geometry. The wall conditions are modified to provide suction / blowing across one Nektar++

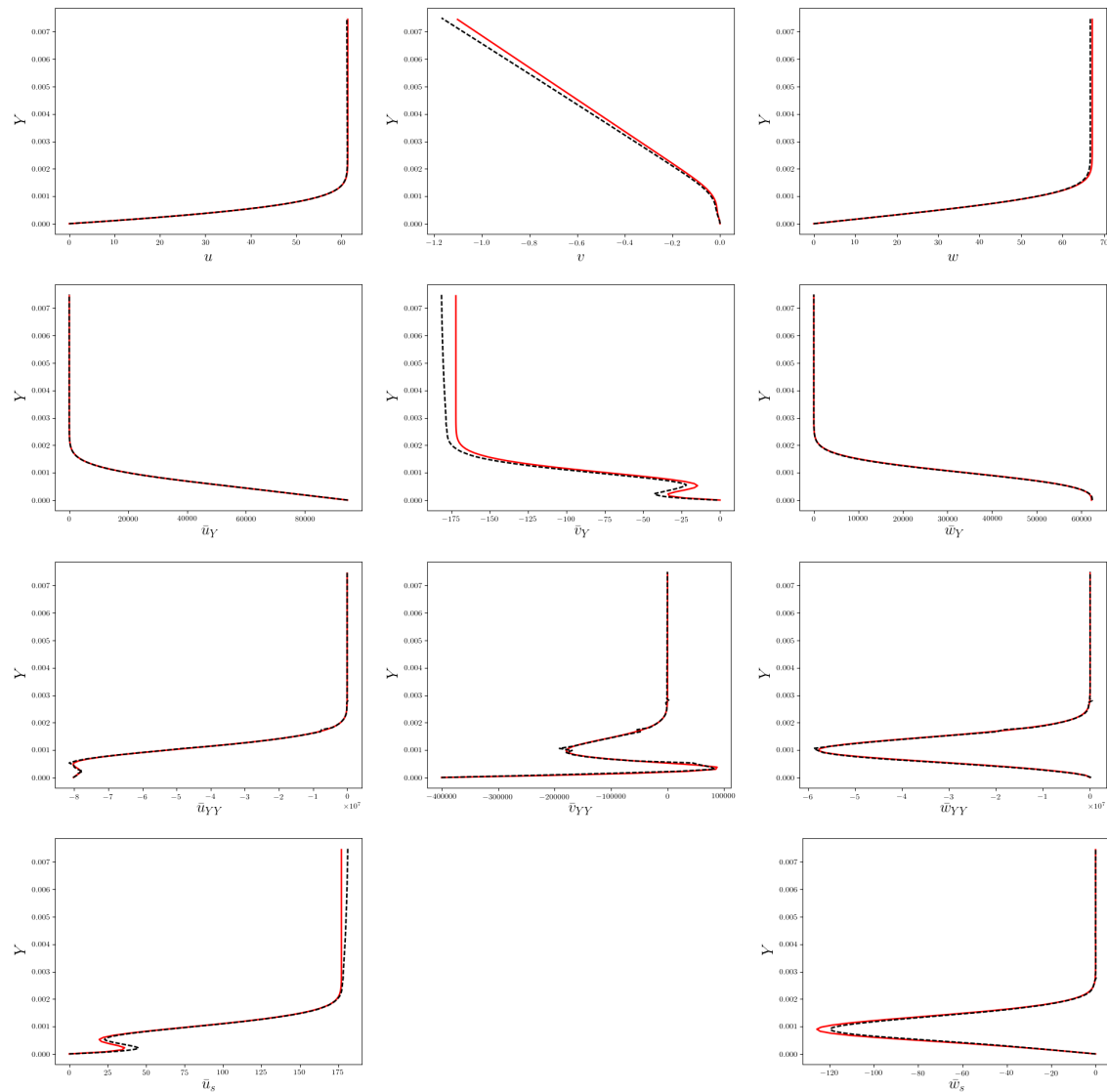


Fig. 4 Clean: Comparison with Nektar++ extracted base flow profiles and the boundary layer solver(CoBLc) generated profiles at 10% chord. All values are real physical quantities. Nektar++ solutions are represented with black, dashed, lines and CoBLc with red, solid, lines. Top row shows u , v and w , second and third rows shows first and second derivatives, respectively, in the normal direction with respect to u , v and w and the last row is the first derivative in the stream-wise direction with respect to u , v and w . There is no \bar{v}_s since this is not computed by CoBLc.

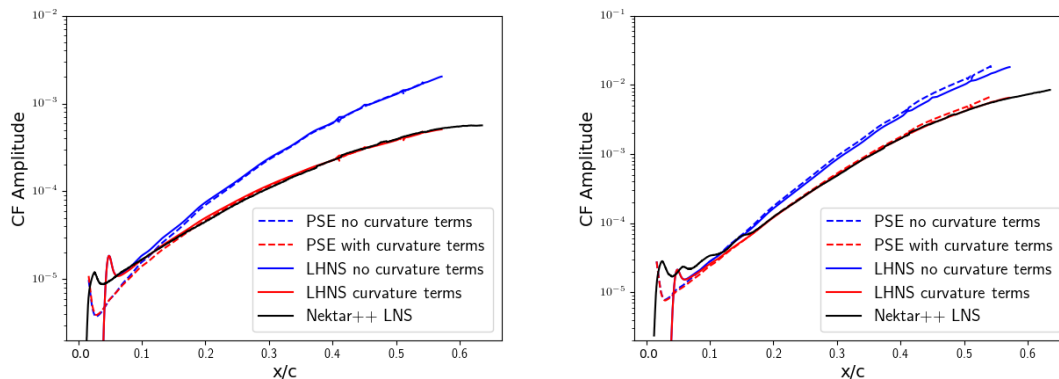


Fig. 5 Clean AERAST geometry LHS and Nektar++ LNS comparison. Left: Stationary CFI, $\beta = 500$. Right: Traveling CFI, $\beta = 440$, $\omega = 420$

surface element thickness to introduce the perturbation. The span-wise domain is configured such that it is the same length scale as the introduced CFI and periodic boundary conditions are then applied.

When running the PSE solver on the clean geometry and sweeping through the wave numbers, the most destabilizing stationary CFI is found to be $\beta = 500$ for the stationary case and $\beta = 440, \omega = 420$ for the traveling case. The amplitude growth predicted by the PSE and LHS codes have been compared with the Nektar++ LNS computation. Both PSE and LHS codes have been computed including and excluding curvature terms. CFI amplitude plots are given by normalizing the maximum of the stream-wise disturbance velocity with the boundary layer edge velocity at each stream-wise location. As expected, we see a stabilizing effect from the inclusion of the curvature terms which is in good agreement with the Nektar++ LNS solution, see Fig. 5. All analyses to follow will hence be computed with the inclusion of curvature. The PSE seems to be predicting the disturbance amplitudes very well in the absence of the roughness, and at the benefit of reduced computational cost (less than a second).

III. Results

Base flow profiles are computed with the AERAST geometry at a Mach number of 0.3 and a negative 4.5° incidence, in order to obtain agreement with the experimentally determined pressure gradient measurements of Saeed et al. [26]. Example steady base flows, derived from the DNS, for the largest roughness cases can be seen in Fig. 6. Lengths of separation bubbles with respect to the roughness height, $b_h = b_l/h$, (and width, $b_w = b_l/h_w$, in the localized bump case) are listed in table 2 for the varying roughness shapes. We can see that the conjugation of the FFS and BFS causes much more elongated bubbles for the down-stream reverse flow.

For the stability analysis, a range of CFI wave numbers and frequencies must be computed for each roughness case in order to find the most destabilizing CFI. A roughness of one height may trigger growth of one wavelength but not for another. This also applies to the different shape of roughness, meaning that a range of CFI's need to be scanned for each case. This is achieved rapidly by application of the PSE equations. Unfortunately, we will see the PSE and PSEh are unable to capture the presence of the roughness correctly. However, LHS and LHSsh codes are able to model the influence of the roughness in the majority of cases. The LHSsh formulation generally predicts greater amplitude CF disturbances.

A. Localised Bump

The composition of a FFS and BFS are placed 3.75mm apart to create the bump profile. All four heights of roughness have been computed with the PSE and PSEh codes for stationary and traveling CFI. N-factor growth curves are displayed in Fig. 7; the clean case has been added for reference. According to both codes there seems to be a stabilization as the bump height is increased, contrary to the literature, which could be due to a number of reasons. Firstly, many stream-wise station locations need to be neglected during the computation in order to attain a solution. This is due to the stream-wise derivative terms exhibiting very large gradient changes over the edges of the bump, where there are rapid variations in geometry. The roughness, although considered large scale in this paper, is still very small

shape	roughness height	forward b_w	forward b_h	backward b_w	backward b_h
bump	413	0.03	0.25	0.87	7.98
bump	618.7	0.09	0.56	1.74	10.57
bump	825	0.20	0.91	2.69	12.22
bump	893	0.25	1.04	3.06	12.83
FFS	413		0.05		
FFS	618.7		0.58		
FFS	825		0.97		
FFS	893		1.1		
BFS	413				6.56
BFS	618.7				7.59
BFS	825				8.19
BFS	893				8.35

Table 2 Bubble lengths with relation to the roughness height, b_h . For the bump case there are two separation regions, before (forward) and after (backward) the bump, which have been related to bump width, b_w , also.

meaning these neglected stations could be a result of satisfying the PSE step size restriction. As a consequence of ignoring some stations, this can mean no profiles are selected over the edges of the bump where the curvature of the roughness, dh/ds , holds a value. We can see this from bump heights 412.5 and 618.7 microns, which give exactly the same predictions for PSE and PSEh computations. We could also have an event where a station along one edge of the bump is taken, but not its corresponding other edge, resulting in a positive dh/ds term in one instance but its corresponding negative contribution not captured in the PSE computation. This could be the case for the higher bump profiles which show some slight differences between PSE and PSEh. The major drawback of the PSE is that it will fail to compute a valid solution if the instability wavelength is greater than, or of the same length as, the roughness width [7]. Here the wavelength of the CFI is around 6 mm and the bump 3.75 mm meaning the bump region is unfortunately too small to be captured by the PSE or PSEh. Sumariva and Hein [36] also came across these problems when trying to compute PSE solutions. PSE results from here-on will be omitted since they give much the same results.

LHNS and LHNSh computations for stationary and traveling CFI are shown in Fig. 8 for all bump heights. The instability is generated by a wall forcing placed just upstream of the clean neutral point (3% chord) and the bump is located at 10%. Both codes are generally consistent with the literature for stationary CFI, where increased step height triggers greater amplification of instability [22, 25, 37]. LHNSh predicts an even larger growth of instability for all bump heights larger than 618.7 microns, in comparison to the LHNS formulation. The 412.5 micron case gives a similar result to the clean case for both LHNS and LHNSh codes, showing the smallest bump height does not have any overall effect on the growth of the CFI; this is in agreement with observations in the experimental work of Saeed et al. [26]. According to the LHNSh code, the next step height, 618.7, also predicts no overall difference to the clean case, as the bump height increases further we begin to see an increased forward movement in transition. The LHNS code seems to predict more amplification of CFI for the 618.7 case than the 825 case, which seems very unlikely. This could possibly be due to having used the PSE to find the most unstable CFI wave numbers. Since the PSE is unable to resolve the roughness region, the most unstable wave number it finds may not, truly, be the most unstable wave number. Perhaps in this case, the PSE actually found a more unstable wave number for the 618.7 case than the 815. Given the differences between the two LHNS / LHNSh solutions we are led to conclude that the LHNS formulation neglects some crucial role of the perturbed u_s field locally at the bump geometry change. Looking at the traveling CFI curves, there is a similar trend to the results as for the stationary case but the growth is amplified ten times that of the stationary case. It is noticeable that the clean case is more amplified than the smaller bump heights (in the LHNSh codes), again we reason that this could be due to the use of the PSE to select the most unstable frequencies which are not, in fact, the truly most unstable wave number-frequency combinations. Contrary to the work of Saeed et al. [26], the LHNSh code predicts that the second highest bump height, 618.7, predicts no forward movement of transition.

A direct comparison of the two codes for the largest bump case can be seen in Fig. 9. Here we can see the LHNSh code predicts a greater amplification of CFI than LHNS for both stationary and traveling CFI. Evaluating all heights, it

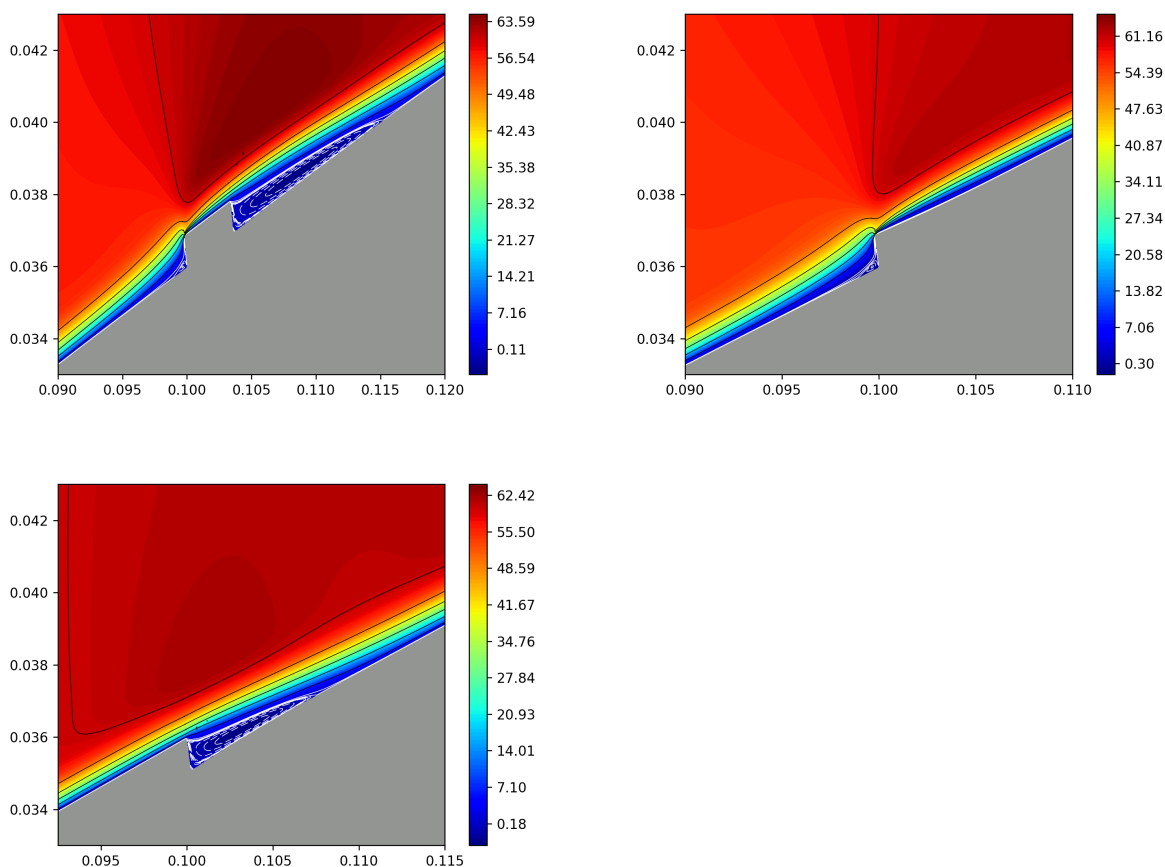


Fig. 6 Baseflow solutions at 10% chord, 893 microns for the bump (top left), FFS (top right) and BFS (bottom left). Contours show stream-wise velocity, black lines show the outer boundary layer and free-stream flow. White lines show flow within the inner boundary layer and dashed white lines denote separation bubbles.

would appear that if there was a critical bump height to cause transition, it must be located somewhere between 37% to 48% of the boundary layer thickness.

Contours of the stream-wise velocity perturbation for the largest bump case are depicted in Fig. 10 for stationary and traveling CFI. Again, each stream-wise location is normalized with the maximum stream-wise velocity at each point. The separation bubble is made visible by the dashed black lines and we see the disturbances structure convecting over the bump and recirculation zone. As in the previous figure, the traveling CFI is much more amplified than the stationary CF. Generally it seems that as the bump height increases, the CFIs which are most destabilized become longer in wavelength, this is consistent with Tufts et al. [22]. We can see the instability is modified by the bump corners and triggers a rapid increase in N-factor for the LHNS code. This characteristic is very similar to findings of Sumariva and Hein [36] who looked at a sharp cornered bump (but in context of 2D base flows). However when looking at the LHNSh code, although there still exists this origination from the upstream corner of the bump, the CFI seems to be more greatly amplified as it moves downstream of the bubble region, suggesting an interaction with the bubble, as has been indicated in other works [19, 22, 23].

We have compared the height of the clean crossflow vortex (CFV) with that of the height of the step. We thought that we might extrapolate the postulation from Tufts et al. [22] for when the step height of a FFS, h , is larger than that of the CFV height, y_c , there is a constructive interaction between the helical flow downstream of the FFS and the CFV. The height of the CFV varies with each wavelength of CFI introduced. This means the clean case needs to be evaluated for each of the corresponding most destabilizing wavelengths for the bump cases. When examining the perturbed velocity profiles, the height of the CFV is between 1463 microns (smallest bump: $\beta = 440$) to 1509 microns (largest bump:

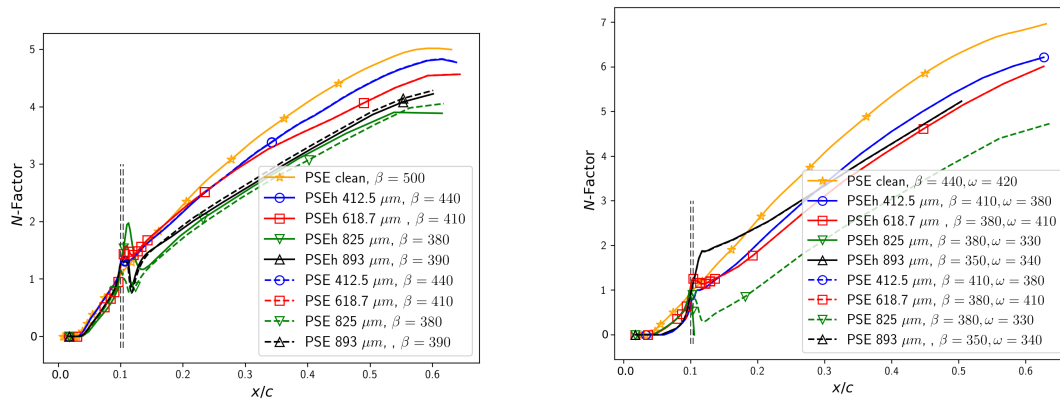


Fig. 7 Bump at 10% chord: PSE calculation (dashed lines) and PSEh (solid lines) comparison of N-factor growth of most unstable CFI for all roughness heights. Blue for 412.5 microns, red for 618.7, green for 825 and black for 893 microns. Left: Stationary CFI. Right: Traveling CFI

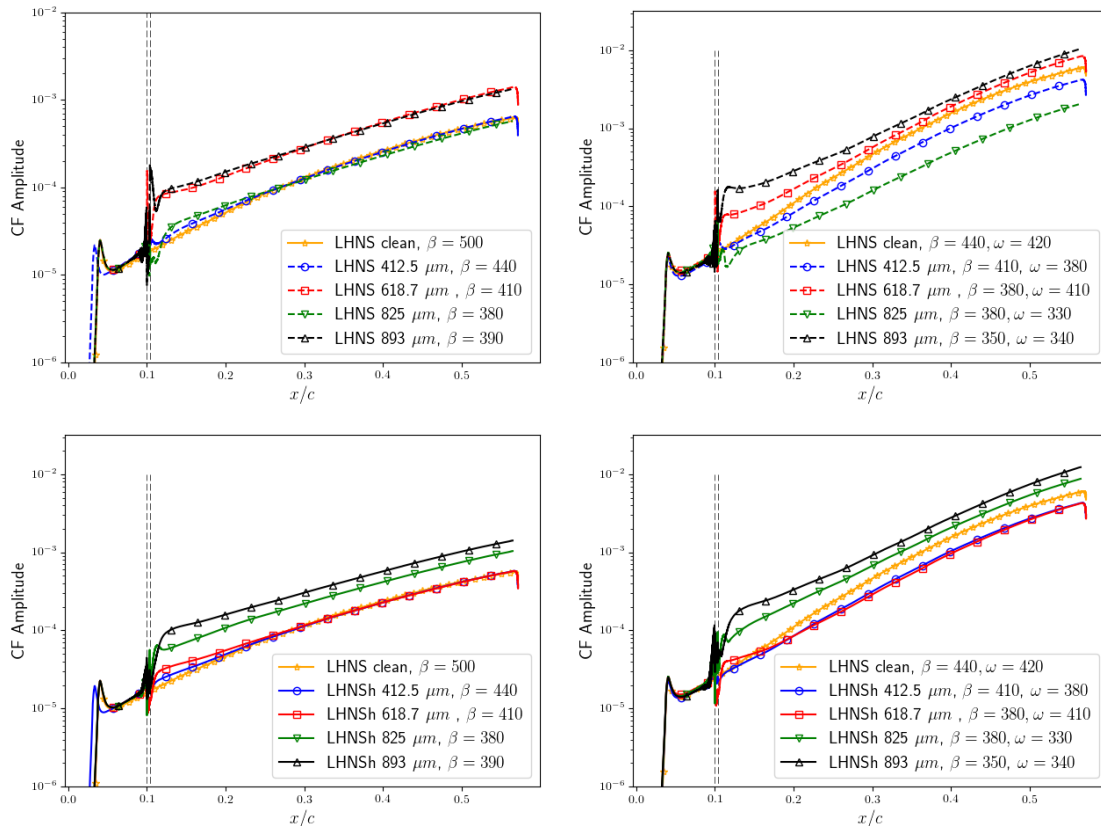


Fig. 8 Bump at 10% chord: Comparison of cross flow instability of all bump heights. Yellow points denote the clean geometry, blue circles for 412.5 microns, red squares for 618.7, green downward pointing triangles for 825 and black upward pointing triangles for 893 microns. Dashed vertical lines denote the width of the bump. Left: Stationary CFI. Right: Traveling CFI. Upper: LHNS calculation. Lower: LHNSh calculation

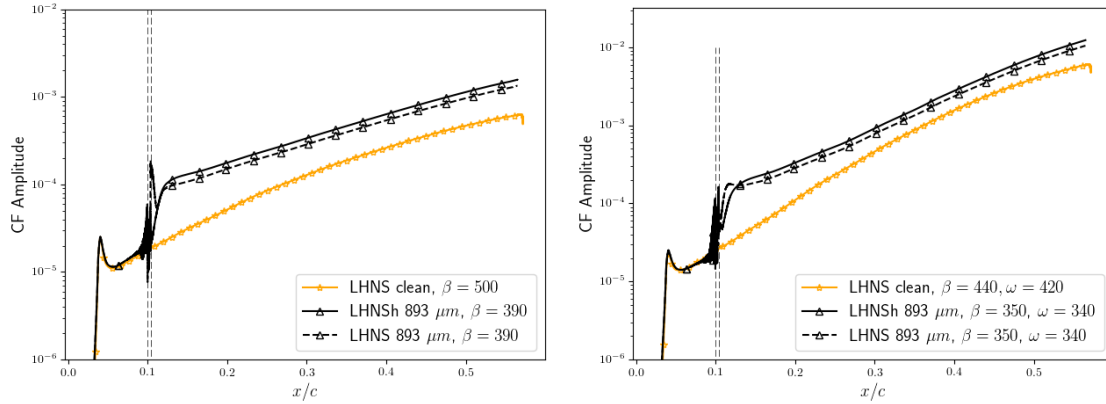


Fig. 9 Bump at 10% chord with height of 893 microns: LHNSh (solid lines) and LHNS (dashed lines) comparison of crossflow instability. Left: Stationary CFI. Right: Traveling CFI.

$\beta = 390$) for the stationary case, and 1417 microns (smallest bump: $\beta = 410, \omega = 380$) to 1462 microns (smallest bump: $\beta = 350, \omega = 340$) for the traveling case. All of these CFV heights are larger than any of the bump heights, meaning this reasoning is not appropriate for the bump configuration. In this instance, there is also no recirculation bubble on top of the bump for there to be destabilizing interaction with the CFI, there only exists one prior to the FFS component and after the BFS component. This suggests, that for the bump case, it could be one of these helical flows which the CFI is interacting with. Given the results in Fig. 10, it is likely to be the downstream helical flow. When examining these instability velocity profiles, we have noticed $\max(\sqrt{\hat{u}^2 + \hat{w}^2})$ seems to correlate with the bump height. The value of $\max(\sqrt{\hat{u}^2 + \hat{w}^2})$ ranges from 646 to 692 microns in height, which is just higher than the second bump height.

B. Forward Facing Step (FFS)

The FFS case has been simulated for all four step heights at 10% chord. Similarly for the bump case, the PSE fails to compute a reliable solution. Again, this is likely due to strong stream-wise gradients and the step feature being too short compared to the CFI wavelength, thereby violating the PSE formulation.

The LHNS and LHNSh codes both predict an increase in growth coinciding with increased step height, see Fig. 11. The most destabilized wave numbers still seem to be decreasing as FFS height increases, but at a much more gradual rate than the bump case. For the stationary CF case, the LHNS code predicts an amplification in growth of the smallest bump case, compared with the clean. This seems an unlikely prediction since for the bump case no difference in amplitudes arose between the LHNS/LHNSh models and the bump case has a BFS component which, from the literature, we know to be much more detrimental to the flow. This leads us to believe the LHNSh result is more reliable. The increase in growth for the 618 micron case seems reasonable since it is predicted by both codes. Again, comparing these heights to the postulation from Tufts et al. [22], we find that the CFV core height for each case is larger than all of the FFS heights. This is probably due to not having the second recirculation that Tufts et al. have in their cases. However, since we still see an amplification of CFI for the larger three FFS heights, there must be some other mechanism interacting with the stationary CFI. We can see the traveling CF is much more dangerous compared to the stationary CF case. Looking at the LHNS result, we would not expect 825 micron case to move the transition front further forward than the 893 micron case, again this merits the LHNSh code for seeming to give a more reliable result. The difference in amplitude predicted by both codes is highlighted for the largest step height in Fig. 12.

Contour plots of the stream-wise perturbation field for the largest step height are depicted in Fig. 13. Again, we can see that the immediate growth of perturbation seems to be triggered by the step corner, as can clearly be seen in the lower right image. Contrary to the bump case, there is no separation bubble present downstream of the step, however the corner does seem to trigger more rapid growth of CF disturbance. When examining \hat{u} perturbation profiles we find that at the step region there are two peaks which form in the perturbation profile, the larger of which is closer to the wall. As we move downstream these peaks tend to merge into one; Eppink [24] also observed this feature when examining FFS.

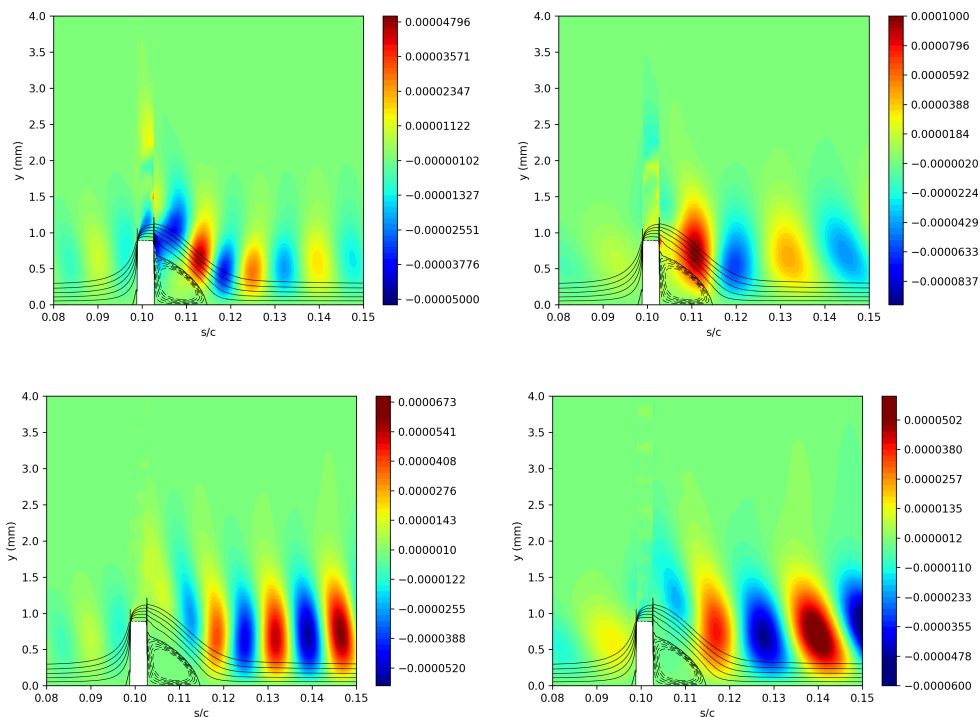


Fig. 10 Stream-wise perturbation field, $|\hat{u}|$, for 893 micron bump at 10% chord. Left: LHNS stationary case, $\beta = 500$. Right: LHNS traveling case, $\beta = 400$, $\omega = 550$. Upper: LHNS solver. Lower: LHNSh solver.

C. Backward Facing Step (BFS)

The BFS has proved much more difficult to compute reliable stability analyses. Unsurprisingly, the PSE and PSEh once again fail to capture the effect of the step. However, the PSE does seem to be selecting wave numbers reasonably well since the lower wave numbers become more amplified due to the thickening of the boundary layer [38]. The LHNS and LHNSh codes also struggle to produce a reliable solution. This is due, once again, to these strong stream-wise gradient changes and the way in which the base flow is interpolated onto the computation grid. Usually a cubic spline interpolation is applied in the stream-wise direction but this can cause spurious profiles in the region of the roughness. The spline interpolation has been replaced with linear interpolation within this region but it still seems these gradient changes are extremely large. This is perhaps to be expected since a BFS of half the height of a FFS may cause transition [37]. Contour plots are shown in Fig. 14 to highlight the differences between LHNS and LHNSh. Until this feature, i.e. the most correct procedure for interpolating very rapidly varying steady base flows profiles to the LNS defined grid is resolved – further work and analysis is required before one can make definitive statements on the effect of the BFS on the convecting CFs over the step.

IV. Conclusions

We have presented some very preliminary results of our work concerning the role of steps on swept wing flows, and how pre-existing stationary and traveling CF disturbances are modified by the step feature. Two new roughness incorporating codes, LHNSh and PSEh, are derived and tested on a swept wing with varying shapes and heights of step placed at 10% chord. One of which is a bump shape, identical to the experimental work of Saeed et al. [26]; FFS and BFS cases form part of the continuing investigations too. The three different step types are evaluated for 4 heights varying from 25% to 53% of the boundary layer thickness.

When applying the PSE / PSEh formulation to any of the roughness cases, the PSE is incapable of capturing the growth of the instability as it convects over the feature. This is due to the presence of strong stream-wise gradients and the minimum step size of the PSE being much larger than the resolution required for convergence over the roughness

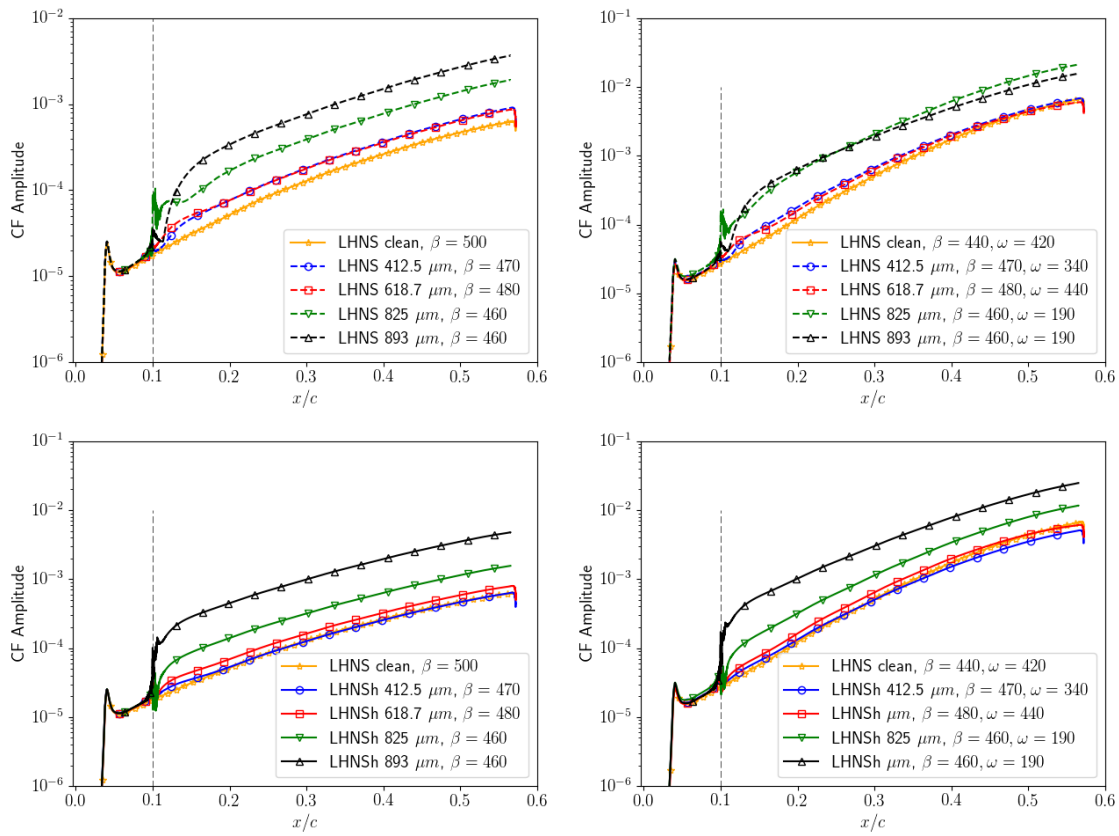


Fig. 11 FFS at 10% chord: Comparison of most destabilizing crossflow instability, though all bump heights. Red for 412.5 microns, blue for 618.7, green for 825 and black for 893 microns. Left: Stationary CFI. Right: Traveling CFI. Upper: LHNS calculation. Lower: LHNSh calculation.

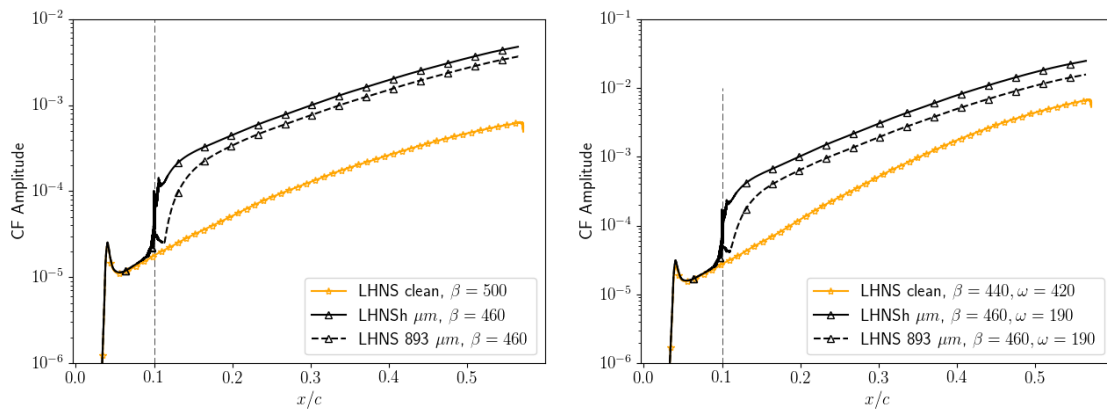


Fig. 12 FFS at 10% chord with height of 893 microns: LNSh (solid lines) and LNS(dashed lines) comparison of crossflow instability. Left: Stationary CFI. Right: Traveling CFI.

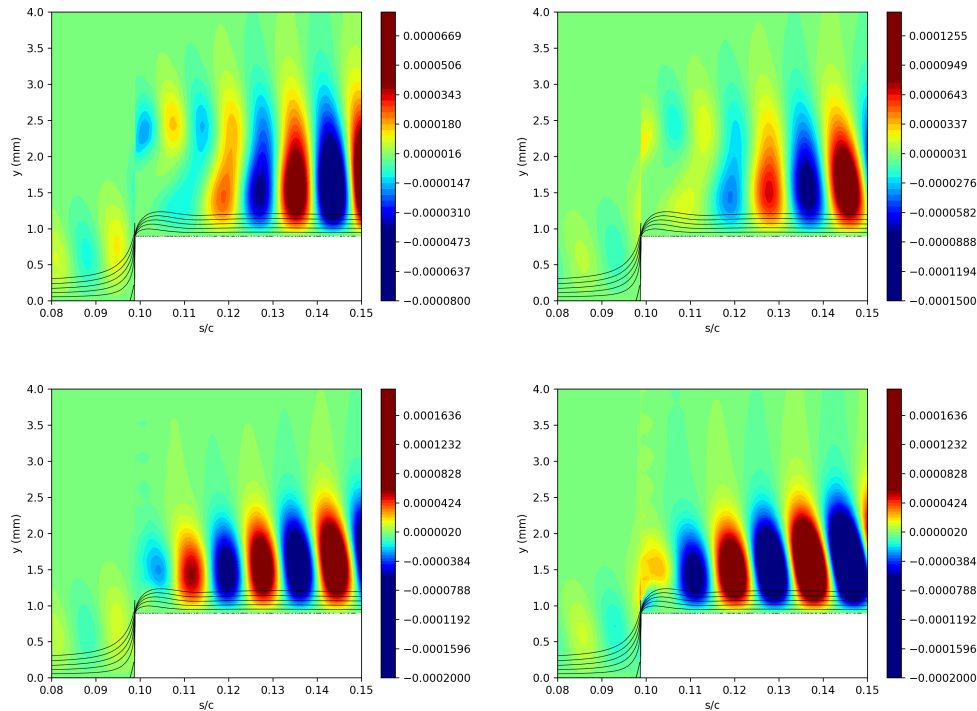


Fig. 13 Stream-wise perturbation field, $|\hat{u}|$, for 893 micron FFS at 10% chord. Left: LHNS stationary case, $\beta = 460$. Right: LHNS traveling case, $\beta = 460$, $\omega = 190$. Upper: LHNS solver. Lower: LHNSh solver.

region. The LHNS and LHNSh, on the other hand, do manage to capture the bump and FFS with these strong and very rapid stream-wise base flow variations. The LHNSh code generally predicts a greater increase in growth as the disturbance convects over the step location and downstream. It is clear that this feature should be included not just in the base flow terms, but also in the perturbed field model, if we wish to capture the growth of an instability within such severe stream-wise changes in the boundary layer state. As is consistent with literature, the traveling CFs seem to be much more detrimental to the flow than corresponding stationary CF.

We suspect that possibly, the criteria of Tufts et al. [22] can not be applied in these FFS cases, or extrapolated to the other step cases, due to the absence of a reverse flow region on top of the step. Tufts et al. indicate that reducing the size of the upper recirculation region decreases the impact of the FFS; the results in this paper (with the caveat of being very preliminary results) seem contrary to observations of Tufts et al. Vidales et al. [23] tend to agree with the method proposed by Tufts et al., however they do not mention if a separation bubble exists on top of their step configuration. We assume that one is present in order for them to have agreement. Since in our case there is no separation present, the geometrical shape itself must be playing a role. Perhaps ramping the surface up to the FFS height or creating more filleted corners could help to reduce the amplification of the disturbance.

The work presented here is on going to aid with characterizing the effect of surface roughness and steps on transition. Validation of these results with Nektar++ LNS is currently work in progress along with computations for the BFS and also evaluation of steps placed at 20% chord, also investigated in the experiments of Saeed et al. [26].

Acknowledgments

The authors acknowledge support from the Airbus Group Central Research Technology (CRT), EPSRC and Imperial College London Center for Doctoral Training in Fluid Dynamics Across Scales. Thanks are also given to Dr. Hui Xu, for sharing his expertise with generating Nektar++ base flow solutions with step features.

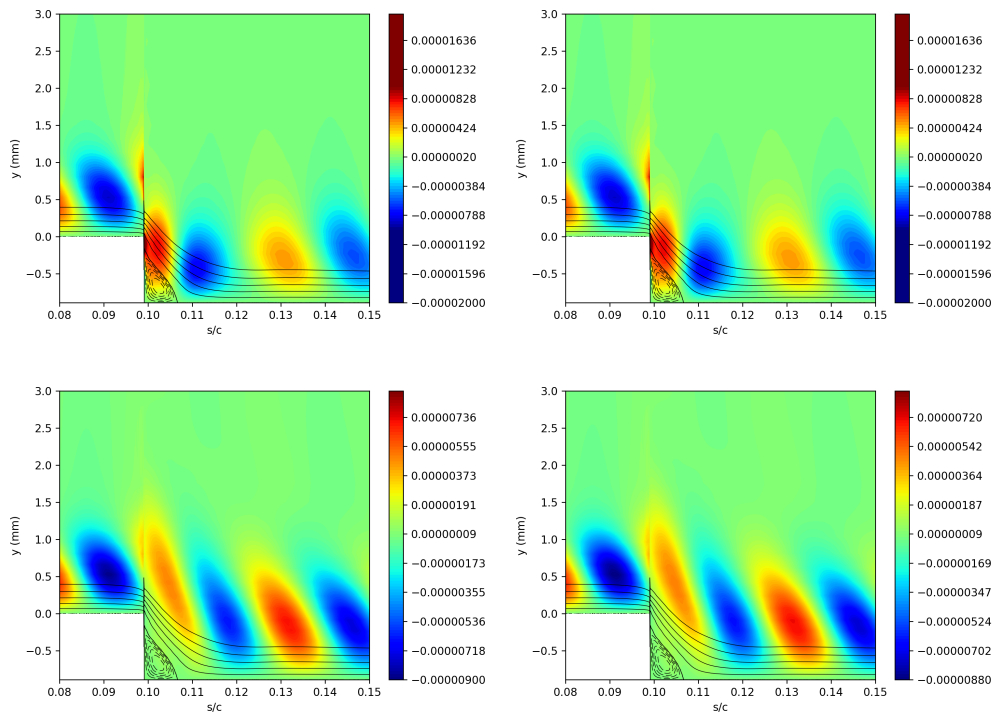


Fig. 14 Stream-wise perturbation field, $|\hat{u}|$, for 893 micron BFS at 10% chord. Left: LHNS stationary case, $\beta = 450$. Right: LHNS traveling case, $\beta = 450$, $\omega = 490$. Upper: LHNS solver. Lower: LHNSh solver.

References

- [1] Gubisch, M., "ANALYSIS: Why Airbus foresees laminar wings on next-gen aircraft," July 2018. URL <https://www.flightglobal.com/news/articles/analysis-why-airbus-foresees-laminar-wings-on-next-448911>
- [2] Beck, N., Landa, T., Seitz, A., Boermans, L., and Liu, R., Y. and Radespiel, "Drag Reduction by Laminar Flow Control," *Energies*, Vol. 11, No. 252, 2018.
- [3] Morkovin, M. V., Reshotko, E., and Herbert, T., "Transition in open flow systems—A reassessment," *Bul. Smrt. Phys. Soc.*, Vol. 1882, No. 39, 1994.
- [4] Van Ingen, J. L., "A suggested semi-empirical method for the calculation of the boundary layer transition region," Vth-74, Delft University of Technology, 1956.
- [5] Herbert, T., "Parabolized Stability Equations," *Ann. Rev. Fluid Mech.*, Vol. 29, 1997, pp. 245–283.
- [6] Bertolotti, F. P., "Linear and Nonlinear Stability of Boundary Layers with Streamwise Varying Properties," Ph.D. thesis, Ohio State University, 1991.
- [7] Wu, X., and Dong, M., "A local scattering theory for the effects of isolated roughness on boundary-layer instability and transition: transmission coefficient as an eigenvalue," *J. Fluid Mechanics*, Vol. 794, 2016, pp. 68–108.
- [8] Li, F., and Malik, M. R., "On the Nature of PSE Approximation," *Theoretical and Computational Fluid Dynamics*, Vol. 8, No. 4, 1996, pp. 253–273.
- [9] Mughal, S. M., and Ashworth, R., "Uncertainty Quantification Based Receptivity Modelling of Crossflow Instabilities Induced by Distributed Surface Roughness in Swept Wing Boundary Layers," *AIAA Paper 2013–3106*, 2013.
- [10] Mughal, S. M., *CoPSE/BL-MiPSecR User Manual*, Imperial College London, 2015.
- [11] Wang, Y., and Gaster, M., "Effect of surface steps on boundary layer transition," *Experiments in Fluids*, Vol. 39, No. 4, 2005, pp. 679–686.

- [12] Fong, K. D., Wang, X., and X, Z., “Numerical simulation of roughness effect on the stability of a hypersonic boundary layer,” *Computers and Fluids*, Vol. 96, 2014, pp. 350–367.
- [13] Worner, A., Rist, U., and Wagner, S., “Humps/Steps Influence on Stability Characteristics of Two-Dimensional Laminar Boundary Layer,” *AIAA J.*, Vol. 41, No. 2, 2003, pp. 192–197.
- [14] Park, D., and Park, S. O., “Linear and non-linear stability analysis of incompressible boundary layer over a two-dimensional hump,” *Computers and Fluids*, Vol. 73, 2013, pp. 80–96.
- [15] Rizzetta, D. P., and Visbal, M. R., “Numerical Simulation of Excrescence Generated Transition,” *AIAA J.*, Vol. 52, No. 2, 2014, pp. 385–397.
- [16] Costantini, M., Risius, S., and Klein, C., “Experimental investigation of the effect of forward-facing steps on boundary layer transition,” *Procedia IUTAM*, Vol. 14, 2015, pp. 152–162.
- [17] Thomas, C., Mughal, S., Roland, H., Ashworth, R., and Martinez-Cava, A., “The effect of gap deformations on the stability of TS wave disturbances,” *AIAA J.*, Vol. 56, No. 6, 2017, pp. 2157–2165.
- [18] Ashworth, R., Lawson, S., Lowry, R., Martinez-Cava, A., Mughal, S., Roland, H., and Thomas, C., “Numerical and experimental study of the tolerance of natural laminar flow on a wing to TS destabilisation at the leading edge /wing-box junction,” *Royal Aeronautical Society Applied Aerodynamics Conference, 19-21 July 2016, Bristol (UK)*, Royal Aeronautical Society, 2016.
- [19] Rodríguez, D., Gennaro, E. M., and Juniper, M. P., “The two classes of primary modal instability in laminar separation bubbles,” *J. Fluid Mechanics*, Vol. 737, 2013.
- [20] Duncan Jr., G. T., Crawford, B. K., Tufts, M. W., Saric, W. S., and Reed, H. L., “Effects of Step Excrescences on a Swept Wing in a Low-Disturbance Wind Tunnel,” *AIAA Paper 2014–0910*, 2014.
- [21] Perraud, J., Arnal, D., Séraudie, A., and Tran, D., “Laminar-Turbulent Transition on Aerodynamic Surfaces with Imperfections,” *Int. J. Engineering Systems Modelling and Simulation*, Vol. 6, No. 3/4, 2004, pp. 162–170.
- [22] Tufts, M. W., Reed, H. L., K., C. B., Duncan Jr., G. T., and Saric, W. S., “Computational Investigation of Step Excrescence Sensitivity in a Swept-Wing Boundary Layer,” *J. of Aircraft*, Vol. 54, No. 2, 2017, pp. 602–626.
- [23] Vidales, A. F. R., Kotsonis, M., Antunes, A., and Cosin, R., “Effect of Two-Dimensional Surface Irregularities on Swept Wing Transition: Forward Facing Steps,” *AIAA Paper 2018–3075*, 2018.
- [24] Eppink, J., “Stereo Particle Image Velocimetry Measurements of Transition Downstream of a Forward-Facing Step in a Swept-Wing Boundary Layer,” *AIAA Paper 2017–0306*, 2017.
- [25] Eppink, J., “The Effect of Forward-Facing Steps on Stationary Crossflow Instability Growth and Breakdown,” *AIAA Paper 2018–0817*, 2018.
- [26] Saeed, T. I., Mughal, S. M., and Morrison, J. F., “The Interaction of a Swept-Wing Boundary Layer with Surface Excrescences,” *AIAA Paper 2016–2065*, 2016.
- [27] Eppink, J. L., Richard W. Wlezien, R. W., King, R. A., and Choudhari, M., “Influence of a Backward-Facing Step on Swept-Wing Boundary-Layer Transition,” *AIAA J.*, Vol. 57, No. 1, 2019, pp. 267–278.
- [28] Chang, C.-L., Malik, M. R., Erlebacher, G., and Hussaini, M. Y., “Linear and nonlinear PSE for compressible boundary layers,” Tech. rep., September 1993.
- [29] Mughal, M., “Active Control of Wave Instabilities in Three-Dimensional Compressible Flows,” *Theoretical and Computational Fluid Dynamics*, Vol. 12, No. 4, 1998, pp. 195–217. doi:10.1007/s001620050106, URL <https://doi.org/10.1007/s001620050106>.
- [30] Zhao, D., “INSTABILITY AND RECEPTIVITY OF BOUNDARY LAYERS ON CONCAVE SURFACES AND SWEPT WINGS,” Ph.D. thesis, Imperial College London, 2011.
- [31] Raposo, H., Mughal, S., and Ashworth, R., “Acoustic receptivity and transition modeling of Tollmien-Schlichting disturbances induced by distributed surface roughness,” *Physics of Fluids*, Vol. 30, No. 1070-6631, 2018.
- [32] DLR, *TAU-Technical documentation of the DLR TAU-code*, Institute of Aerodynamics and Flow Technology, Braunschweig, 2011th ed., 2011.

- [33] Cantwell, C., Moxey, D., Comerford, A., Bolis, A., Rocco, G., Mengaldo, G., Grazia, D. D., Yakovlev, S., Lombard, J.-E., Ekelschot, D., Jordi, B., Xu, H., Mohamied, Y., Eskilsson, C., Nelson, B., Vos, P., Biotto, C., Kirby, R., and Sherwin, S., "Nektar++: An open-source spectral/hp element framework," *Computer Physics Communications*, Vol. 192, 2015, pp. 205–219. doi:10.1016/j.cpc.2015.02.008.
- [34] Dong, S., Karniadakis, G., and Chrysosostomidis, C., "A Robust and Accurate Outflow Boundary Condition for Incompressible Flow Simulations on Severely-Truncated Unbounded Domains," *Journal of Computational Physics*, Vol. 216, 2013, pp. 83–105.
- [35] Thomas, C., Mughal, S., Gipon, M., Ashworth, R., and Martinez-Cava, A., "Stability of an Infinite Swept Wing Boundary Layer with Surface Waviness," *AIAA J.*, Vol. 54, No. 10, 2016.
- [36] Sumariva, A. F., J., and Hein, S., "Adaptive Harmonic Linearized Navier-Stokes equations used for boundary-layer instability analysis in the presence of large streamwise gradients," *AIAA Paper 2018–1548*, 2018.
- [37] Perraud, J., Arnal, D., and Kuehn, W., "Laminar-turbulent transition prediction in the presence of surface imperfections," *Int. J. Eng. Systems Modelling and Simulation*, 2014.
- [38] Perraud, J., "Effects of steps and gaps on 2D and 3D transition," *European Congress on Computational Methods in Applied Sciences and Engineering. ECCOMAS 2000*, 2000, pp. 11–14.



Global Stability Analysis of a Boundary Layer with Surface Indentations

Thibaut Appel*

*Airbus Central Research and Technology, Bristol BS34 7PA, United Kingdom
Imperial College London, South Kensington Campus, London SW7 2AZ, United Kingdom*

Shahid Mughal†

Imperial College London, South Kensington Campus, London SW7 2AZ, United Kingdom

Richard Ashworth‡

Airbus Central Research and Technology, Bristol BS34 7PA, United Kingdom

In the quest for laminar flow control on aircraft wings, quantifying the impact of structural deformation on laminar-turbulent transition remains a challenge. The purpose of this work is to numerically investigate the stability of two-dimensional incompressible boundary layers developing on a flat-plate geometry with indented surfaces of different depths. These surface indentations generate laminar separation bubbles, known to have strong destabilizing effects on Tollmien-Schlichting disturbances. The parallel efficiency of the developed computational tool based on state-of-the-art numerical libraries allows rapid parametric studies within the usually expensive global stability analysis framework. Using an incompressible linearized Navier-Stokes formulation, we use the perfectly matched layer method to absorb waves at the inflow and outflow boundaries. Forced receptivity analysis is performed in order to investigate the effect of the indentation region on the convecting Tollmien-Schlichting waves. Furthermore, the likelihood of global temporal mechanisms arising is investigated through BiGlobal stability analysis. The deepest surface indentation, which features a peak-reversed flow velocity of 9 % in the laminar separation bubble, leads to significant levels of Tollmien-Schlichting amplification. It is also characterized by two temporally unstable modes, namely a dominant, localized stationary mode as well as a traveling Kelvin-Helmholtz mode.

I. Nomenclature

English symbols

A	=	discretized linear stability operator
B	=	discretized mass operator
F	=	non-dimensional frequency
f	=	frequency
H	=	roughness shape
h	=	indentation depth
i	=	imaginary unit
L	=	length scale
Ma	=	Mach number
\mathbf{n}	=	outward normal vector
n	=	number of grid points
p	=	pressure
\mathbf{q}	=	flow variables vector
q	=	finite-difference order
R_c	=	target reflection coefficient for PML

*Ph.D. Student, Virtual Product Engineering, email: thibaut.appel@airbus.com

†Lecturer, Department of Mathematics, email: s.mughal@imperial.ac.uk

‡Modeling and Simulation Scientist, Virtual Product Engineering, email: richard.ashworth@airbus.com

Re = Reynolds number
 r = radial coordinate
 s = stretching metric for PML
 t = time coordinate
 U = velocity scale
 \mathbf{u} = velocity field vector (u, v, w)
 \mathbf{x} = spatial coordinates vector (x, y, z)

Greek symbols

α = streamwise wavenumber
 β = spanwise wavenumber
 Γ = control volume boundary
 γ = grid clustering parameter
 δ = boundary layer thickness
 ε = infinitesimal quantity
 ζ = complex frequency shift for PML
 η = deformed wall-normal coordinate
 θ = transformed eigenvalue for shift-and-invert
 κ = grid compression factor for PML
 λ = indentation width
 ν = kinematic viscosity
 ρ = density
 σ = damping profile for PML
 τ = shift eigenvalue for shift-and-invert
 Ψ = discretized forcing vector
 ψ = forcing vector
 Ω = control volume
 ω = angular frequency

Subscripts

i = imaginary part
 r = real part
 w = wall quantity
 ∞ = free-stream quantity

Superscripts

$*$ = dimensional quantity
 $-$ = base variable
 \sim = perturbation variable
 \wedge = shape function or amplitude
 \sim = stretched coordinate for PML

II. Introduction

DURING these pivotal times of climate change awareness, the transportation industry is facing public pressure over action for curbing CO₂ emissions. The success of the "flygskam" ("flying shame") movement in Sweden [1] and the current debate on ending the kerosene tax exemption for airlines might resonate with aeronautical industry stakeholders and increase their efforts to develop fuel-saving technologies. Understanding and controlling the laminar-turbulent transition of boundary layers is in line with these greener objectives. In the particular context of aircraft wings, the main benefit of maximizing the extent of laminar flow past the leading edge is that turbulence significantly increases friction drag and hence fuel consumption. The total drag of an aircraft would be reduced by approximately 16% if laminar flow

were maintained on 40% of its surfaces including wings, nacelles as well as horizontal and vertical stabilizers [2].

The multifaceted transition process relies on an idealized succession of scenarios [3]. It is initiated by the receptivity process, which describes how environmental disturbances impose their signature within a boundary layer and excite fluctuations. In a low-amplitude disturbance environment, the linear growth of instabilities is followed by non-linear mode interactions, secondary instabilities and finally by the breakdown into a turbulent state. However, this path is certainly not unique; should the initial disturbance amplitude be sufficiently large, the breakdown to turbulence may occur due to strongly amplifying mechanisms directly following the receptivity stage, bypassing the other stages. Numerous bypass transition processes were linked to a transient growth phenomenon [4], referring to initially small disturbances undergoing an algebraic growth before exponential decay.

In flat-plate subsonic flows, the dominant instability modes are the Tollmien-Schlichting (TS) disturbances, arising from a viscous instability. In practice, the manner in which TS disturbances are generated in atmospheric flight is assumed to be due to acoustic noise, turbulence and/or vorticity fields interacting with surface roughness, leading to receptivity. Experimental observations demonstrate that transition is heavily dependent on the environmental characteristics, which can also be influenced by three-dimensionality and free-stream conditions. Receptivity modeling in stability analysis is a key requirement for accurate transition prediction, since it establishes the initial magnitude of the fluctuations within a boundary layer which essentially dictates the possible path of its transition to turbulence. Above a certain amplitude threshold, non-linear effects are amplified, interaction between higher-order harmonics plays a significant role and leads to rapid transition to turbulence [5]. Thus, receptivity modeling is intrinsically linked to understanding where, how and what type of non-linear processes set in and dictate the transition path.

On top of complex instability mechanisms emerging in cruise flight conditions, qualitatively and quantitatively assessing how surface imperfections, or roughness elements, influence the stages of laminar-turbulent transition remains a hurdle. On wings, examples include damage due to scratches, hail dents as well as residuals of grease and insects. Natural excrescences formed by junctions between detachable leading edge and wing box components as well as more three-dimensional features such as rivet heads are also thought of having a non-negligible impact on transition. Such surface irregularities generally act as receptivity sites and lead to three-dimensional modifications to the basic flow state, which then impact upon disturbance convection and evolution.

Localized surface irregularities can induce a strong adverse pressure gradient in the streamwise direction and separate the boundary layer from the surface on which it is developing. This creates a separation or recirculation bubble if the flow reattaches further downstream. Although such a laminar separation bubble (LSB) might be stable due to limited energy exchange with the outer flow, it has been found [6, 7] that a boundary layer flow in the presence of a LSB is first globally unstable due to a stationary or low-frequency three-dimensional mode. Barkley et al. [7] highlighted how the critical absolute instability of a two-dimensional flow with a backward-facing step was localized in the LSB. Similar observations were noted in the case of a flow over a bump [8]. Applying direct and adjoint analysis, Marquet et al. [9] described two instability mechanisms, namely lift-up and convective non-normalities, in a recirculation bubble behind a smooth backward-facing step. Xu et al. [10] devised geometrical parameter correlations for the stabilization or destabilization of TS waves in the presence of smooth forward facing steps. The topology of LSBs was also analyzed to describe the instability characteristics of the global mode [11]. Marquet et al. [12] compared the strength of resonator dynamics and amplifier dynamics in a low-Reynolds-number recirculation bubble. Additionally, the existence of two global linear mechanisms was highlighted [13], unveiling a centrifugal instability leading to a steady three-dimensionalization of the LSB as well as oscillatory behavior dependent upon regions of absolute inflectional instability. A criterion for absolute instability was given in terms of the peak reversed-flow velocity in the LSB. A threshold as low as 7 % of peak reversed flow was found by Rodríguez and Theofilis [11] for two-dimensional LSBs. Later, Rodríguez et al. [13] stated that the two-dimensional absolute instability is inactive below 12 %, a higher value than the three-dimensional instability threshold of 7 %.

Given the multitude of laminar-turbulent transition road maps in nature, different approaches to model laminar-turbulent transition mechanisms have been developed. Standard methodologies ranging from local Orr-Sommerfeld (OS) theory, non-local linear and non-linear Parabolized Stability Equations (PSE) are mature and have been extensively used, with fine agreement with experiments. In recent work, Thomas et al. [14] found good agreement when comparing results based on the full Linearized Navier-Stokes (LNS) equations with results from the lower-order PSE form in their investigation of flow destabilization due to LSBs arising on two-dimensional wavy airfoils. Due to strong base flow gradients in the vicinity of LSBs, it is known that at some stage, alternative mechanisms take over in the turbulence tripping process. Abrupt transition due to bypass mechanisms may become prominent; presently, the changeover from convective-type breakdown to bypass processes is an area of significant uncertainty. The development of efficient numerical techniques, which allow such analyses to be undertaken, is currently not as advanced relative to techniques

devised for treating adequately convective instabilities and at a cheap computational cost. Global stability analysis holds potential for yielding more complex, localized two-and-a-half dimensional or three-dimensional instability modes distinct from those determined with PSE-type analyses.

Recently, Xu et al. [15] computed incompressible boundary layer flows convecting over localized three-dimensional surface indentations, where LSBs arose in the confined area of the indentation. Their presence was found to lead to rapid TS destabilization and thus tripping the laminar flow to turbulence, even at low Reynolds numbers. They studied how a preexisting two-dimensional TS disturbance is transformed to a three-dimensional form as it convects through the three-dimensional separation bubble. The LSBs were found to have a significant impact on the advected disturbances, in that the TS destabilization was linked to the inflectional instability of the separated shear layer. As an extension to Xu et al. studies, the main objective of the present work is to investigate the existence of unstable, global temporal eigenmodes related to the two-dimensional LSBs with BiGlobal analysis. Different indentation depths, and thus the impact of different separation bubble intensities, are examined to assess the potential existence of global modes. The other issue examined, with forced receptivity analysis, is the effect of naturally distributed two-dimensional surface forcing on preexisting TS disturbances as they convect through the LSBs.

The rest of this paper is organized as follows. Section III presents the mathematical formulation of the global stability analysis approach together with an absorbing boundary condition treatment via the perfectly matched layer framework. The numerical process used in the parallel computational tool that has been developed is presented in section IV. Results of temporal BiGlobal analysis and forced receptivity analysis are presented in section V. We conclude by highlighting the main findings of this study.

III. Mathematical Formulation

A. Governing equations for linear stability theory

As a means to study the modal evolution of disturbances in incompressible boundary-layer flows, the framework of Linear Stability Theory (LST) is used. In the Cartesian coordinates considered, $\mathbf{q} = (p, u, v, w)^T$ is defined as a compact representation of the instantaneous flow quantities where p is the pressure, u the streamwise velocity, v the wall-normal velocity and w the spanwise velocity. One can decompose the instantaneous quantities into a steady-state part and an infinitesimal part such that, for $\varepsilon \ll 1$,

$$\mathbf{q}(\mathbf{x}, t) = \bar{\mathbf{q}}(\mathbf{x}) + \varepsilon \tilde{\mathbf{q}}(\mathbf{x}, t) \quad (1)$$

The infinitesimal perturbations $\varepsilon \tilde{\mathbf{q}}$ are superimposed on a steady-state equilibrium $\bar{\mathbf{q}}$ called the base flow, which is laminar and has finite-amplitude in a domain $\Omega \subset \mathbb{R}^2$. Its boundary is denoted $\Gamma = \partial\Omega$. Introducing the decomposition of Eq. (1) in the non-dimensional Navier-Stokes equations, linearizing around the base flow and retaining the first-order perturbation terms $O(\varepsilon)$ yields the Linearized Navier-Stokes (LNS) equations, which read

$$\begin{aligned} \Delta \bar{p} + \nabla \cdot ((\bar{\mathbf{u}} \cdot \nabla) \bar{\mathbf{u}}) + \nabla \cdot ((\bar{\mathbf{u}} \cdot \nabla) \bar{\mathbf{u}}) &= 0 & (\mathbf{x}, t) \in \Omega \times \mathbb{R}^+ & \quad (2a) \\ \frac{\partial \tilde{\mathbf{u}}}{\partial t} + (\bar{\mathbf{u}} \cdot \nabla) \tilde{\mathbf{u}} + (\tilde{\mathbf{u}} \cdot \nabla) \bar{\mathbf{u}} + \nabla \bar{p} - \frac{1}{Re} \Delta \tilde{\mathbf{u}} &= \mathbf{0} & (\mathbf{x}, t) \in \Omega \times \mathbb{R}^+ & \quad (2b) \\ \tilde{\mathbf{u}} &= \boldsymbol{\psi} & (\mathbf{x}, t) \in \Gamma \times \mathbb{R}^+ & \quad (2c) \end{aligned}$$

where $\boldsymbol{\psi}$ is a forcing term applied on the boundary. The LNS Eqs. (2) are rendered dimensionless with a length scale L and a velocity scale chosen as the free-stream velocity U_∞ . The Reynolds number $Re = U_\infty L / \nu_\infty$ quantifies the ratio of inertial effects to viscous effects, where ν_∞ is the free-stream kinematic viscosity. Moreover, the pressure is non-dimensionalized by $\rho_\infty U_\infty^2$ and the time coordinate by L / U_∞ . Unless specified with units, all the introduced quantities in the rest of the paper are non-dimensionalized with these scales.

Note that the Linearized Pressure Poisson Equation (LPPE) formulation of the LNS equations is used, where a Poisson equation for the pressure, shown in Eq. (2a) substitutes for the traditionally used continuity equation $\nabla \cdot \tilde{\mathbf{u}} = 0$. Such a formulation was notably suggested by Johnston and Liu [16] and further discussed by Shirokoff and Rosales [17] for the full non-linear Navier-Stokes equations. In the standard "continuity-momentum", or primitive formulation of the Navier-Stokes equations, the pressure plays the role of a Lagrange multiplier and does not appear itself but solely through its gradient. When spatially discretizing this formulation on a collocated grid with centered finite differences, this lack of information leads to a non-physical pressure field formed of sawtooth patterns satisfying the Navier-Stokes equations, called "checkerboard instability".

In contrast, the LPPE formulation circumvents the checkerboard instability with additional information introduced for the pressure. Using a descriptor state-space model approach, Dellar and Jones [18] demonstrated the well-posedness of the formulation when the equations are discretized on a collocated grid. However, they commented that there is no guarantee that the LPPE formulation is entirely dynamically equivalent to the LNS equations formulated in primitive variables when spatially discretized. Therefore, special care is advised when investigating global stability analysis problems with the LPPE-LNS equations as, for instance, spurious eigenvalues may arise. Besides, to be mathematically equivalent to the primitive formulation, appropriate boundary conditions must be chosen to enforce $\forall(\mathbf{x}, t) \in \Gamma \times \mathbb{R}^+, \nabla \cdot \tilde{\mathbf{u}} = 0$, especially for the pressure at a no-slip boundary. Rempfer [19] explained that "*it is illegal to write down the momentum equation taken at the boundary and derive a pressure boundary condition from it by simply projecting the result on the wall-normal coordinate.*" The choice of boundary conditions for the pressure is mentioned in section V. To the best of our knowledge, it may be the first time that the full LPPE formulation has been used in global stability analysis for the interior of the domain Ω as Theofilis [20] used the LPPE solely as a boundary condition for the pressure at the wall, with a primitive LNS formulation in the interior.

B. Receptivity and BiGlobal analyses

For a steady base flow $\bar{\mathbf{q}}$, the separability between space and time coordinates allows the introduction of a Fourier decomposition in time, and the linear stability analysis is carried out seeking solutions to Eqs. (2) under a wave-like form,

$$\tilde{\mathbf{q}}(x, y, z, t) = \hat{\mathbf{q}}(x, y)e^{i\beta z - i\omega t} + \text{c.c.} \quad (3)$$

In the above, ω is the angular frequency and $\hat{\mathbf{q}}$ the shape function. The parameter β can be physically interpreted as a spanwise wavenumber related to a periodicity wavelength $L_z = 2\pi/\beta$. Furthermore, the abbreviation "c.c." means that the complex conjugate of the perturbation is added, as the latter remains a real quantity. The assumption of inhomogeneity in the streamwise and wall-normal directions coupled with periodicity in the spanwise spatial direction is an approach adapted to analyze streamwise geometry deformation effects on the base flow. The base flow solely depends on the streamwise and wall-normal coordinates, $\bar{\mathbf{u}}(\mathbf{x}, y)$ and $\bar{u}_z = 0$.

In the case where the receptivity of the flow to external forcing is analyzed, both ω and β are prescribed real quantities. In this work, the response of the flow to disturbances generated by a small-scale, time-fluctuating surface element located at the wall is examined, with its effect being modeled in the forcing term ψ . The assumption of infinitesimal perturbations in Eq. (1) allows the problem to be governed by the LNS Eqs. (2), coupled with boundary conditions for the velocity at the wall derived with a Taylor expansion treatment. The roughness shape $\varepsilon H(x, z, t)$ models the time-periodic wall-forcing and is given by the Fourier representation $H(x, z, t) = \hat{H}(x)e^{i\beta z - i\omega t}$. The components of the wall-forcing vector ψ read

$$\hat{u}_w(x) = -\hat{H}(x) \frac{\partial \bar{u}}{\partial y}(x, 0) \quad (4a)$$

$$\hat{v}_w(x) = -(\hat{H}(x) + i\omega) \frac{\partial \bar{v}}{\partial y}(x, 0) \quad (4b)$$

$$\hat{w}_w(x) = -\hat{H}(x) \frac{\partial \bar{w}}{\partial y}(x, 0) \quad (4c)$$

In another framework where, following the terminology introduced by Theofilis [21], we perform streamwise temporal BiGlobal analysis, there is no forcing term ψ to the boundary value problem presented in Eqs. (2) and the angular frequency ω becomes an unknown complex eigenvalue, whereas β remains a real, prescribed spanwise wavenumber. The complex eigenvalue ω represents the asymptotic, long-time limit behavior of the investigated flow perturbations in that the existence of one eigenvalue with a positive imaginary part (temporal growth rate) is a sufficient condition for a globally unstable flow. The latter will preferentially amplify the state with the most positive eigenvalue in time. Its real part ω_r represents the frequency of the perturbation. The corresponding eigenfunction, $\hat{\mathbf{q}}(x, y)$ describes its spatial shape.

C. The perfectly matched layer method

The choice of appropriate boundary conditions for the inflow and outflow regions in the context of global stability analysis remains cumbersome and has been discussed in literature, notably by Groot et al. [22]. Ideally, the perturbation field should be allowed to enter or exit the domain seamlessly, without physical or numerical reflection. Each flow

perturbation variable should satisfy the local dispersion relation at these boundaries. Typical boundary conditions include zero Dirichlet, extrapolation, Robin, a boundary condition based on Gaster transformation [23], a PSE-type ansatz or a 1D-LST-type ansatz. These will either not appropriately close the system of Partial Differential Equations (PDE) formed by the Eqs. (2) from a mathematical point of view, or have a limited domain of validity in the wavenumber space. This leads to spurious eigenvalues arising in the spectra of eigenvalue problems, to a restriction of the modeled physics and potentially to a contamination of the solution near the boundaries. Therefore, proper care is advised when employing them.

In an effort to alleviate this issue, a generic boundary treatment that models an unbounded domain and prevents reflections of spurious waves into its interior without resorting to empirical parameters has been adopted. The approach is the Perfectly Matched Layer (PML) method, introduced in a seminal paper by Berenger [24] for electromagnetics. This technique was extended to the linearized Euler and linearized Navier-Stokes equations by Hu et al. [25] and tested on various flow configurations. The underlying idea behind the technique is to surround the physical domain with a layer of grid points in which the same system as in Eqs. (2) is solved, but with an added dissipation term in order to absorb energy and thereby prevent reflections off the computational boundaries. This is achieved with a coordinate transformation that can be seen as an analytic continuation of the LNS equations into a complex contour, where propagating waves are gradually substituted by exponentially decaying waves within the PML. For example, consider a streamwise propagating wave $e^{i\alpha x - i\omega t}$ in the positive direction, with $\alpha \in \mathbb{R}$, $\alpha > 0$. If the following coordinate transformation is applied

$$\tilde{x} = x + \frac{i}{\omega} \int_x \sigma_x(s) ds \quad (5)$$

The wave ansatz with the stretched coordinate is then transformed to an evanescent wave

$$e^{i\alpha\tilde{x} - i\omega t} = \exp\left(-\frac{\alpha}{\omega} \int_x \sigma_x(s) ds\right) e^{i\alpha x - i\omega t} \quad (6)$$

which decays further downstream in any section of the domain where the damping profile σ_x is strictly positive. The principle of adding a lossy layer at the outflow of the physical domain becomes obvious. It should be noted that the same absorption benefit is obtained with a PML added at the inflow, since the upstream propagating waves $\alpha < 0$ would also decay in such a region in the $-x$ direction. Figure 1 provides a schematic overview of the method with absorbing layers present at the inflow, at the outflow as well as in the free-stream region of the computational domain.

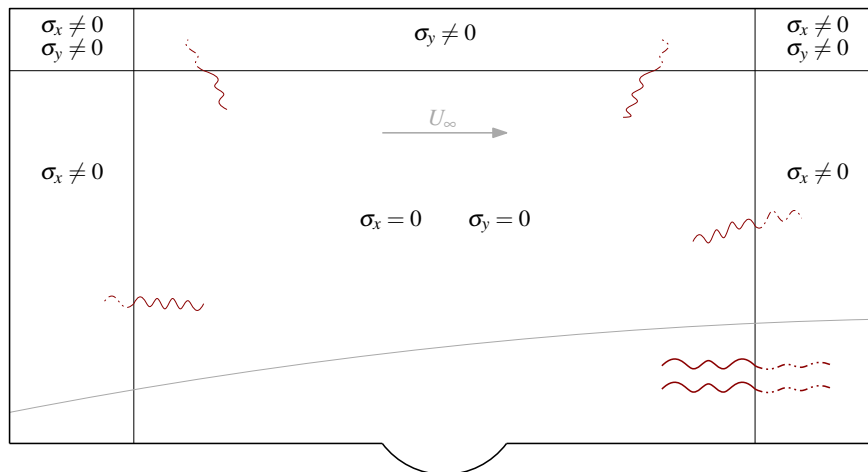


Fig. 1 Schematic representation of the PML method, with lossy layers in the streamwise and wall-normal directions.

As the name implies, the absorption should be "perfect" for the continuous problem and, in theory, should yield a zero reflection coefficient for all angles of incidence and frequencies at the interface between the physical domain and the lossy layer. After discretization of the governing equations, reflections unavoidably arise, but with a negligible amplitude. From a practical point of view, implementing the PML coordinate stretching for the formulation based on

the LNS Eqs. (2) is equivalent to changing the first order spatial derivatives to

$$\frac{\partial}{\partial \tilde{x}} = \frac{1}{1 - \frac{\sigma_x}{i\omega}} \frac{\partial}{\partial x} = \frac{1}{s_x} \frac{\partial}{\partial x} \quad (7)$$

The second order derivatives are obtained in the same manner using the chain rule. The subscript "x" does not mean a partial derivative but rather specifies the spatial direction where the PML extends. Devised in the frequency domain, the method is well adapted to suit the time-harmonic LNS approach followed here. It is also easily extended to two dimensions, where contributions from the different layers are simply summed at the corners. However, in this work the absorption treatment is mainly needed in the streamwise direction. The implemented PML formulation for the current analysis is based on the contribution from Komatitsch and Martin [26]. It is an extension devised to enhance the absorbing capability for grazing incident waves, the latter of which are spuriously reflected with the classical discrete PML methods. This formulation consists of a more general coordinate stretching s_x than in Eq. (7) with the introduction of new real variables such that

$$s_x = \kappa_x - \frac{\sigma_x}{i\omega + \zeta_x} \quad (8)$$

where $\sigma_x \geq 0$ is defined such that $\sigma_x > 0$ in the PML and $\sigma_x = 0$ in the physical domain. $\kappa_x \geq 1$ is a grid compression (or stretching) function. It further increases the wave damping since an additional factor $e^{-\kappa_x \alpha_i}$ is introduced inside the lossy layer. The complex frequency shift, $\zeta_x \geq 0$ introduces a shifting of the poles and contributes to mitigating the issue of absorbing waves impinging on the interface at grazing incidence. These functions defining the coordinate transformation must be sufficiently smooth to minimize numerical artifacts. Following Komatitsch and Martin [26], the damping profile is defined as a polynomial law

$$\sigma_x = \sigma_{\max} \left(\frac{x}{L_{\text{PML}}} \right)^2 \quad (9)$$

where L_{PML} is the width of the layer. The grid compression function is similarly written and reads

$$\kappa_x = 1 + (\kappa_{\max} - 1) \left(\frac{x}{L_{\text{PML}}} \right)^2 \quad (10)$$

The only literature contribution in which global stability analysis is performed with the aforementioned, simple stretching given by Eq. (7) is Merle [27], who applied the PML to study the analysis of laminar compressible flow over a bump and over an open cavity. Ran et al. [28] did not employ the PML method per se, but incorporated sponge layers implemented with a source term in the LNS equations and studied their influence on the temporal spectrum of a developing Blasius boundary layer profile. Although there is no contribution directly involving the use of the more sophisticated stretching of Eq. (8) with the LNS equations, Martin and Couder-Castaneda [29] applied the method for an evanescent treatment at the outflow boundary for a supersonic flow in a diffuser with non-linear Navier-Stokes equations. This yields sufficient foundation for the application of the method in the formulation involved in this work, which marks the first application of the PML method based on (8) with incompressible LNS equations and global stability analysis.

IV. Numerical Approach

A. Base flow computations

The three-dimensional base flows were computed by Xu et al. [15] by means of Direct Numerical Simulation (DNS) using a spectral/hp element discretization within the Nektar++ package, which supports h (grid size) refinement and p (polynomial order) refinement [30]. The full non-linear Navier-Stokes equations were solved with a stiffly stable splitting scheme which decouples the velocity and pressure fields. Time integration was achieved by a second-order accurate implicit-explicit (IMEX) scheme. The spectral element method was applied with a hybrid mesh, quadrilaterals and triangles, with 5425 elements and a 5th-degree polynomial expansion imposed in the streamwise direction. 4876 elements form the mesh in the wall-normal direction. A Fourier expansion with 180 modes was performed in the spanwise direction. The localized surface deformation is defined, in the streamwise direction, as

$$\eta(r) = \begin{cases} -\frac{h}{2} \left(\cos \left(\frac{2\pi r}{\lambda} \right) + 1 \right), & r \leq \lambda/2 \\ 0, & r > \lambda/2 \end{cases} \quad (11)$$

in which the radial coordinate $r = \sqrt{(x - x_c)^2}$ measures the distance to the indentation center position x_c . A convergence study by p -type refinement was performed to ensure mesh independence. Spanwise Fourier modes independence was also reached and steady solutions were obtained by time-marching the equations until an appropriate steady-state convergence criterion was met.

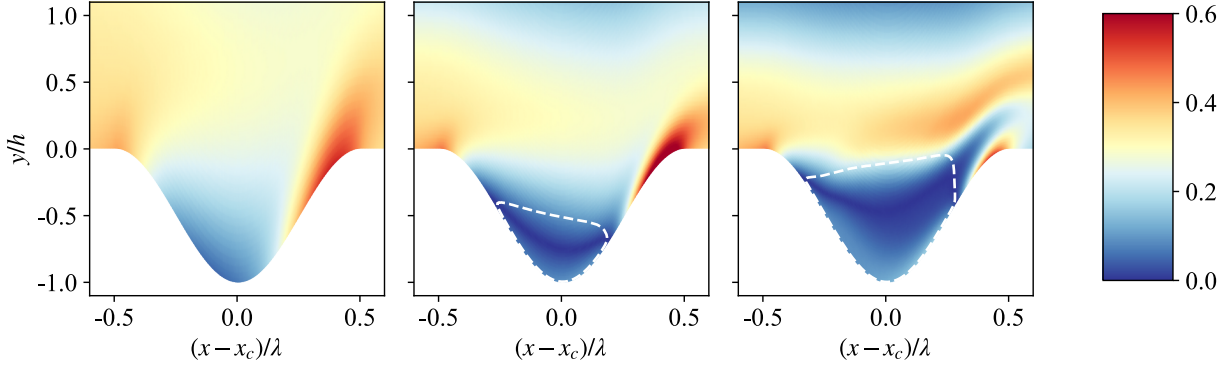


Fig. 2 Contours of non-dimensional vorticity $|\nabla \times \bar{u}|$ of the base flows. Left: $h = 0.81$ mm. Middle: $h = 1.62$ mm. Right: $h = 2.17$ mm. The white dashed line indicates the limit of the reversed streamwise velocity region.

Across the whole computational domain, the L_2 -norm relative error of the computed velocity fields was less than 10^{-6} . Figure 2 depicts the two-dimensional base flows for three different indentation depths, extracted along the streamwise symmetric plane of the three-dimensional indentations. The flows can be considered as incompressible since the Mach number satisfies $Ma = 0.05 \ll 0.3$. Moreover, the free-stream unit Reynolds number is $Re = 1.2 \times 10^6$ with a reference free-stream velocity $U_\infty = 18 \text{ m s}^{-1}$. The indentation width is $\lambda = 81$ mm. Base flows for different indentation depths were computed, namely $h = 0.81$ mm, $h = 1.62$ mm and $h = 2.17$ mm. The intensity of the LSB appears to grow with increasing depth and increasing peak reversed-flow velocity, the latter expressed as percentages. The cases respectively correspond to $\lambda/h = 100$ (0%), $\lambda/h = 50$ (3%) and $\lambda/h = 37.3$ (9%). For further details, the reader is referred to Xu et al. [15].

B. Receptivity and BiGlobal computations

The computational procedure is presented in what follows. After the discretization of the LNS Eqs. (2) on Ω , it is necessary to solve, for a receptivity-type problem a linear system

$$\mathbf{A}\hat{q} = \Psi \quad (12)$$

For a temporal BiGlobal approach, a Generalized Eigenvalue Problem (GEVP) must be solved, which has the form of

$$\mathbf{A}\hat{q} = \omega \mathbf{B}\hat{q} \quad (13)$$

where \mathbf{A} , \mathbf{B} are matrix operators discretizing the governing equations and Ψ is the vector incorporating the discretized wall-forcing components. All incorporate the boundary conditions. The discretization is performed with the FD- q method, developed by Hermanns and Hernández [31]. It is a stable, high-order finite-difference method based on a non-uniform grid that minimizes the Lagrange interpolation error, in order to alleviate the well-known Runge phenomenon and its spurious oscillations near the domain boundaries. The method can be seen as an intermediate between a "classic" finite-difference method and Chebyshev spectral collocation. Compact finite-difference stencils lead to non-negligible memory consumption and computation time gains while a near spectral-like accuracy is reached.

The base flow \bar{q} is interpolated on a regular grid using high-order B-splines. The surface deformation embodied by the indentation geometry is enclosed in the Jacobian of the mapping from the physical domain to the computational domain. In addition, we use a bi-quadratic mapping [32] that divides the wall-normal domain into three regions with an equal number of points to optimize the grid distribution in the near-wall region and hence appropriately capture the TS or global mode structures. In the streamwise direction, the grid is clustered around the maximum depth location of the

indentations with an interior contraction [33] coupled with the function $\tan(\gamma\pi x)/\tan(\gamma\pi)$, where γ controls the level of grid clustering.

The computational tool that has been developed relies on state-of-the-art numerical libraries in order to exploit both parallel efficiency and robustness. The formation of matrix operators \mathbf{A} , \mathbf{B} as well as of the right-hand-side vector Ψ is performed in parallel with the suite of data structures and routines PETSc [34]. The linear system formulated in Eq. (12) is solved with the sparse, multifrontal solver MUMPS [35] based on LU-factorization.

The parallel library SLEPc [36] is used to solve the GEVP of Eq. (13) with a Krylov-Schur method. It belongs to the class of Krylov subspace methods and allows computation of a portion of interest in the eigenvalue spectrum. The original problem is projected to a subspace of a significantly smaller dimension, whose associated eigenpairs are the best approximations to the original eigenvalue problem. Due to the absence of a time derivative in the LPPE shown in Eq. (2a) and the enforcement of some boundary conditions, the mass matrix \mathbf{B} is singular. Hence, a spectral transformation such as the shift-and-invert approach must be employed to solve the GEVP. In general, the convergence of the Krylov-Schur algorithm is optimal for eigenvalues lying at the spectrum extremities, and it is harder to extract eigenvalues located further into the interior. However, the regions of interest for linear stability problems of the kind considered here are typically located next to the origin. Using a shift-and-invert transformation bears the advantage of enhancing convergence of the eigenpairs in the vicinity of an interior target, or shift τ . The original GEVP is transformed into

$$(\mathbf{A} - \tau\mathbf{B})^{-1}\mathbf{B}\hat{\mathbf{q}} = \theta\mathbf{B}\hat{\mathbf{q}} \quad (14)$$

The eigenvector $\hat{\mathbf{q}}$ remains unmodified, while the relation between the original eigenvalue ω and the transformed eigenvalue θ is

$$\theta = 1/(\omega - \tau) \quad (15)$$

The algorithm is parallel and the required matrix inversion in the shift-and-invert operator included in Eq. (14) is also performed in parallel, by means of LU-factorization with MUMPS. The downside of the shift-and-invert approach is the constraint of manually prescribing shift values in the complex plane. Finally, a balancing technique is applied on the shift-and-invert operator in an attempt to curb round-off errors and maintain the accuracy of the computed eigenpairs to the requested level.

V. Results

For the computations performed in this work, a total of $n_x = 1500$ grid points were used in the streamwise direction and $n_y = 100$ in the wall-normal direction. The chosen length scale L is the corresponding zero pressure gradient Blasius boundary layer thickness $\delta_h = 0.735$ mm at x_c . The computational domain extends from $Re_\delta = 600$ to $Re_\delta = 1149$ in the streamwise direction, that is over a distance of roughly 10λ . Furthermore, the far-field boundary, where the perturbation field is assumed to vanish, is set sufficiently far away from the wall at $y = 150\delta_h$ in an attempt to reduce any influence of the domain truncation on the solution in the interior of the domain. Following Johnston and Liu [16], a Neumann boundary condition is imposed at the wall for the pressure

$$\frac{\partial \hat{p}}{\partial \mathbf{n}} + \frac{1}{Re} (\nabla \times \nabla \times \hat{\mathbf{u}}) \cdot \mathbf{n} = 0 \quad (16)$$

A FD-6 discretization is employed in the streamwise direction while high accuracy is targeted in the wall-normal direction with a FD-12 method. The streamwise grid is clustered near the indentation area with $\gamma = 0.4$.

With this set of parameters, the time spent on setting up and solving a two-dimensional, forced receptivity problem is 1 minute and 10 seconds. For a temporal BiGlobal problem, depending on the spectrum distribution and on the shift value, the computation time is between 10 minutes and 1 hour. In total, 16 MPI (Message Passing Interface) processes were used on a cluster node of 2 sockets and 8 cores per socket, with Intel® Xeon® E5-2680 (Sandy Bridge) CPU architecture.

A. Receptivity to wall-forcing

In the first instance, we investigate the destabilization of TS waves generated by a small-scale, time-periodic surface element placed ahead of the surface indentation. The surface actuation generates a purely two-dimensional perturbation field, that is $\beta = 0$. A Gaussian profile defines the streamwise surface deformation shape of the forcing as shown in Fig. 3. Its maximum is located 450 mm after the nominal leading edge, or roughly 1.97λ before the streamwise station marking the beginning of the indentation. Its maximum deformation off the base surface is 0.25 mm which is negligible

relative to the indentation depth h . The full width at half-maximum is $\lambda/18 = 4.5$ mm. Naturally, within the scope of the linearized framework, the deformation maximum height prescribed in the analysis is in fact irrelevant since any amplitude result can be simply scaled to fit.

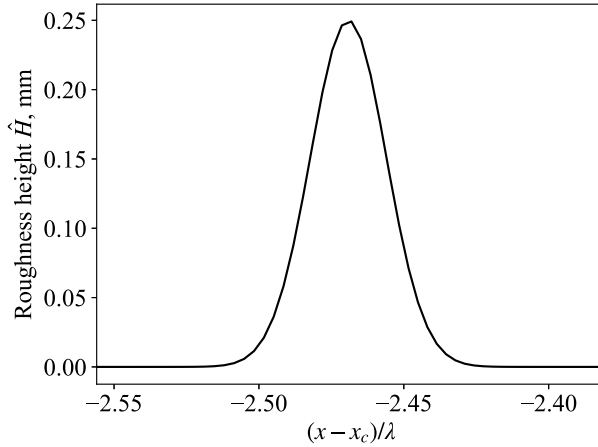


Fig. 3 Wall-forcing shape \hat{H} enforced to generate a TS wave upstream of the indentation area.

We impose an absorbing boundary treatment with PMLs at the inflow and at the outflow of the computational domain, with width 40 mm corresponding to approximately $\lambda/2$. In practice, an established rule of thumb is that a PML width of at least half the wavelength of the wave to be damped is sufficient. The maximum grid compression parameter was set to $\kappa_{\max} = 6$, with a zero complex frequency shift. The target reflection coefficient is $R_c = 0.01\%$. In a similar manner as Martin and Couder-Castaneda [29], the maximum value of the damping profile is computed as

$$\sigma_{\max} = -\frac{3 \max_{\Omega} \{|\bar{\mathbf{u}}|\} \log(R_c)}{2L_{\text{PML}}} \quad (17)$$

These settings allow an efficient damping of the perturbation field as demonstrated in Fig. 4. The increasing amplitude of the spatially developing TS structures in the wake of the indentation region smoothly vanishes between the PML interface and the outflow boundary of the domain, where a zero Dirichlet boundary condition is imposed.

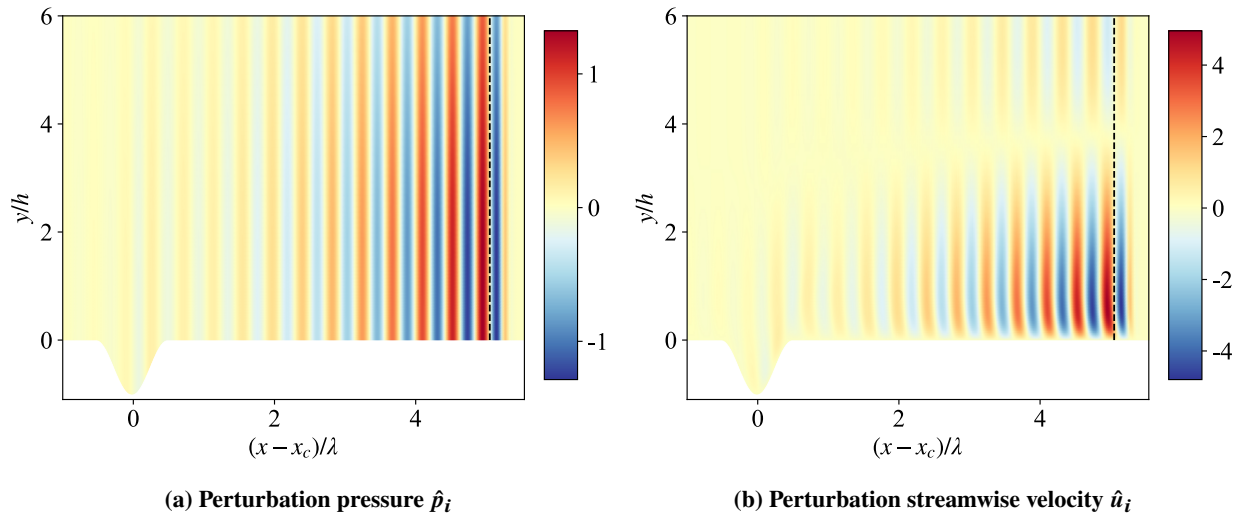


Fig. 4 Contours of perturbation variables for the $h = 0.81$ mm case, zoomed in near the outflow and the wall region. The dashed line (- -) indicates the start of the PML region.

The prescribed frequency of the TS wave is $f = 172$ Hz and corresponds to a non-dimensional frequency of

$F = 10^6 \times 2\pi f v_\infty / U_\infty^2 = 50$. Figure 5 depicts the evolution of the maximum amplitude of \hat{u} across the streamwise direction for the three different indentation depths. Results from the present LNS-based receptivity approach are compared with the PSE-3D results of Gowree et al. [37]. It is obvious that the indentation region acts as a destabilizer of the TS wave. Unlike the receptivity approach where initial amplitude information is computed as part of the solution

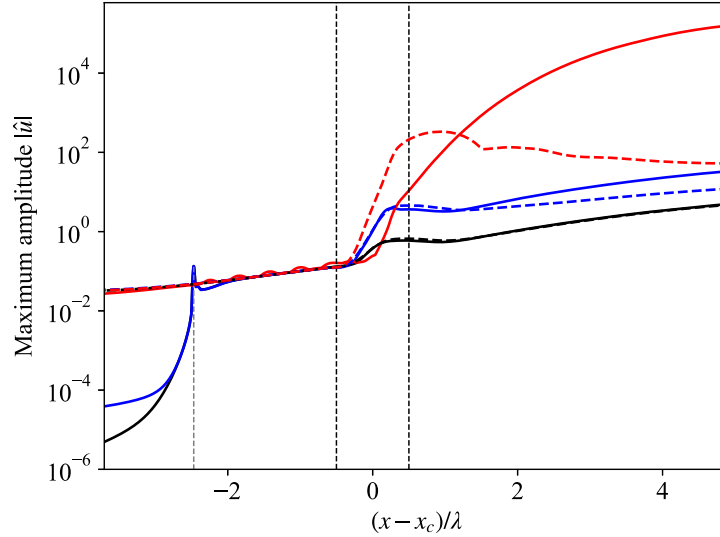


Fig. 5 Maximum amplitude of the TS wave. LNS results: (—) $h = 0.81$ mm, (—) $h = 1.62$ mm, (—) $h = 2.17$ mm. Corresponding dashed lines are PSE-3D results from Gowree et al. [37]. The wall-roughness forcing (--) is located upstream of the indentation region (- -).

process, PSE-based theory only yields the streamwise evolution of the perturbation without quantitative information about the imposed initial disturbance level. In linear PSE simulations, a local, normalized eigenfunction of the same frequency f is imposed at the inflow and the state of amplification is monitored relative to this initial disturbance magnitude. An excellent match is noted between the two approaches when $h = 0.81$ mm. The discrepancies growing with increasing depth may be due to a number of reasons. The underlying hypothesis of the PSE-3D is that of a slowly varying streamwise base flow variation, whereas the LNS formulation makes no such assumption. Some streamwise derivatives are neglected in the PSE-3D equations whereas they might be significant in the indentation region, given the base flow gradients. However, it should also be noted that the PSE-3D performs spanwise plane marching, taking into account the three-dimensionality of the base flow but the LNS-based simulations are purely two-dimensional.

For the $h = 2.17$ mm setting, the LNS approach predicts very large amplitudes in the wake of the indentation which in all practical sense, should then undergo a strongly non-linear mechanism given the significant magnitude of the disturbance. Nonetheless, of particular interest is the behavior predicted upstream of the indentation region. In Fig. 5, the surface based Gaussian actuation is located at $(x - x_c)/\lambda \approx -2.47$ for all three indentations. The $h = 0.81$ mm and $h = 1.62$ mm results are as expected in that the TS amplitudes decay significantly upstream of the actuation location, grow linearly downstream and then undergo further destabilization as the waves convect over the indentation, and then in the wake region. However, the behavior predicted for the $h = 2.17$ mm indentation is radically different. Although the location, shape and magnitude of actuation remain unchanged compared to the shallower indentations, we presume that the low-magnitude forcing appears to be completely "swamped" by a very strong upstream effect arising from the indentation field.

Next, a parametric sweep for a range of actuation frequencies f to determine the most destabilizing TS disturbances is undertaken. We sweep f between 77 Hz and 229 Hz with a constant step of $\Delta f = 19$ Hz. This corresponds to a non-dimensional angular frequency ω in Eq. (4b) ranging between 0.02 and 0.06. The maximum amplitude of the TS wave across the domain is monitored. Figures 6 and 7 present the evolution of the maximum amplitude for the frequency range aforementioned, respectively for $h = 0.81$ mm and $h = 1.62$ mm. For all frequencies, a sudden amplitude increase can be observed at about one-third of the way across the indentation region. Further downstream, amplification continues except for frequencies above 200 Hz, approximately. For these higher frequencies the maximum amplitude decays in the wake of the indentation. The effectiveness of the PML regions causing a significant reduction of the TS wave amplitudes

in the outflow region is clearly evident.

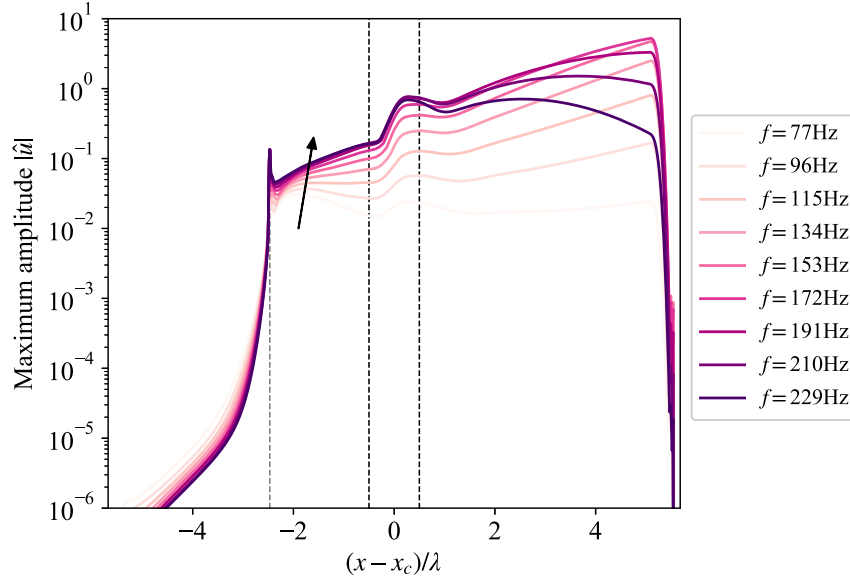


Fig. 6 Evolution of the maximum streamwise amplitude \hat{u} across the domain for the $h = 0.81$ mm case. The arrow shows the direction in which frequency is increased.

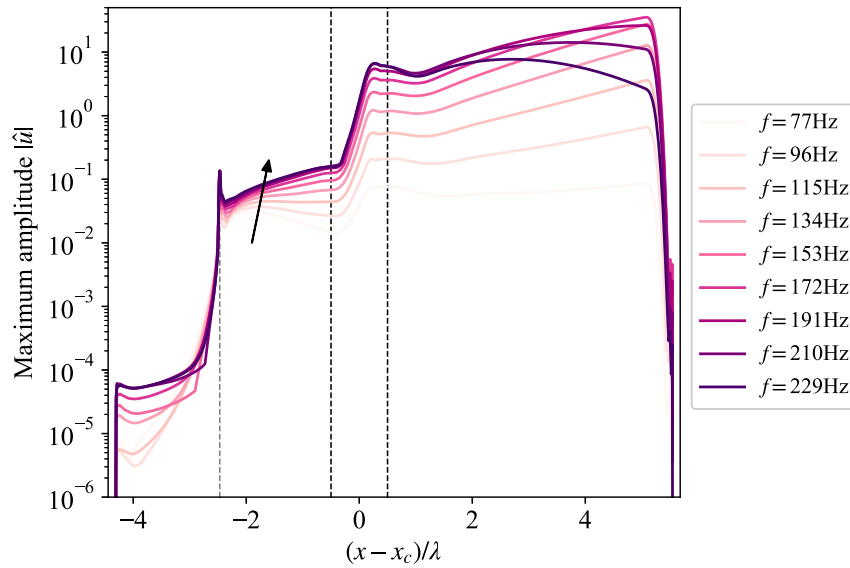


Fig. 7 Evolution of the maximum streamwise amplitude \hat{u} across the domain for the $h = 1.62$ mm case. The arrow shows the direction in which frequency is increased.

These cases are relatively benign compared to the $h = 2.17$ mm case displayed in Fig. 8. In a more accentuated manner than the two smaller depths, the streamwise location of the sharp rise in TS wave amplitude in the indentation moves downstream as the wave frequency increases. Moreover, in all the frequency values examined, the wave amplitudes continue growing substantially downstream of the indentation, until where the artificially imposed PML domain becomes active. As alluded to earlier, we speculate strongly upstream propagating waves are predicted in all cases, with only the PML at the inflow boundary acting to diminish wave amplitudes. Although the domain stretches

approximately by 5λ beyond the indentation, potential decay may occur further downstream. Of significant note is that TS disturbance amplitudes increase by a factor of 10^6 relative to amplitude levels at the indentation center.

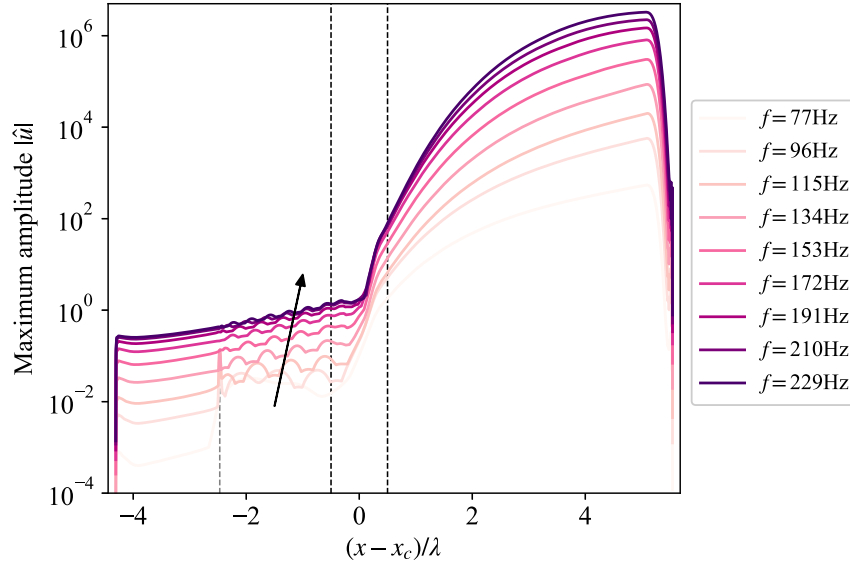


Fig. 8 Evolution of the maximum streamwise amplitude \hat{u} across the domain for the $h = 2.17$ mm case. The arrow shows the direction in which frequency is increased.

B. Temporal BiGlobal analysis

In this analysis, 600 eigenvalues are sought in the vicinity of the origin with a Krylov subspace of dimension 1200. The relative tolerance for eigenvalue convergence is set to 10^{-10} . The convergence of the Krylov-Schur algorithm together with the shift-and-invert approach is significantly dependent upon how close the shift value is located to the eigenvalues. Different boundary treatments at the inflow and outflow are compared, including the PML introduced in section III.C and a Robin-type radiation boundary condition defined as $\hat{\mathbf{q}}_x = i\alpha_{\text{PSE}}\hat{\mathbf{q}}$. α_{PSE} is the most unstable local streamwise wavenumber at the inflow or outflow location computed from a preliminary PSE analysis. When the PML method is applied, one notes that the unknown ω appears in the denominator of the coordinate stretching in Eq. (7), transforming the linear GEVP into a non-linear eigenvalue problem. We overcome this extra-difficulty by prescribing a constant $\tilde{\omega} = 0.01$ in the coordinate stretching, the value corresponding to the region of interest for ω_r . This artifice cannot guarantee optimal efficiency of the lossy layers for all angular frequencies of the perturbation modes that we wish to damp at the boundaries.

Figure 9 presents the physically relevant portion of the temporal eigenvalue spectra for the indentations of depth $h = 1.62$ mm and $h = 2.17$ mm with $\beta = 0$. The non-dimensional angular frequency is $\omega_r = \delta_h \omega_r^* / U_\infty$ and the amplification rate ω_i is scaled in the same way. The eigenmodes forming the dense, inverse U-shaped, continuous spectrum branches located near $\omega_i = -0.01$ can be distinguished from branches including wall modes branches, TS modes as well as "boundary condition" modes; these may be considered as physically spurious since they have a spatial distribution localized exclusively at the outflow of the computational domain. Unfortunately, the computation of the laminar boundary layer base flow was limited to approximately 5λ positions downstream of the indentation streamwise extent, thus restricting the computation of the full spatial streamwise mode structure. In addition, Lesshaft [38] states that the numerical truncation of the computational domain is also known to introduce spurious eigenvalues.

We focus our attention on the few most unstable and least stable global modes retrieved by the analysis. All the different boundary treatments, including the PML, are able to recover the least stable global mode denoted S_1 in Fig. 9a as well as the unstable global modes indicated by S_2 and S_3 in Fig. 9b. No physically relevant temporal global modes arose in the shallow $h = 0.81$ mm indentation which does not give rise to a LSB, nor features reversed flow. That is the reason why the corresponding spectrum is not included. Note how the choice of boundary conditions affects the spatial distribution of the spectra but not the global modes. Table 1 summarizes their numerical values.

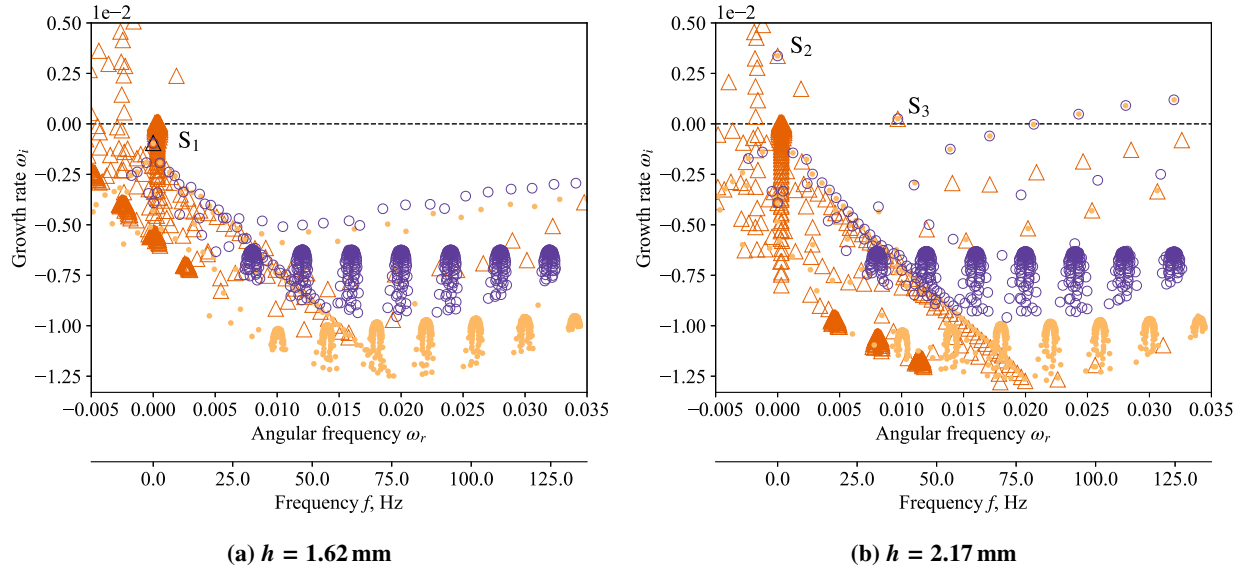


Fig. 9 Temporal spectra obtained with $\beta = 0$, comparison between different sets of inflow/outflow boundary conditions. (Δ): PML/PML. (\bullet): Zero Dirichlet/Robin. (\circ): Robin/Robin. One of the symbols for the mode S_1 is changed to (Δ) for clarity.

Table 1 Least stable and most unstable global modes for the $h = 1.62$ mm and $h = 2.17$ mm cases, $\beta = 0$.

Mode	Depth h	Stability	ω_r	ω_i
S_1	1.62 mm	Stable	$+2.06 \times 10^{-7}$	-9.66×10^{-4}
S_2	2.17 mm	Unstable	-1.78×10^{-9}	$+3.37 \times 10^{-3}$
S_3	2.17 mm	Unstable	$+9.70 \times 10^{-3}$	$+2.55 \times 10^{-4}$

Looking at the eigenvalue distribution, the $h = 2.17$ mm corresponding boundary layer is more temporally unstable than the $h = 1.62$ mm case. As expected, the application of the PML method yields additional branches of non-physical eigenvalues. The almost matching branches on the right-hand-side of Fig 9b may be arising from the imposition of Zero Dirichlet inflow (Δ / \bullet) and Robin-type outflow (\bullet / \circ) boundary conditions.

The two unstable modes found in the case where the peak reversed-flow velocity is 9% remain inactive in the intermediate 3% case. This is consistent with the observations of Rodríguez and Theofilis [11] but not in agreement with the more recent 12% threshold of Rodríguez et al. [13]. It highlights the possibility of the peak reversed-flow criterion not being valid for all kinds of generated LSBs. Further criteria require investigation, such as the relative position of the inflection point with respect to the recirculation region [39].

Next, we examine how the spatial distribution of these modes is affected by allowing the existence of spanwise periodic modes through the non-dimensional spanwise wavenumber $\beta = \delta_h \beta^*$, which has been varied from 0.01 to 1.0. In what follows, results are shown with a zero Dirichlet inflow and a Robin boundary condition at the outflow. Figure 10 shows the contour plots of \hat{u}_i for the least stable mode S_1 , which is stationary and remains stable when β is increased to 1. For a purely two-dimensional perturbation field, the mode structure extends from a region of small velocity in the indentation and grows in magnitude further downstream. Near the outflow boundary, the streamwise perturbation velocity is maximum. Given the aforementioned difficulty of dealing with a short base flow streamwise domain, the spatial extent of the structure cannot be fully described. As β increases, the mode remains stable. However, the region of maximum streamwise perturbation velocity is gradually transferred to a region localized in the indentation area, suggesting that two superimposed modes might coexist and merge at greater spanwise wavenumbers. The values of β for which the stationary mode is least stable are 0.1-0.2 corresponding to L_z in the range 14.25-28.50 h .

For the deepest indentation case and $\beta = 0$, the absolute temporal instability corresponds to a localized feature above the indentation region and slightly shifted downstream as seen in the top-left part of Fig. 11. The mode is stationary,

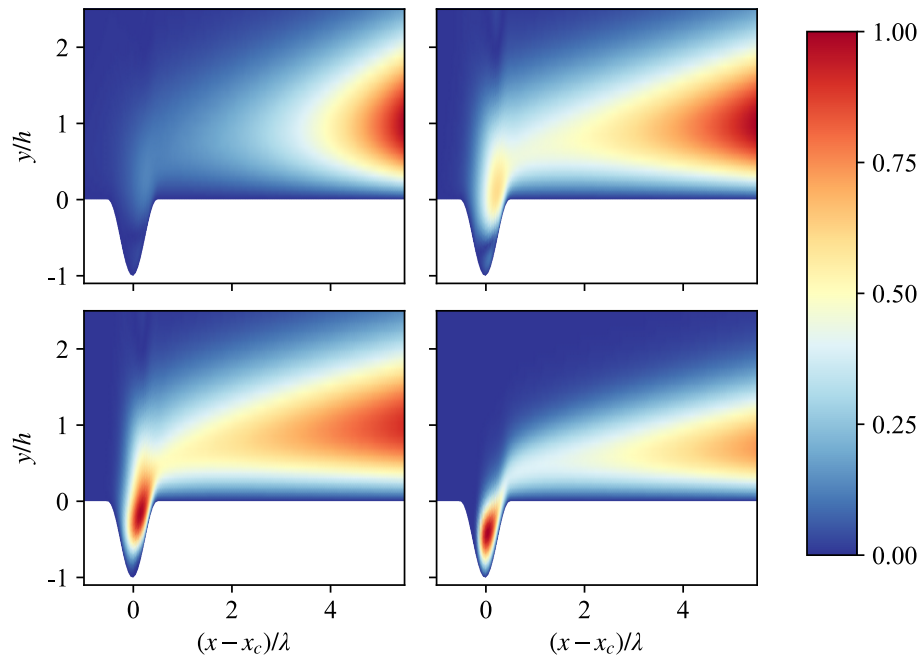


Fig. 10 Spatial distribution of streamwise perturbation velocity amplitude $|\hat{u}|$ with increasing values of β for the least stable temporal mode S_1 in the $h = 1.62$ mm case. Top-left: $\beta = 0$. Top-right: $\beta = 0.04$. Bottom-left: $\beta = 0.1$. Bottom-right: $\beta = 1$.

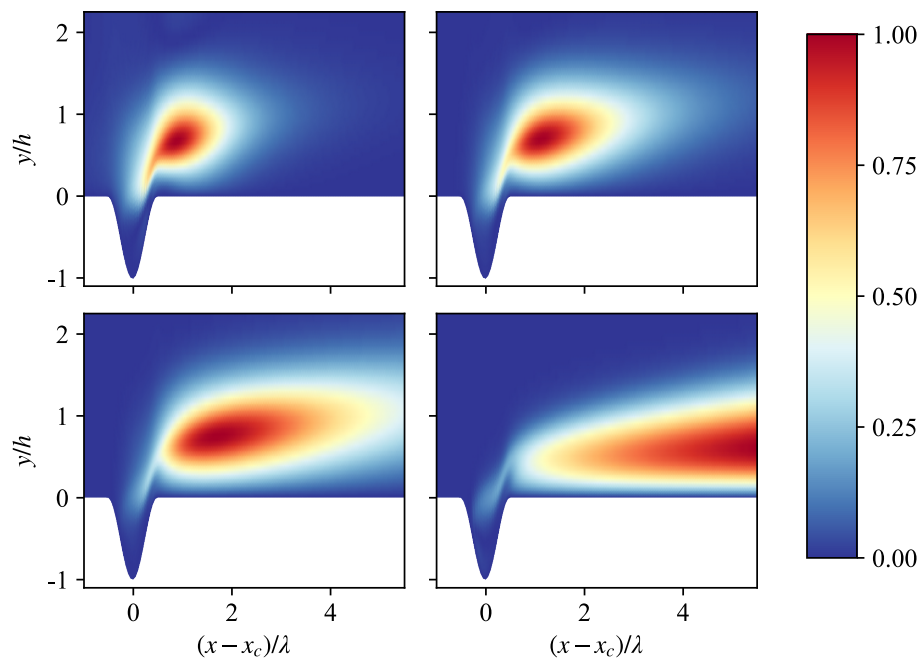


Fig. 11 Spatial distribution of streamwise perturbation velocity amplitude $|\hat{u}|$ with increasing values of β for the most unstable temporal mode S_2 in the $h = 2.17$ mm case. Top-left: $\beta = 0$, unstable. Top-right: $\beta = 0.05$, unstable. Bottom-left: $\beta = 0.1$, unstable. Bottom-right: $\beta = 1$, stable.

$\omega_r = 0$ (to numerical accuracy) and unstable up to $\beta = 0.5$ corresponding to $L_z \approx 4.25h$. It becomes stable as β further increases and L_z decreases. Hence, the absolute instability of the boundary layer is weakened by smaller periodicity wavelengths. The localized structure is stretched in the streamwise direction as the wavenumber β increases.

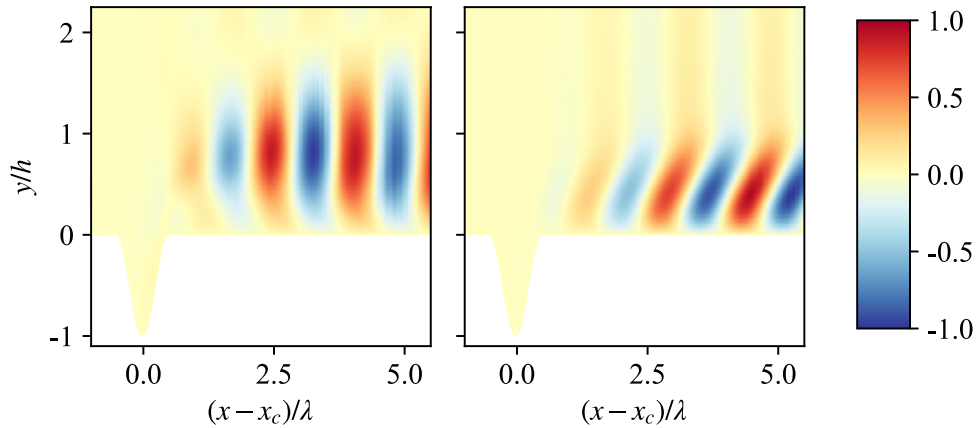


Fig. 12 Spatial distribution of streamwise perturbation \hat{u}_i (left) and spanwise perturbation \hat{w}_i (right) for the unstable mode S_3 , $\beta = 0.01$.

The second relevant unstable mode S_3 resembles a wave-like mode and could be attributed to a Kelvin-Helmholtz mechanism of frequency $f = 37.8$ Hz. Figure 12 represents the corresponding streamwise and spanwise perturbation velocity developing spatially in the wake of the indentation region for $\beta = 0.01$. The mode becomes rapidly stable, beyond $\beta = 0.02$ and the wave-like structure is found to degenerate with further increments in β .

VI. Conclusions

This work comprised an initial analysis of how localized surface indentations impacts the stability of a developing boundary layer featuring two-dimensional LSBs. The numerical investigation was performed with a two-dimensional steady base flow assumption, together with a periodicity assumption of instabilities in the spanwise direction. The indentation with the deepest depth, and hence strongest laminar separation bubble intensity distinguishes itself from the shallower indentations. Two distinct analyses were undertaken.

In the temporal BiGlobal analysis, consistent with literature, it was found that the flow is first temporally unstable due to a stationary mode localized near the indentation region and second to a traveling Kelvin-Helmholtz mode. However, the former was found to become stable below spanwise periodicity lengths of $4.25h$ while the latter is stabilized as soon as the spanwise wavenumber becomes positive. The performed receptivity analysis showed that a preexisting, incoming TS wave is amplified in the wake of the $h = 0.81$ mm and $h = 1.62$ mm indentations over a limited range of frequencies. The deepest indentation depth features significant levels of amplification, and a potential manifestation of a new mechanism where the time-harmonic, linearized Navier Stokes framework suggests a strong upstream and downstream propagating structure; the physical mechanism of which requires to be understood. This could potentially be tied in with the occurrence and prediction of the unstable stationary mode found with the BiGlobal analysis, however further work is required to fully describe the findings.

Furthermore, we successfully applied the perfectly matched layer to the incompressible, time-harmonic LNS equations to absorb outgoing waves at the computational boundaries. This implies that the forced receptivity problem and spatial BiGlobal problems can be treated autonomously, by setting damping-based PML parameters rather than dealing with more tedious wave-dependent parameters. We believe this provides a more generic boundary treatment. Applying the method to the temporal BiGlobal problem required a small adjustment and the impact on physics was solely characterized by spurious eigenvalues on the spectrum.

The parametric studies were performed with rapid turnover thanks to the parallel efficiency of the computational tool. Extending the analysis to a TriGlobal approach is a logical extension of this work, which could also be supplemented by adjoint analysis in order to describe the sensitivity of the global modes to fully three-dimensional geometrical deformation and fully three-dimensional base flow variation.

Acknowledgments

This work is part of a project which has received funding from the European Union's Horizon 2020 research and innovation program under the Marie Skłodowska-Curie grant agreement No. 675008. Aspects of this work have been supported by the Innovate UK funded ALFET project 113022. The authors would like to thank Jose E. Roman and Oliver J. Dellar for their valuable comments.

References

- [1] Hoikkala, H., and Magnusson, N., "As 'Flying Shame' Grips Sweden, SAS Ups Stakes in Climate Battle," *Bloomberg*, 2019. URL <https://www.bloomberg.com/news/articles/2019-04-14/as-flying-shame-grips-sweden-sas-ups-stakes-in-climate-battle>
- [2] Schrauf, G., "Status and perspectives of laminar flow," *The Aeronautical Journal*, Vol. 109, No. 1102, 2005, pp. 639–644. doi:10.1017/S00019240000097X.
- [3] Morkovin, M., "Transition in open flow systems - a reassessment," *Bull. Am. Phys. Soc.*, Vol. 39, 1994, p. 1882.
- [4] Reshotko, E., "Transient growth: A factor in bypass transition," *Physics of Fluids*, Vol. 13, No. 5, 2001, pp. 1067–1075. doi:10.1063/1.1358308.
- [5] Ruban, A. I., Bernots, T., and Kravtsova, M. A., "Linear and nonlinear receptivity of the boundary layer in transonic flows," *Journal of Fluid Mechanics*, Vol. 786, 2016, pp. 154–189. doi:10.1017/jfm.2015.587.
- [6] Theofilis, V., Hein, S., and Dallmann, U., "On the origins of unsteadiness and three-dimensionality in a laminar separation bubble," *Philosophical Transactions of the Royal Society of London A: Mathematical, Physical and Engineering Sciences*, Vol. 358, No. 1777, 2000, pp. 3229–3246. doi:10.1098/rsta.2000.0706.
- [7] Barkley, D., Gomes, M. G. M., and Henderson, D. D., "Three-dimensional instability in flow over a backward-facing step," *Journal of Fluid Mechanics*, Vol. 473, 2002, pp. 167–190. doi:10.1017/S002211200200232X.
- [8] Gallaire, F., Marquillie, M., and Ehrenstein, U., "Three-dimensional transverse instabilities in detached boundary layers," *Journal of Fluid Mechanics*, Vol. 571, 2007, pp. 221–233. doi:10.1017/S0022112006002898.
- [9] Marquet, O., Lombardi, M., Chomaz, J.-M., Sipp, D., and Jacquin, L., "Direct and adjoint global modes of a recirculation bubble: lift-up and convective non-normalities," *Journal of Fluid Mechanics*, Vol. 622, 2009, pp. 1–21. doi:10.1017/S0022112008004023.
- [10] Xu, H., Lombard, J.-E. W., and Sherwin, S. J., "Influence of localised smooth steps on the instability of a boundary layer," *Journal of Fluid Mechanics*, Vol. 817, 2017, pp. 138–170. doi:10.1017/jfm.2017.113.
- [11] Rodríguez, D., and Theofilis, V., "Structural changes of laminar separation bubbles induced by global linear instability," *Journal of Fluid Mechanics*, Vol. 655, 2010, pp. 280–305. doi:10.1017/S0022112010000856.
- [12] Marquet, O., Sipp, D., Chomaz, J.-M., and Jacquin, L., "Amplifier and resonator dynamics of a low-Reynolds-number recirculation bubble in a global framework," *Journal of Fluid Mechanics*, Vol. 605, 2008, pp. 429–443. doi:10.1017/S0022112008000323.
- [13] Rodríguez, D., Gennaro, E. M., and Juniper, M. P., "The two classes of primary modal instability in laminar separation bubbles," *Journal of Fluid Mechanics*, Vol. 734, 2013, p. R4. doi:10.1017/jfm.2013.504.
- [14] Thomas, C., Mughal, S., and Ashworth, R., "Development of Tollmien-Schlichting disturbances in the presence of laminar separation bubbles on an unswept infinite wavy wing," *Phys. Rev. Fluids*, Vol. 2, 2017, p. 043903. doi:10.1103/PhysRevFluids.2.043903.
- [15] Xu, H., Mughal, S. M., Gowree, E. R., Atkin, C. J., and Sherwin, S. J., "Destabilisation and modification of Tollmien-Schlichting disturbances by a three-dimensional surface indentation," *Journal of Fluid Mechanics*, Vol. 819, 2017, pp. 592–620. doi:10.1017/jfm.2017.193.
- [16] Johnston, H., and Liu, J.-G., "Accurate, stable and efficient Navier-Stokes solvers based on explicit treatment of the pressure term," *Journal of Computational Physics*, Vol. 199, No. 1, 2004, pp. 221–259. doi:10.1016/j.jcp.2004.02.009.
- [17] Shirokoff, D., and Rosales, R., "An efficient method for the incompressible Navier-Stokes equations on irregular domains with no-slip boundary conditions, high order up to the boundary," *Journal of Computational Physics*, Vol. 230, No. 23, 2011, pp. 8619–8646. doi:10.1016/j.jcp.2011.08.011.

- [18] Dellar, O. J., and Jones, B. L., “Dynamically correct formulations of the linearised Navier-Stokes equations,” *International Journal for Numerical Methods in Fluids*, Vol. 85, No. 1, 2017, pp. 3–29. doi:10.1002/fld.4370.
- [19] Rempfer, D., “On boundary conditions for incompressible Navier-Stokes problems,” *Applied Mechanics Reviews*, Vol. 59, No. 3, 2006, pp. 107–125. doi:10.1115/1.2177683.
- [20] Theofilis, V., “The linearized pressure Poisson equation for global instability analysis of incompressible flows,” *Theoretical and Computational Fluid Dynamics*, Vol. 31, No. 5, 2017, pp. 623–642. doi:10.1007/s00162-017-0435-z.
- [21] Theofilis, V., “Advances in global linear instability analysis of nonparallel and three-dimensional flows,” *Progress in Aerospace Sciences*, Vol. 39, No. 4, 2003, pp. 249–315. doi:10.1016/S0376-0421(02)00030-1.
- [22] Groot, K., Pinna, F., and van Oudheusden, B., “On Closing the Streamwise BiGlobal Stability Problem: The Effect of Boundary Conditions,” *Procedia IUTAM*, Vol. 14, 2015, pp. 459–468. doi:10.1016/j.piutam.2015.03.074, IUTAM_ABCM Symposium on Laminar Turbulent Transition.
- [23] Gaster, M., “A note on the relation between temporally-increasing and spatially-increasing disturbances in hydrodynamic stability,” *Journal of Fluid Mechanics*, Vol. 14, No. 2, 1962, pp. 222–224. doi:10.1017/S0022112062001184.
- [24] Berenger, J.-P., “A perfectly matched layer for the absorption of electromagnetic waves,” *Journal of Computational Physics*, Vol. 114, No. 2, 1994, pp. 185–200. doi:10.1006/jcph.1994.1159.
- [25] Hu, F. Q., Li, X., and Lin, D., “Absorbing boundary conditions for nonlinear Euler and Navier–Stokes equations based on the perfectly matched layer technique,” *Journal of Computational Physics*, Vol. 227, No. 9, 2008, pp. 4398–4424. doi:10.1016/j.jcp.2008.01.010.
- [26] Komatitsch, D., and Martin, R., “An unsplit convolutional perfectly matched layer improved at grazing incidence for the seismic wave equation,” *Geophysics*, Vol. 72, No. 5, 2007, pp. SM155–SM167. doi:10.1190/1.2757586.
- [27] Merle, M., “Numerical approach for the global stability analysis of subsonic boundary flows,” Ph.D. thesis, École Nationale Supérieure d’Arts et Métiers - ENSAM, Sep. 2015.
- [28] Ran, W., Zare, A., Nichols, J. W., and Jovanovic, M. R., “The effect of sponge layers on global stability analysis of Blasius boundary layer flow,” *47th AIAA Fluid Dynamics Conference*, 2017, p. 3456. doi:10.2514/6.2017-3456.
- [29] Martin, R., and Couder-Castaneda, C., “An improved unsplit and convolutional perfectly matched layer absorbing technique for the Navier-Stokes equations using cut-off frequency shift,” *Computer Modeling in Engineering & Sciences*, Vol. 63, No. 1, 2010, pp. 47–77. doi:10.3970/cmesc.2010.063.047.
- [30] Cantwell, C., Moxey, D., Comerford, A., Bolis, A., Rocco, G., Mengaldo, G., Grazia, D. D., Yakovlev, S., Lombard, J.-E., Ekelschot, D., Jordi, B., Xu, H., Mohamied, Y., Eskilsson, C., Nelson, B., Vos, P., Biotto, C., Kirby, R., and Sherwin, S., “Nektar++: An open-source spectral/hp element framework,” *Computer Physics Communications*, Vol. 192, 2015, pp. 205–219. doi:10.1016/j.cpc.2015.02.008.
- [31] Hermanns, M., and Hernández, J. A., “Stable high-order finite-difference methods based on non-uniform grid point distributions,” *International Journal for Numerical Methods in Fluids*, Vol. 56, No. 3, 2007, pp. 233–255. doi:10.1002/fld.1510.
- [32] Groot, K. J., Serpieri, J., Kotsonis, M., and Pinna, F., “Secondary Stability Analysis of Crossflow Vortices using BiGlobal Theory on PIV Base Flows,” *55th AIAA Aerospace Sciences Meeting*, 2017, p. 1880. doi:10.2514/6.2017-1880.
- [33] Liseikin, V. D., *Grid Generation Methods*, Scientific Computation, Springer International Publishing, 2017. doi:10.1007/978-90-481-2912-6.
- [34] Balay, S., Gropp, W. D., McInnes, L. C., and Smith, B. F., “Efficient Management of Parallelism in Object Oriented Numerical Software Libraries,” *Modern Software Tools in Scientific Computing*, edited by E. Arge, A. M. Bruaset, and H. P. Langtangen, Birkhäuser Press, 1997, pp. 163–202. doi:10.1007/978-1-4612-1986-6_8.
- [35] Amestoy, P. R., Guermouche, A., L’Excellent, J.-Y., and Pralet, S., “Hybrid scheduling for the parallel solution of linear systems,” *Parallel Computing*, Vol. 32, No. 2, 2006, pp. 136–156. doi:10.1016/j.parco.2005.07.004.
- [36] Hernandez, V., Roman, J. E., and Vidal, V., “SLEPc: A Scalable and Flexible Toolkit for the Solution of Eigenvalue Problems,” *ACM Trans. Math. Software*, Vol. 31, No. 3, 2005, pp. 351–362. doi:10.1145/1089014.1089019.
- [37] Gowree, E. R., Mughal, S., Xu, H., and Atkin, C., “Linear and non-linear instability of Tollmien-Schlichting waves over a localised three-dimensional surface indentation,” *Journal of Fluid Mechanics*, 2019. (submitted for publication).

- [38] Lesshaft, L., “Artificial eigenmodes in truncated flow domains,” *Theoretical and Computational Fluid Dynamics*, Vol. 32, No. 3, 2018, pp. 245–262. doi:10.1007/s00162-017-0449-6.
- [39] Avanci, M. P., Rodríguez, D., and Alves, L. S. d. B., “A geometrical criterion for absolute instability in separated boundary layers,” *Physics of Fluids*, Vol. 31, No. 1, 2019, p. 014103. doi:10.1063/1.5079536.